

Towards an Understanding of the Correlations in Jet Substructure

Report of BOOST2013, hosted by the University of Arizona, 12th-16th of August 2013.

D. Adams¹, A. Arce², L. Asquith³, M. Backovic⁴, T. Barillari⁵, P. Berta⁶, D. Bertolini⁷,
A. Buckley⁸, J. Butterworth⁹, R. C. Camacho Toro¹⁰, J. Caudron¹¹, Y.-T. Chien¹², J. Cogan¹³,
B. Cooper⁹, D. Curtin¹⁴, C. Debenedetti¹⁵, J. Dolen¹⁶, M. Eklund¹⁷, S. El Hedri¹¹,
S. D. Ellis¹⁸, T. Embry¹⁷, D. Ferencek¹⁹, J. Ferrando⁸, S. Fleischmann²⁰, M. Freytsis²¹,
M. Giulini²², Z. Han²³, D. Hare²⁴, P. Harris²⁵, A. Hinzmann²⁶, R. Hoing²⁷, A. Hornig¹²,
M. Jankowiak²⁸, K. Johns¹⁷, G. Kasieczka²⁹, R. Kogler²⁷, W. Lampl¹⁷, A. J. Larkoski³⁰,
C. Lee¹², R. Leone¹⁷, P. Loch¹⁷, D. Lopez Mateos²¹, H. K. Lou³¹, M. Low³²,
P. Maksimovic³³, I. Marchesini²⁷, S. Marzani³⁰, L. Masetti¹¹, R. McCarthy³⁴, S. Menke⁵,
D. W. Miller³², K. Mishra²⁴, B. Nachman¹³, P. Nef¹³, F. T. O'Grady¹⁷, A. Ovcharova³⁵,
A. Picazio¹⁰, C. Pollard⁸, B. Potter-Landua²⁵, C. Potter²⁵, S. Rappoccio¹⁶, J. Rojo³⁶,
J. Rutherford¹⁷, G. P. Salam^{25,37}, J. Schabinger³⁸, A. Schwartzman¹³, M. D. Schwartz²¹,
B. Shuve³⁹, P. Sinervo⁴⁰, D. Soper²³, D. E. Sosa Corral²², M. Spannowsky⁴¹, E. Strauss¹³,
M. Swiatlowski¹³, J. Thaler³⁰, C. Thomas²⁵, E. Thompson⁴², N. V. Tran²⁴, J. Tseng³⁶,
E. Usai²⁷, L. Valery⁴³, J. Veatch¹⁷, M. Vos⁴⁴, W. Waalewijn⁴⁵, J. Wacker¹³, and C. Young²⁵

¹Brookhaven National Laboratory, Upton, NY 11973, USA

²Duke University, Durham, NC 27708, USA

³Argonne National Laboratory, Lemont, IL 60439, USA

⁴CP3, Universite catholique du Louvain, B-1348 Louvain-la-Neuve, Belgium

⁵Max-Planck-Institute fuer Physik, 80805 Muenchen, Germany

⁶Charles University in Prague, FMP, V Holesovickach 2, Prague, Czech Republic

⁷University of California, Berkeley, CA 94720, USA

⁸University of Glasgow, Glasgow, G12 8QQ, UK

⁹University College London, WC1E 6BT, UK

¹⁰University of Geneva, CH-1211 Geneva 4, Switzerland

¹¹Universitaet Mainz, DE 55099, Germany

¹²Los Alamos National Laboratory, Los Alamos, NM 87545, USA

¹³SLAC National Accelerator Laboratory, Menlo Park, CA 94025, USA

¹⁴University of Maryland, College Park, MD 20742, USA

¹⁵University of California, Santa Cruz, CA 95064, USA

¹⁶University at Buffalo, Buffalo, NY 14260, USA

¹⁷University of Arizona, Tucson, AZ 85719, USA

¹⁸University of Washington, Seattle, WA 98195, USA

¹⁹Rutgers University, Piscataway, NJ 08854, USA

²⁰Bergische Universitaet Wuppertal, Wuppertal, D-42097, Germany

²¹Harvard University, Cambridge, MA 02138, USA

²²Universitaet Heidelberg, DE-69117, Germany

²³University of Oregon, Eugene, OR 97403, USA

²⁴Fermi National Accelerator Laboratory, Batavia, IL 60510, USA

²⁵CERN, CH-1211 Geneva 23, Switzerland

²⁶Universitaet Zuerich, 8006 Zuerich, Switzerland

²⁷Universitaet Hamburg, DE-22761, Germany

²⁸New York University, New York, NY 10003, USA

²⁹ETH Zuerich, 8092 Zuerich, Switzerland

³⁰Massachusetts Institute of Technology, Cambridge, MA 02139, USA

³¹Princeton University, Princeton, NJ 08544, USA

³²University of Chicago, IL 60637, USA

³³Johns Hopkins University, Baltimore, MD 21218, USA

³⁴YITP, Stony Brook University, Stony Brook, NY 11794-3840, USA

³⁵Berkeley National Laboratory, University of California, Berkeley, CA 94720, USA

³⁶University of Oxford, Oxford, OX1 3NP, UK

³⁷LPTHE, UPMC Univ. Paris 6 and CNRS UMR 7589, Paris, France

³⁸Universidad Autonoma de Madrid, 28049 Madrid, Spain

³⁹Perimeter Institute for Theoretical Physics, Waterloo, Ontario N2L 2Y5, Canada

⁴⁰University of Toronto, Toronto, Ontario M5S 1A7, Canada

⁴¹IPPP, University of Durham, Durham, DH1 3LE, UK

⁴²Columbia University, New York, NY 10027, USA

⁴³LPC Clermont-Ferrand, 63177 Aubiere Cedex, France

⁴⁴Instituto de Fisica Corpuscular, IFIC/CNIC-UIVEG, E-46071 Valencia, Spain

⁴⁵University of Amsterdam, 1012 WX Amsterdam, Netherlands

¹Address(es) of author(s) should be given

Abstract Over the past five or so years a large number of observables have been proposed in the literature, and explored at the LHC experiments, that attempt to utilise the internal structure of highly boosted jets in order to distinguish those that have been initiated by a quark, a gluon or by a heavier particle, such as a Top quark or W boson. This report of the BOOST2013 workshop presents original particle-level studies that attempt to improve our understanding of the relationship between these observables, their complementarity and overlap, and the dependence of this on the underlying jet parameters, especially the jet radius R and jet p_T . This is explored in the context of quark/gluon discrimination, boosted W-boson tagging and boosted Top quark tagging.

Keywords boosted objects · jet substructure · beyond-the-Standard-Model physics searches · Large Hadron Collider

1 Introduction

A characteristic feature of the proton-proton collisions at the LHC is a center-of-mass energy, 7 TeV in 2010 and 2011, 8 TeV in 2012, and 13TeV with the start of the second phase of operation in 2015, that, even after accounting for parton density functions, is large compared to the heaviest of the known particles. Thus these particles (and potentially also previously unknown ones) will often be produced at the LHC with substantial boosts. As a result, when decaying hadronically, these particles will not be observed as multiple jets in the detector, but rather as a single hadronic jet with distinctive internal substructure. This realization has led to a new era of sophistication in our understanding of both standard QCD jets and jets containing the decay of a heavy particle, with an array of new jet observables and detection techniques introduced and studied. To allow the efficient sharing of results from these jet substructure studies a series of BOOST Workshops have been held on a yearly basis: SLAC (2009, [1]), Oxford University (2010, [2]), Princeton University (2011, [3]), IFIC Valencia (2012 [4]), University of Arizona (2013 [5]), and, most recently, University College London (2014 [6]). After each of these meetings Working Groups have functioned during the following year to generate reports highlighting the most interesting new results, including studies of ever maturing details. Previous BOOST reports can be found at [7–9].

This report from BOOST 2013 thus views the study and implementation of jet substructure techniques as a fairly mature field, and focuses on the question of the correlations between the plethora of observables that have been developed and employed, and their dependence on the underlying jet parameters, especially the jet radius R and jet p_T . Samples of quark-, gluon-, W- and Top-initiated jets are constructed at the particle-level using FASTJET [10], and the

performance, in terms of separating signal from background, of various groomed jet masses and jet substructure observables investigated through Receiver Operating Characteristic (ROC) curves, which show the efficiency to “tag” the signal as a function of the efficiency (or rejection, being $1/\text{efficiency}$) to “tag” the background. In new analyses developed for the report, we investigate the separation of a quark signal from a gluon background (q/g tagging), a W signal from a gluon background (W-tagging) and a Top signal from a mixed quark/gluon QCD background (Top-tagging). In the case of Top-tagging, we also investigate the performance of dedicated Top-tagging algorithms, the HepTopTagger [11] and the Johns Hopkins Tagger [12]. Using multivariate techniques, we study the degree to which the discriminatory information provided by the observables and taggers overlaps, by examining in particular the extent to which the signal-background separation performance increases when two or more variables/taggers are combined, via a Boosted Decision Tree (BDT), into a single discriminant. Where possible, we provide a discussion of the physics behind the structure of the correlations and the p_T and R scaling that we observe.

We present the performance of observables in idealized simulations without pile-up and detector resolution effects, with the primary goal of studying the correlations between observables and the dependence on jet radius and p_T . The relationship between substructure observables, their correlations, and how these depend on the jet radius R and jet p_T should not be too sensitive to pile-up and resolution effects; conducting studies using idealized simulations allows us to more clearly elucidate the underlying physics behind the observed performance, and also provides benchmarks for the development of techniques to mitigate pile-up and detector effects. A full study of the performance of pile-up and detector mitigation strategies is beyond the scope of the current report, and will be the focus of upcoming studies.

The report is organized as follows. In Section 2 we describe the generation of the Monte Carlo event samples that we use in the studies that follow. In Section 3 we detail the jet algorithms, observables and taggers investigated in each section of the report, and in Section 4 the multivariate techniques used to combine the one or more of the observables into single discriminants. In Section 5 we describe the q/g-tagging studies, in Section 6 we describe the W-tagging studies, and in Section 7 we describe the Top-tagging studies. Finally we offer some summary of the studies and general conclusions in Section 8.

This report presents original analyses and discussions pertaining to the performance of and correlations between various jet substructure techniques applied to quark/gluon discrimination, W-boson tagging, and Top tagging. The principal organizers of and contributors to the analyses pre-

104 sented in the report are: B. Cooper, S. D. Ellis, M. Freyt,
105 sis, A. Hornig, A. Larkoski, D. Lopez Mateos, B. Shuve, and
106 N. V. Tran.

107 2 Monte Carlo Samples

108 In the below sections the Monte Carlo samples used in the
109 q/g tagging, W tagging and Top tagging sections of this re-
110 port are described. Note that in all cases the samples used
111 contain no additional proton-proton interactions beyond the
112 hard scatter (no pile-up), and there is no attempt to emulate
113 the degradation in angular and p_T resolution that would re-
114 sult when reconstructing the jets inside a real detector.

115 2.1 Quark/gluon and W tagging

116 Samples were generated at $\sqrt{s} = 8$ TeV for QCD dijets, and
117 for W^+W^- pairs produced in the decay of a (pseudo) scalar
118 resonance and decaying hadronically. The QCD events were
119 split into subsamples of gg and $q\bar{q}$ events, allowing for tests
120 of discrimination of hadronic W bosons, quarks, and gluons.

121 Individual gg and $q\bar{q}$ samples were produced at leading
122 order (LO) using MADGRAPH5 [13], while W^+W^- sam-
123 ples were generated using the JHU GENERATOR [14–16]
124 to allow for separation of longitudinal and transverse polar-
125 izations. Both were generated using CTEQ6L1 PDFs [17].
126 The samples were produced in exclusive p_T bins of width
127 100 GeV, with the slicing parameter chosen to be the p_T of
128 any final state parton or W at LO. At the parton-level the
129 p_T bins investigated were 300-400 GeV, 500-600 GeV and
130 1.0-1.1 TeV. The samples were then all showered through
131 PYTHIA8 (version 8.176) [18] using the default tune 4C
132 [19]. For each of the various samples (W,q,g) and p_T bins,
133 500,000 events were simulated.

134 2.2 Top tagging

135 Samples were generated at $\sqrt{s} = 14$ TeV. Standard Model
136 dijet and top pair samples were produced with SHERPA 2.0.Q75
137 [20–25], with matrix elements of up to two extra partons
138 matched to the shower. The top samples included only hadronic
139 decays and were generated in exclusive p_T bins of width
140 100 GeV, taking as slicing parameter the maximum of the
141 top/anti-top p_T . The QCD samples were generated with a
142 cut on the leading parton-level jet p_T , where parton-level
143 jets are clustered with the anti- k_t algorithm and jet radii of
144 $R = 0.4, 0.8, 1.2$. The matching scale is selected to be $Q_{\text{cut}} =$
145 40, 60, 80 GeV for the $p_{T,\text{min}} = 600, 1000, \text{ and } 1500$ GeV bins
146 respectively. For the top samples, 100k events were gener-
147 ated in each bin, while 200k QCD events were generated in
148 each bin.

3 Jet Algorithms and Substructure Observables

150 In this section, we define the jet algorithms and observables
151 used in our analysis. Over the course of our study, we con-
152 sidered a larger set of observables, but for the final analysis,
153 we eliminated redundant observables for presentation pur-
154 poses. In Sections 3.1, 3.2, 3.3 and 3.4 we first describe the
various jet algorithms, groomers, taggers and other substruc-
ture variables used in these studies.

3.1 Jet Clustering Algorithms

Jet clustering: Jets were clustered using sequential jet clus-
tering algorithms [26] implemented in FASTJET 3.0.3. Final
state particles i, j are assigned a mutual distance d_{ij} and a
distance to the beam, d_{iB} . The particle pair with smallest d_{ij}
are recombined and the algorithm repeated until the small-
est distance is instead the distance to the beam, d_{iB} , in which
case i is set aside and labelled as a jet. The distance metrics
are defined as

$$d_{ij} = \min(p_{Ti}^{2\gamma}, p_{Tj}^{2\gamma}) \frac{\Delta R_{ij}^2}{R^2}, \quad (1)$$

$$d_{iB} = p_{Ti}^{2\gamma}, \quad (2)$$

where $\Delta R_{ij}^2 = (\Delta\eta)^2 + (\Delta\phi)^2$. In this analysis, we use the
anti- k_t algorithm ($\gamma = -1$) [27], the Cambridge/Aachen (C/A)
algorithm ($\gamma = 0$) [28, 29], and the k_t algorithm ($\gamma = 1$)
[30, 31], each of which has varying sensitivity to soft ra-
diation in defining the jet.

Qjets: We also perform non-deterministic jet clustering [32,
33]. Instead of always clustering the particle pair with small-
est distance d_{ij} , the pair selected for combination is chosen
probabilistically according to a measure

$$P_{ij} \propto e^{-\alpha(d_{ij}-d_{\text{min}})/d_{\text{min}}}, \quad (3)$$

where d_{min} is the minimum distance for the usual jet clus-
tering algorithm at a particular step. This leads to a differ-
ent cluster sequence for the jet each time the Qjet algorithm
is used, and consequently different substructure properties.
The parameter α is called the rigidity and is used to control
how sharply peaked the probability distribution is around the
usual, deterministic value. The Qjets method uses statistical
analysis of the resulting distributions to extract more infor-
mation from the jet than can be found in the usual cluster
sequence.

3.2 Jet Grooming Algorithms

Pruning: Given a jet, re-cluster the constituents using the
C/A algorithm. At each step, proceed with the merger as

usual unless both

$$\frac{\min(p_{T_i}, p_{T_j})}{p_{T_{ij}}} < z_{\text{cut}} \text{ and } \Delta R_{ij} > \frac{2m_j}{p_{T_j}} R_{\text{cut}}, \quad (4)$$

in which case the merger is vetoed and the softer branch discarded. The default parameters used for pruning [34] in this study are $z_{\text{cut}} = 0.1$ and $R_{\text{cut}} = 0.5$. One advantage of pruning is that the thresholds used to veto soft, wide-angle radiation scale with the jet kinematics, and so the algorithm is expected to perform comparably over a wide range of momenta.

Trimming: Given a jet, re-cluster the constituents into subsets of radius R_{trim} with the k_t algorithm. Discard all subjects i with

$$p_{T_i} < f_{\text{cut}} p_{T_j}. \quad (5)$$

The default parameters used for trimming [35] in this study are $R_{\text{trim}} = 0.2$ and $f_{\text{cut}} = 0.03$.

Filtering: Given a jet, re-cluster the constituents into subsets of radius R_{filt} with the C/A algorithm. Re-define the jet to consist of only the hardest N subjects, where N is determined by the final state topology and is typically one more than the number of hard prongs in the resonance decay (to include the leading final-state gluon emission) [36]. While we do not independently use filtering, it is an important step of the HEPTopTagger to be defined later.

Soft drop: Given a jet, re-cluster all of the constituents using the C/A algorithm. Iteratively undo the last stage of the C/A clustering from j into subjects j_1, j_2 . If

$$\frac{\min(p_{T_1}, p_{T_2})}{p_{T_1} + p_{T_2}} < z_{\text{cut}} \left(\frac{\Delta R_{12}}{R} \right)^\beta, \quad (6)$$

discard the softer subject and repeat. Otherwise, take j to be the final soft-drop jet [37]. Soft drop has two input parameters, the angular exponent β and the soft-drop scale z_{cut} with default value $z_{\text{cut}} = 0.1$.

3.3 Jet Tagging Algorithms

Modified Mass Drop Tagger: Given a jet, re-cluster all of the constituents using the C/A algorithm. Iteratively undo the last stage of the C/A clustering from j into subjects j_1, j_2 with $m_{j_1} > m_{j_2}$. If either

$$m_{j_1} > \mu m_j \text{ or } \frac{\min(p_{T_1}^2, p_{T_2}^2)}{m_j^2} \Delta R_{12}^2 < y_{\text{cut}}, \quad (7)$$

then discard the branch with the smaller transverse mass $m_T = \sqrt{m_i^2 + p_{T_i}^2}$, and re-define j as the branch with the

larger transverse mass. Otherwise, the jet is tagged. If de-clustering continues until only one branch remains, the jet is considered to have failed the tagging criteria [38]. In this study we use by default $\mu = 1.0$ (i.e. implement no mass drop criteria) and $y_{\text{cut}} = 0.1$.

Johns Hopkins Tagger: Re-cluster the jet using the C/A algorithm. The jet is iteratively de-clustered, and at each step the softer prong is discarded if its p_T is less than $\delta_p p_{T_{\text{jet}}}$. This continues until both prongs are harder than the p_T threshold, both prongs are softer than the p_T threshold, or if they are too close ($|\Delta \eta_{ij}| + |\Delta \phi_{ij}| < \delta_R$); the jet is rejected if either of the latter conditions apply. If both are harder than the p_T threshold, the same procedure is applied to each: this results in 2, 3, or 4 subjects. If there exist 3 or 4 subjects, then the jet is accepted: the top candidate is the sum of the subjects, and W candidate is the pair of subjects closest to the W mass [12]. The output of the tagger is m_t, m_W , and θ_h , a helicity angle defined as the angle, measured in the rest frame of the W candidate, between the top direction and one of the W decay products. The two free input parameters of the John Hopkins tagger in this study are δ_p and δ_R , defined above.

HEPTopTagger: Re-cluster the jet using the C/A algorithm. The jet is iteratively de-clustered, and at each step the softer prong is discarded if $m_1/m_{12} > \mu$ (there is not a significant mass drop). Otherwise, both prongs are kept. This continues until a prong has a mass $m_i < m$, at which point it is added to the list of subjects. Filter the jet using $R_{\text{filt}} = \min(0.3, \Delta R_{ij})$, keeping the five hardest subjects (where ΔR_{ij} is the distance between the two hardest subjects). Select the three subjects whose invariant mass is closest to m_t [11]. The output of the tagger is m_t, m_W , and θ_h (defined above). The two free input parameters of the HEPTopTagger in this study are m and μ , defined above.

Top Tagging with Pruning or Trimming: For comparison with the other top taggers, we add a W reconstruction step to the pruning and trimming algorithms described above. A W candidate is found as follows: if there are two subjects, the highest-mass subject is the W candidate (because the W prongs end up clustered in the same subject); if there are three subjects, the two subjects with the smallest invariant mass comprise the W candidate. In the case of only one subject, no W is reconstructed.

3.4 Other Jet Substructure Observables

Jet substructure observables are calculated using jet constituents prior to any grooming.

Qjet mass volatility: As described above, Qjet algorithms re-cluster the same jet non-deterministically to obtain a collection of interpretations of the jet. For each jet interpretation, the pruned jet mass is computed with the default pruning parameters. The mass volatility, Γ_{Qjet} , is defined as [32]

$$\Gamma_{\text{Qjet}} = \frac{\sqrt{\langle m_J^2 \rangle - \langle m_J \rangle^2}}{\langle m_J \rangle}, \quad (8)$$

where averages are computed over the Qjet interpretations. We use a rigidity parameter of $\alpha = 0.1$ (although other studies suggest a smaller value of α may be optimal [32, 33]), and 25 trees per event for all of the studies presented here.

N -subjettiness: N -subjettiness [39] quantifies how well the radiation in the jet is aligned along N directions. To compute N -subjettiness, $\tau_N^{(\beta)}$, one must first identify N axes within the jet. Then,

$$\tau_N = \frac{1}{d_0} \sum_i p_{Ti} \min(\Delta R_{1i}^\beta, \dots, \Delta R_{Ni}^\beta), \quad (9)$$

where distances are between particles i in the jet and the axes,

$$d_0 = \sum_i p_{Ti} R^\beta \quad (10)$$

and R is the jet clustering radius. The exponent β is a free parameter. There is also some choice in how the axes used to compute N -subjettiness are determined. The optimal configuration of axes is the one that minimizes N -subjettiness; recently, it was shown that the ‘‘winner-takes-all’’ (WTA) axes can be easily computed and have superior performance compared to other minimization techniques [40]. We use both the WTA and one-pass k_t optimization axes in our analyses.

A more powerful discriminant is often the ratio,

$$\tau_{N,N-1} \equiv \frac{\tau_N}{\tau_{N-1}}. \quad (11)$$

While this is not an infrared-collinear (IRC) safe observable it is calculable [41] and can be made IRC safe with a loose lower cut on τ_{N-1} .

Energy correlation functions: The transverse momentum version of the energy correlation functions are defined as [42]:

$$\text{ECF}(N, \beta) = \sum_{i_1 < i_2 < \dots < i_N \in j} \left(\prod_{a=1}^N p_{Ti_a} \right) \left(\prod_{b=1}^{N-1} \prod_{c=b+1}^N \Delta R_{i_b i_c} \right)^\beta \quad (12)$$

where i is a particle inside the jet. It is preferable to work in terms of dimensionless quantities, particularly the energy correlation function double ratio:

$$C_N^{(\beta)} = \frac{\text{ECF}(N+1, \beta) \text{ECF}(N-1, \beta)}{\text{ECF}(N, \beta)^2}. \quad (13)$$

This observable measures higher-order radiation from leading-order substructure. Note that $C_2^{(0)}$ is identical to the variable PTD introduced by CMS in [43].

4 Multivariate Analysis Techniques

Multivariate techniques are used to combine variables into an optimal discriminant, and the extent to which the discrimination power increases when this is done is used to indicate how much the discriminatory information present in the variables overlaps. An alternative strategy for studying correlations in discrimination power that is not explored here is ‘‘truth matching’’ [44].

In all cases the multivariate technique used to combine variables is a boosted decision tree (BDT) as implemented in the TMVA package [45]. We use the BDT implementation including gradient boost. An example of the BDT settings are as follows:

- NTrees=1000
- BoostType=Grad
- Shrinkage=0.1
- UseBaggedGrad=F
- nCuts=10000
- MaxDepth=3
- UseYesNoLeaf=F
- nEventsMin=200

Exact parameter values are chosen to best reduce the effect of overtraining. Additionally, the simulated data were split into training and testing samples and comparisons of the BDT output were compared to reduced the effect of overtraining as well.

5 Quark-Gluon Discrimination

In this section, we examine the differences between quark- and gluon-initiated jets in terms of substructure variables, and to determine to what extent these variables are correlated. Along the way, we provide some theoretical understanding of these observables and their performance. The motivation for these studies comes not only from the desire to ‘‘tag’’ a jet as originating from a quark or gluon, but also to improve our understanding of the quark and gluon components of the QCD backgrounds relative to boosted resonances. While recent studies have suggested that quark/gluon

317 tagging efficiencies depend highly on the Monte Carlo gen-366
 318 erator used[46, 47], we are more interested in understanding367
 319 the scaling performance with p_T and R , and the correlations368
 320 between observables, which are expected to be treated con-369
 321 sistently within a single shower scheme. 370

322 5.1 Methodology 373

323 These studies use the qq and gg MC samples, described pre-374
 324 viously in Section 2. The showered events were clustered375
 325 with FASTJET 3.03 using the anti- k_T algorithm with jet radii376
 326 of $R = 0.4, 0.8, 1.2$. In both signal (quark) and background377
 327 (gluon) samples, an upper and lower cut on the leading jet378
 328 p_T is applied after showering/clustering, to ensure similar
 329 p_T spectra for signal and background in each p_T bin. The
 330 bins in leading jet p_T that are considered are 300-400 GeV,
 331 500-600 GeV, 1.0-1.1 TeV, for the 300-400 GeV, 500-600
 332 GeV, 1.0-1.1 TeV parton p_T slices respectively. Various jet
 333 grooming approaches are applied to the jets, as described in
 334 Section 3.4. Only leading and subleading jets in each sam-
 335 ple are used. The following observables are studied in this
 336 section: 380

- 337 – The number of constituents (N_{constits}) in the jet. 386
- 338 – The pruned Qjet mass volatility, Γ_{Qjet} . 387
- 339 – 1-point energy correlation functions, C_1^β with $\beta = 0, 1, 2$. 388
- 340 – 1-subjettiness, τ_1^β with $\beta = 1, 2$. The N -subjettiness axes 389
 341 are computed using one-pass k_t axis optimization. 390
- 342 – The ungroomed jet mass, m . 391

343 We will see below that, in terms of their jet-by-jet corre-393
 344 lations and their ability to separate quark initiated jets from394
 345 gluon initiated jets (hereafter called simply quark jets and395
 346 gluon jets), these observables fall into five classes. The first396
 347 three, N_{constits} , Γ_{Qjet} and $C_1^{\beta=0}$, form classes by themselves397
 348 (Classes I to III) in the sense that they each carry some inde-398
 349 pendent information about a jet and, when combined, pro-399
 350 vide substantially better quark jet and gluon jet separation400
 351 than either observable by itself. Of the remaining observ-401
 352 ables, $C_1^{\beta=1}$ and $\tau_1^{\beta=1}$ comprise a single class (Class IV)402
 353 in the sense that they exhibit similar distributions when ap-403
 354 plied to a sample of jets, their jet-by-jet values are highly404
 355 correlated, they exhibit very similar power to separate quark405
 356 jets and gluon jets (with very similar dependence on the jet406
 357 parameters R and p_T) and this separation power is essen-407
 358 tially unchanged when they are combined. The fifth class408
 359 (Class V) is composed of $C_1^{\beta=2}$, $\tau_1^{\beta=2}$ and the (ungroomed)409
 360 jet mass. Again the issue is that jet-by-jet correlations are410
 361 strong (even though the individual observable distributions411
 362 are somewhat different), quark versus gluon separation power412
 363 is very similar (including the R and p_T dependence) and lit-413
 364 tle is achieved by combining more than one of these ob-414
 365 servables. This class structure is not surprising given that415

within a class the observables exhibit very similar depen-
 dence on the kinematics of the underlying jet constituents.
 For example, the members of Class V are constructed from
 of a sum over pairs of constituents using products of the en-
 ergy of each member of the pair times the angular separation
 squared for the pair (for the mass case think in terms of mass
 squared with small angular separations). By the same argu-
 ment the Class IV and Class V observables will be seen to
 be more similar than any other pair of classes, differing only
 in the power (β) of the dependence on the angular separa-
 tions, which will produce small but detectable differences.
 We will return to a more complete discussion of jet masses
 at the end of Section 5.

5.2 Single Variable Discrimination

The quark and gluon distributions of different substructure
 observables are shown in Figure 1, which already illustrates
 at least some of the points about the Classes made above. At
 a fundamental level the primary difference between quark
 jets and gluon jets is the color charge of the initiating parton,
 typically expressed in terms of the ratio of the correspond-
 ing Casimir factors $C_F/C_A = 4/9$. Since the quark has the
 smaller color charge, it will radiate less than a corresponding
 gluon and the resulting jet will contain fewer constituents.
 This difference is clearly indicated in Figure 1(a), suggest-
 ing that simply counting constituents will provide good sep-
 aration between quark and gluon jets. In fact, among the ob-
 servables considered, one can see by eye that N_{constits} should
 provide the highest separation power, *i.e.*, the quark and gluon
 distributions are most distinct, as was originally noted in
 [47, 48]. Figure 1 further suggests that $C_1^{\beta=0}$ should pro-
 vide the next best separation followed by $C_1^{\beta=1}$, as was also
 found by the CMS and ATLAS Collaborations[46, 49].

To more quantitatively study the power of each observ-
 able as a discriminator for quark/gluon tagging, ROC curves
 are built by scanning each distribution and plotting the back-
 ground efficiency (to select gluon jets) vs. the signal ef-
 ficiency (to select quark jets). Figure 2 shows these ROC
 curves for all of the substructure variables shown in Fig-
 ure 1, along with the ungroomed mass, representing the best
 performing mass variable, for $R=0.4, 0.8$ and 1.2 jets in
 the $p_T = 300 - 400$ GeV bin. In addition, the ROC curve
 for a tagger built from a BDT combination of all the vari-
 ables (see Section 4) is shown. Clearly, and as suggested ear-
 lier, n_{constits} is the best performing variable for all R s, even
 though $C_1^{\beta=0}$ is close, particularly for $R=0.8$. Most other
 variables have similar performance, except Γ_{Qjet} , which shows
 significantly worse discrimination (this may be due to our
 choice of rigidity $\alpha = 0.1$, with other studies suggesting that
 a smaller value, such as $\alpha = 0.01$, produces better results[32,
 33]). The combination of all variables shows somewhat bet-

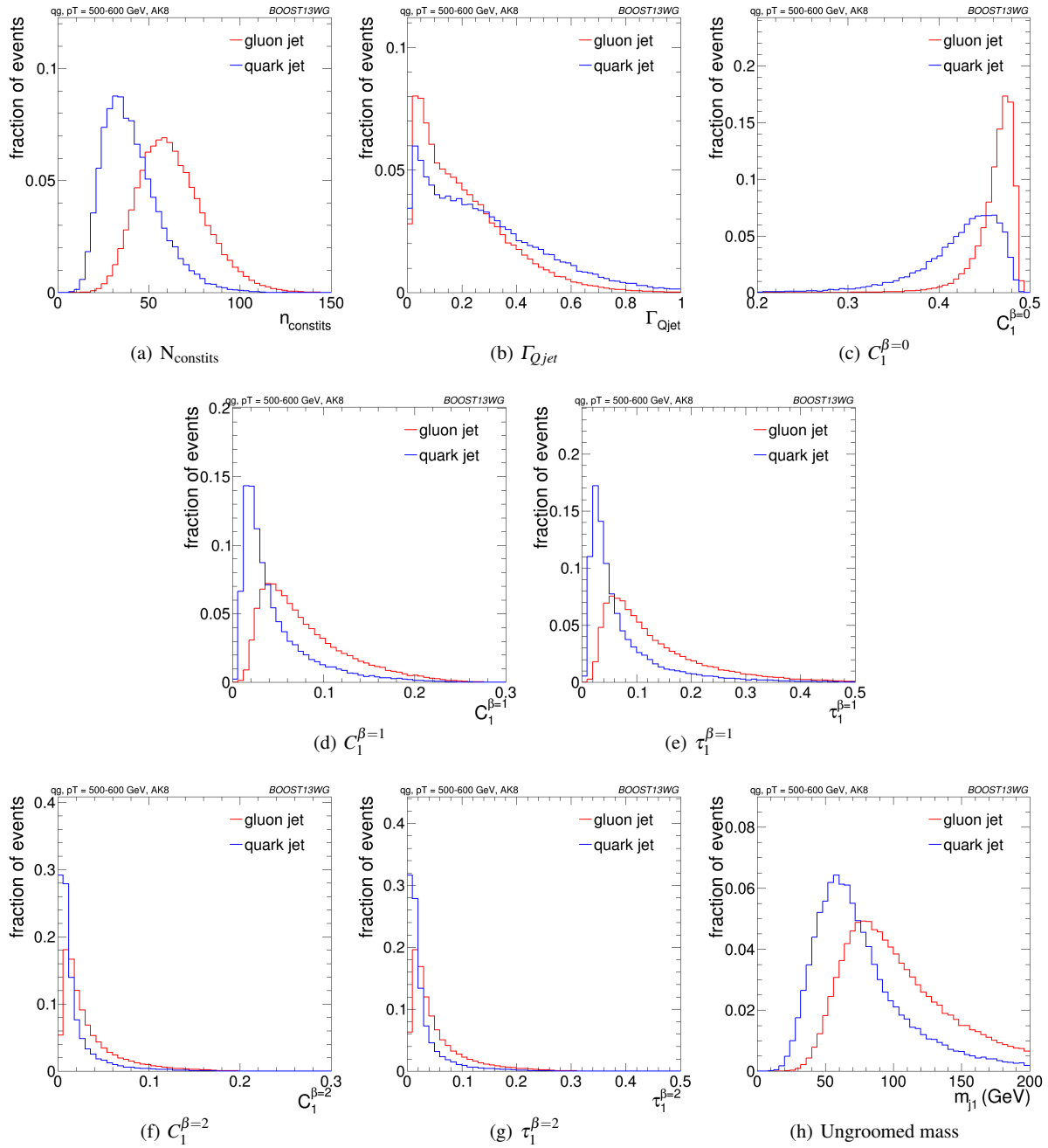


Fig. 1 Comparisons of quark and gluon distributions of different substructure variables (organized by Class) for leading jets in the $p_T = 500 - 600$ GeV bin using the anti- k_T $R = 0.8$ algorithm.

416 ter discrimination, and we will discuss in more detail below 425
 417 the correlations between the observables and their impact on 426
 418 the combined discrimination power. 427

419 We now examine how the performance of the substructure 428
 420 observables changes with p_T and R . To present the results 429
 421 in a “digestible” fashion we will focus on the gluon 430
 422 jet “rejection” factor, $1/\varepsilon_{\text{bkg}}$, for a quark signal efficiency, 431
 423 ε_{sig} , of 50%. We can use the values of $1/\varepsilon_{\text{bkg}}$ generated for 432
 424 the 9 kinematic points introduced above ($R = 0.4, 0.8, 1.2$ 433

and the 100 GeV p_T bins with lower limits $p_T = 300$ GeV, 434
 500 GeV, 1000 GeV) to generate surface plots. The surface 435
 plots in Figure 3 indicate both the level of gluon rejection 436
 and the variation with p_T and R for each of the studied single 437
 observable. The color shading is defined so that a change 438
 in color corresponds to a change of about 0.4 in $1/\varepsilon_{\text{bkg}}$. 439
 The colors have the same correlation with the magnitude of 440
 $1/\varepsilon_{\text{bkg}}$ in all of the plots, but repeat after a change of about 441
 4. Thus “blue” corresponds to a value of about 2.5 in Fig- 442

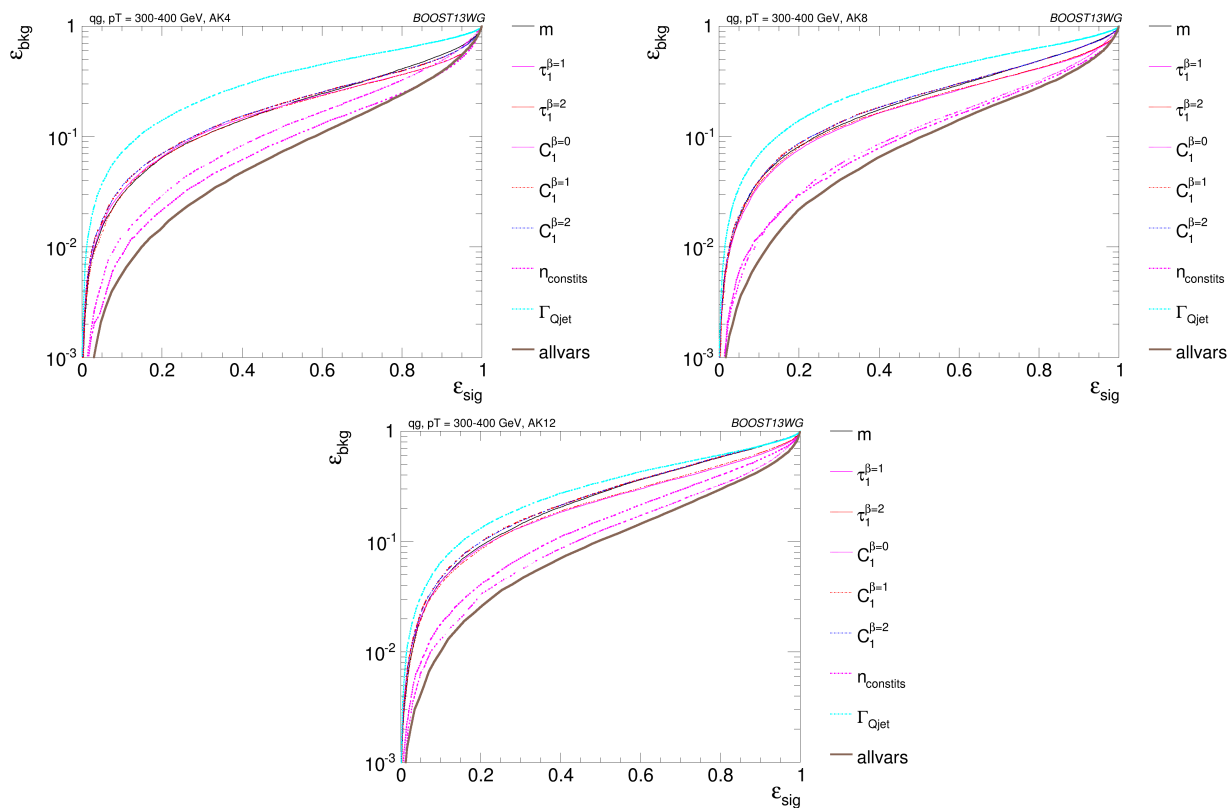


Fig. 2 The ROC curve for all single variables considered for quark-gluon discrimination in the p_T 300-400 GeV bin using the anti- k_T $R=0.4, 0.8$ and 1.2 algorithm.

434 ure 3(b) and the values 6.5 and 10.5 in Figure 3(a), while 459
 435 "yellow" corresponds to about 5 in Figures 3(c) to (h) and 460
 436 about 9 in Figure 3(a). 461

437 We see, as expected, that the numerically largest rejection 462
 438 rates occur for the observable $N_{\text{constituents}}$ in Figure 3(a), 463
 439 where the rejection factor is in the range 6 to 11 and varies 464
 440 rather dramatically with R . As R increases the jet collects 465
 441 more constituents from the underlying event, which are the 466
 442 same for quark and gluon jets, and the separation power de- 467
 443 creases. At large R , there is some improvement with increas- 468
 444 ing p_T due to the enhanced radiation, which does distinguish
 445 quarks from gluons. Figure 3(b) confirms the limited effi- 469
 446 cacy of the single observable I_{Qjet} (at least for our param- 470
 447 eter choices) with a rejection rate only in the range 2.5 to 2.8 471
 448 On the other hand, this observable probes a very different 472
 449 property of jet substructure, *i.e.*, the sensitivity to detailed 473
 450 changes in the grooming procedure, and this difference is 474
 451 suggested by the distinct R and p_T dependence illustrated 475
 452 in Figure 3(b). The rejection rate increases with increasing 476
 453 R and decreasing p_T , since the distinction between quark 477
 454 and gluon jets for this observable arises from the relative 478
 455 importance of the one "hard" gluon emission configuration 479
 456 The role of this contribution is enhanced for both decreasing 480
 457 p_T and increasing R . Figure 3(c) indicates that the observ- 481
 458 able $C_1^{\beta=0}$ can, by itself, provide a rejection rate in the rang 482

7.8 to 8.6 (intermediate between the two previous observ-
 ables) and again with distinct R and p_T dependence. In this
 case the rejection rate decreases slowly with increasing R
 ($\beta = 0$ explicitly means that the angular dependence is much
 reduced), while the rejection rate peaks at intermediate p_T
 values (an effect visually enhanced by the limited number of
 p_T values included). Both the distinct values of the rejection
 rates and the differing R and p_T dependence serve to con-
 firm that these three observables tend to probe independent
 features of the quark and gluon jets.

Figures 3(d) and (e) serve to confirm the very similar
 properties of the Class IV observables $C_1^{\beta=1}$ and $\tau_1^{\beta=1}$ (as
 already suggested in Figures 1(d) and (e)) with essentially
 identical rejection rates (4.1 to 5.4) and identical R and p_T
 dependence (a slow decrease with increasing R and an even
 slower increase with increasing p_T). A similar conclusion
 for the Class V observables $C_1^{\beta=2}$, $\tau_1^{\beta=2}$ and m with similar
 rejection rates in the range 3.5 to 5.3 and very similar
 R and p_T dependence (a slow decrease with increasing R
 and an even slower increase with increasing p_T). Arguably,
 drawing a distinction between the Class IV and Class V ob-
 servables, is a fine point, but the color shading does sug-
 gest some distinction from the slightly smaller rejection rate
 in Class V. Again the strong similarities between the plots

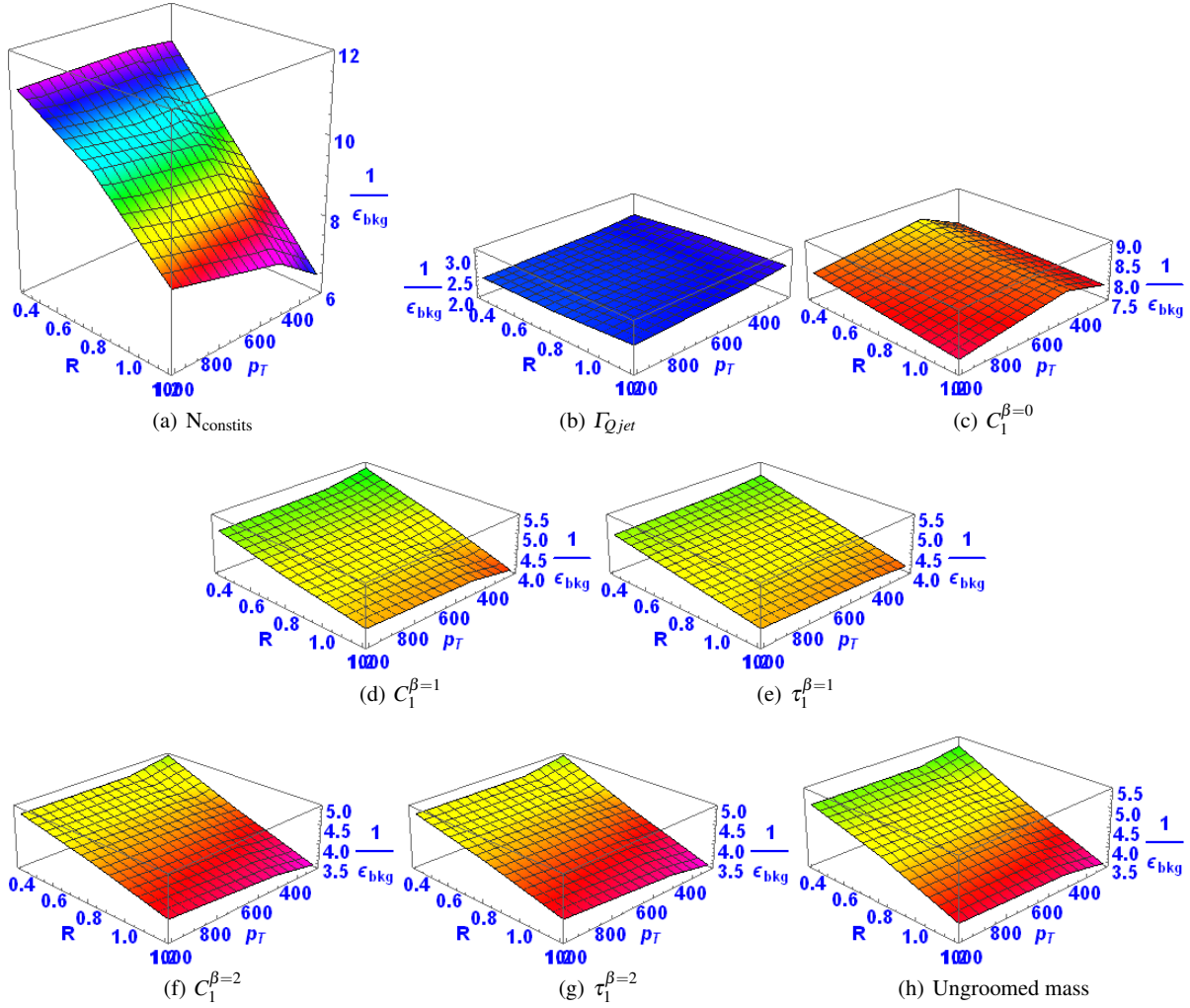


Fig. 3 Surface plots of $1/\epsilon_{\text{bkg}}$ for all single variables considered for quark-gluon discrimination as functions of R and p_T .

483 within the second and third rows in Figure 3 speaks to the
 484 common properties of the observables within the two classes.

485 In summary, the overall discriminating power between
 486 quark and gluon jets tends to decrease with increasing R
 487 except for the Γ_{Qjet} observable, presumably primarily due
 488 to the increasing contamination from the underlying event.
 489 Since the construction of the Γ_{Qjet} observable explicitly in-
 490 volves pruning away the soft, large angle constituents, it is
 491 not surprising that it exhibits different R dependence. In gen-
 492 eral the discriminating power increases slowly and mono-
 493 tonically with p_T (except for the Γ_{Qjet} and $C_1^{\beta=0}$ observ-
 494 ables) presumably because there is overall more (color charge
 495 related) radiation as p_T increasing providing some increas-
 496 in discrimination (except for the Γ_{Qjet} observable). We turn
 497 now to the question of the impact of employing more than
 498 one observable at a time.

5.3 Combined Performance and Correlations

500 The quark/gluon tagging performance can be further im-
 501 proved over cuts on single observables by combining mul-
 502 tiple observables in a BDT; due to the challenging nature
 of q/g -tagging, any improvement in performance with mul-
 tivariable techniques could be critical for certain analyses,
 and the improvement could be more substantial in data than
 the marginal benefit found in MC and shown in Fig. 2. Fur-
 thermore, insight can be gained into the features allowing
 for quark/gluon discrimination if the origin of the improve-
 ment is understood. To quantitatively study this improve-
 ment, we build quark/gluon taggers from every pair-wise
 combination of variables studied in the previous section for
 comparison with the all-variable combination. To illustrate
 the results achieved in this way we will exhibit the same
 sort 2D of surface plots as in Figure 3. Based on our dis-
 cussion of the correlated properties of observables within a
 single class, we expect little improvement in the rejection

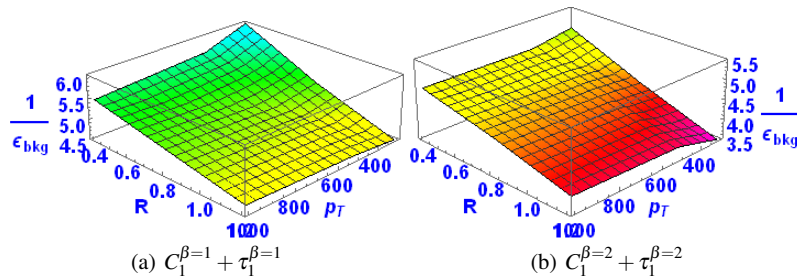


Fig. 4 Surface plots of $1/\epsilon_{\text{bkg}}$ for the indicated pairs of variables from Classes IV and V considered for quark-gluon discrimination as functions of R and p_T .

rate when combining observables from the same class and
substantial improvement when combining observables from
different classes.

Figure 4 shows pairwise plots for (a) Class IV and (b)
Class V. Comparing to the corresponding plots in Figure 3
we see that combining $C_1^{\beta=1} + \tau_1^{\beta=1}$ provides a small im-
provement in the rejection rate of about 10% (0.5 out of
5) with essentially no change in the R and p_T dependence,
while combining $C_1^{\beta=2} + \tau_1^{\beta=2}$ yields a rejection rate that is
essentially identical to the single observable rejection rate
for all R and p_T values (with a similar conclusion if one of
these observables is replaced with the ungroomed jet mass
 m). This again confirms that expectation that the observables
within a single class effectively probe the *same* jet proper-
ties.

Next we consider the cross-class pairs of observables in-
dicated in Figure 5, where only one member of Classes IV
and V is included. As expected the largest rejection rates are
obtained from combining another observable with N_{constits}
(Figures 5(a) to (d)). In general, the rates are larger than
for the single variable case with similar R and p_T depen-
dence. In particular, the pair $N_{\text{constits}} + C_1^{\beta=1}$ yields rejection
rates in the range 6.4 to 14.7 (6.4 to 15 for the similar case
 $N_{\text{constits}} + \tau_1^{\beta=1}$) with the largest values at small R and large
 p_T . The other pairings with N_{constits} (except with $\tau_1^{\beta=1}$) yield
smaller rejection rates and smaller dynamic range. The pair
 $N_{\text{constits}} + C_1^{\beta=0}$ (Figure 5(d)) exhibits the smallest range of
rates (8.3 to 11.3) suggesting that the differences between
these two observables serve to substantially reduce the R
and p_T dependence for the pair, but this also reduces the
possible optimization. The other pairs indicated exhibit sim-
ilar behavior. The pair rejection rates are somewhat better
than either observable alone (since we are always combin-
ing from different classes), and the R and p_T dependence is
generally similar to the more variant single observable case.
The smallest R and p_T variation always occurs when pairing
with $C_1^{\beta=0}$. Changing any of the observables in these pairs
with a different observable in the same class (e.g., $C_1^{\beta=2}$ for
 $\tau_1^{\beta=2}$ produces very similar results (at the few percent level)

Figure 5(k) shows the result of a BDT analysis including all
of the current observables with rejection rates in the range
10.5 to 17.1. This is a somewhat narrower range than in Fig-
ure 5(b) but with somewhat larger maximum values.

Another way to present the same data but by fixing R
and p_T and showing all single observables and pairs of ob-
servables at once is in terms of the “matrices” indicated in
Figures 6 and 7. The numbers in each cell are the now fami-
liar rejection factor values of $1/\epsilon_{\text{bkg}}$ (gluons) for $\epsilon_{\text{sig}} = 50\%$
(quarks). Figure 6 corresponds $p_T = 1 - 1.1$ TeV and $R =$
0.4, 0.8, 1.2, while Figure 7 is for $R = 0.4$ and the 3 p_T bins.
The actual numbers should be familiar from the discussion
above with the single observable rejections rates appearing
on the diagonal and the pairwise results off the diagonal.
The correlations indicated by the shading should be largely
understood as indicating the organization of the observables
into the now familiar classes. The all-observable (BDT) re-
sult appears as the number at the lower right in each plot.

5.4 QCD Jet Masses

To close the discussion of the tagging of jets as either quark
jets or gluon jets we provide some insight into the behav-
ior of the masses of such QCD jets, both with and without
grooming. Recall that, in practice, an identified jet is simply
a list of constituents, *i.e.*, final state particles. To the extent
that the masses of these individual constituents are irrelev-
ant, typically because the detected constituents are rela-
tivistic, each constituent has a “well” defined 4-momentum.
It follows that the 4-momentum of the jet is simply the sum
of the 4-momenta of the constituents and its square is the
jet mass squared. We have already seen one set of jet mass
distributions in Figure 1(h) for quark and gluon jets found
with the anti- k_T algorithm with $R = 0.8$ and p_T in the bin
500-600 GeV. If we consider the mass distributions for other
kinematic points (other values of R and p_T), we observe
considerable variation but that variation can largely be re-
moved by plotting versus the scaled variable $m/p_T/R$. Sim-
ply on dimensional grounds we know that jet mass must
scale essentially linearly with p_T , with the remaining p_T

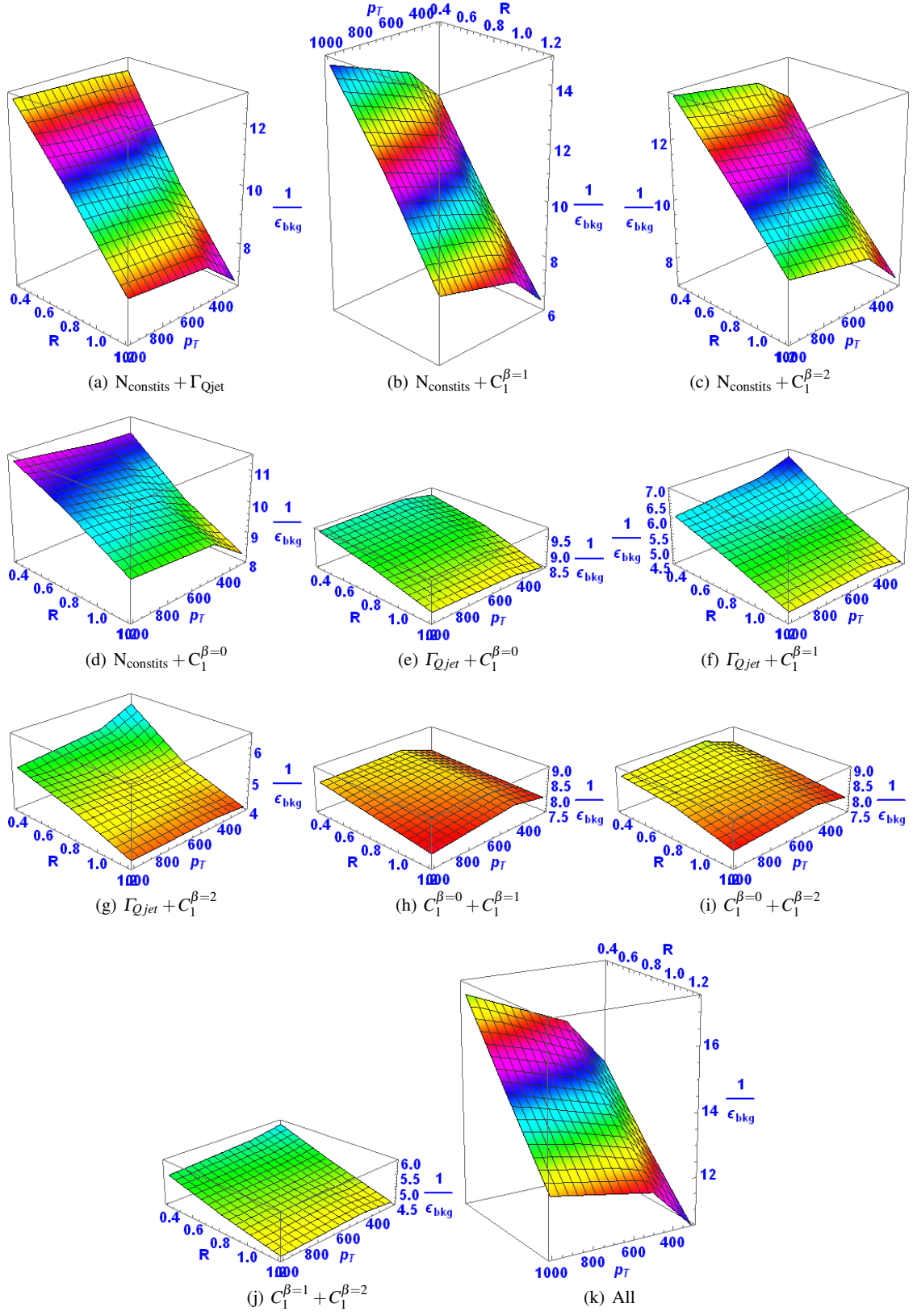


Fig. 5 Surface plots of $1/\epsilon_{\text{bkg}}$ for the indicated pairs of variables from different classes considered for quark-gluon discrimination as functions of R and p_T .

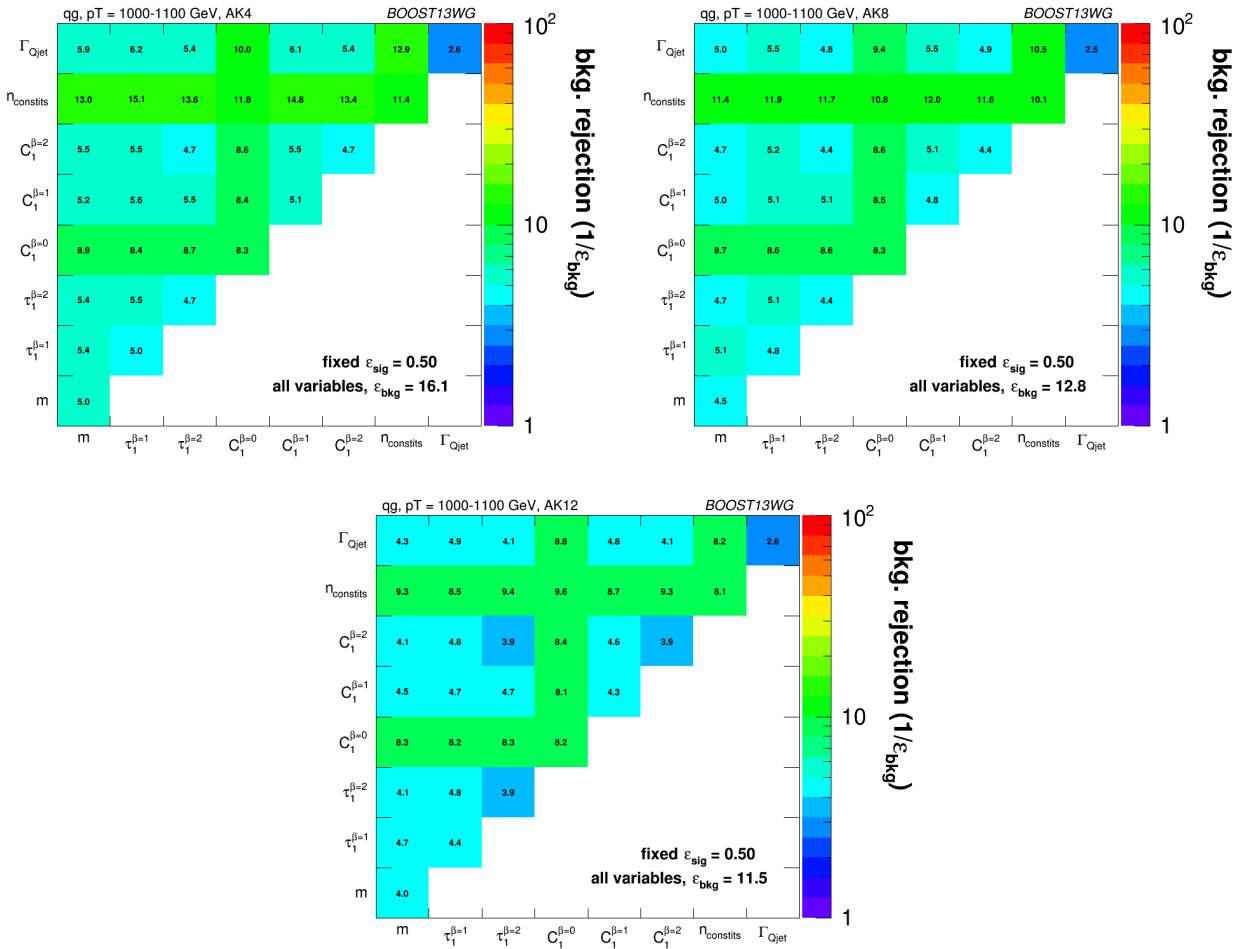


Fig. 6 Gluon rejection defined as $1/\varepsilon_{\text{gluon}}$ when using each 2-variable combination as a tagger with 50% acceptance for quark jets. Results are shown for jets with $p_T = 1 - 1.1$ TeV and for (top left) $R = 0.4$; (top right) $R = 0.8$; (bottom) $R = 1.2$. The rejection obtained with a tagger that uses all variables is also shown in the plots.

dependence arising predominantly from the running of the coupling, $\alpha_s(p_T)$. The R dependence is also crudely linear as the mass scales approximately with the largest angular opening between any 2 constituents and that is set by R . The mass distributions for quark and gluon jets versus $m/p_T/R$ for all of our kinematic points are indicated in Figure 8, where we use a logarithmic scale on the y-axis to clearly exhibit the behavior of these distributions over a large dynamic range. We observe that the distributions for the different kinematic points do approximately scale, *i.e.* the simple arguments above do capture most of the variation with R and p_T . We will consider shortly an explanation of the residual non-scaling. A more quantitative understanding of jet mass distributions requires all-orders calculations in QCD, which have been performed for ungroomed jet mass spectra at high logarithmic accuracy, both in the context of direct QCD resummation [50, 51] and Soft Collinear Effective Theory [52, 53].

Several features of Figure 8 can be easily understood. The distributions all cut-off rapidly for $m/p_T/R > 0.5$, which is understood as the precise limit (maximum mass) for a jet composed of just 2 constituents. As expected from the soft and collinear singularities in QCD, the mass distribution peaks at small mass values. The actual peak is “pushed” away from the origin by the so-called Sudakov form factor. Summing the corresponding logarithmic structure (singular in both p_T and angle) to all orders in perturbation theory yields a distribution that is highly damped as the mass vanishes. In words, there is precisely *zero* probability that a color parton emits *no* radiation (and the resulting jet has zero mass). The large mass “shoulder” ($0.3 < m/p_T/R < 0.5$) is driven largely by the presence of a single large angle, energetic emission in the underlying QCD shower, *i.e.*, this regime is quite well described by low-order perturbation theory. (The shoulder label will be more clear after we groom the jet.) In contrast, we should think of the peak region as corresponding to multiple soft emissions. This simple (ap-

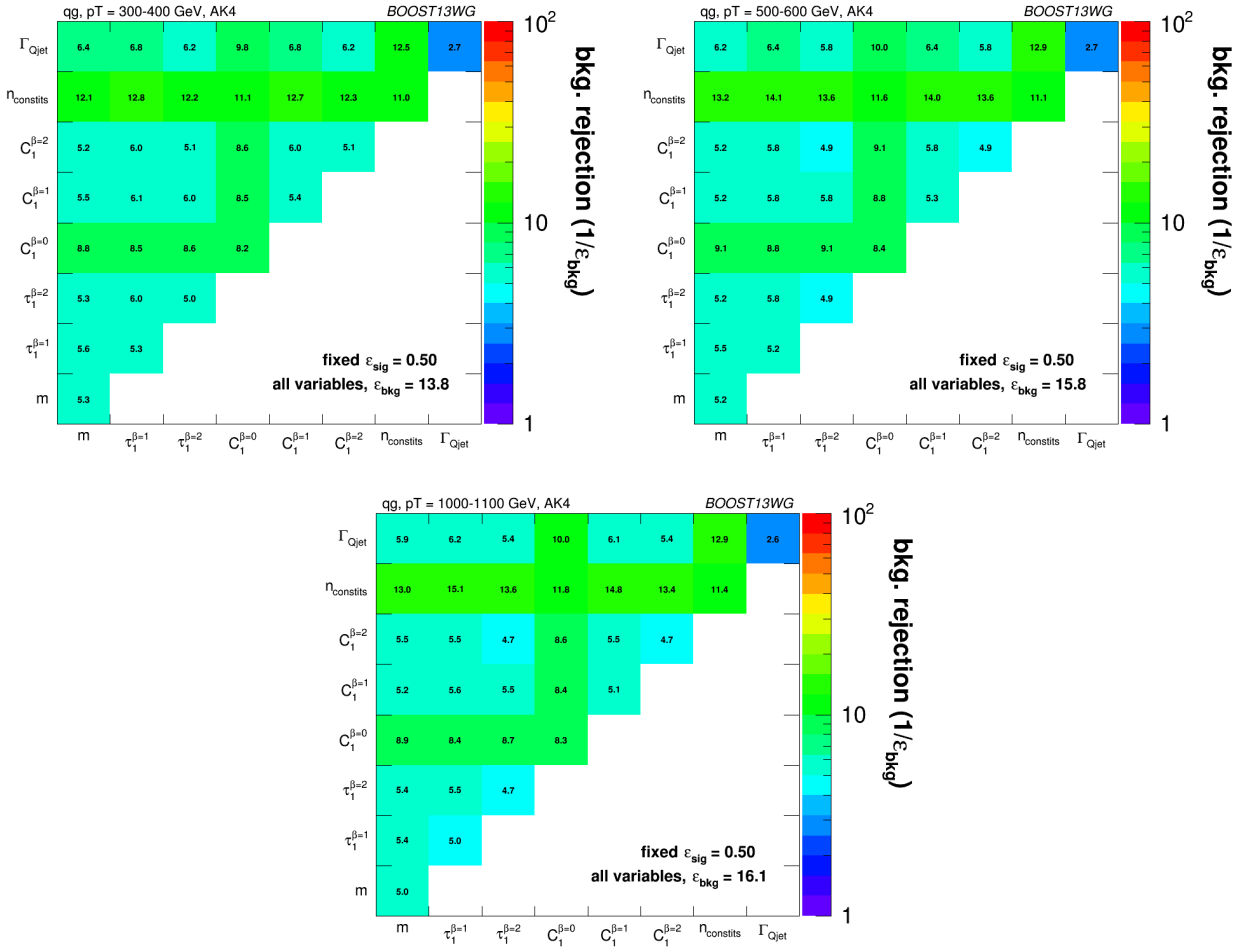


Fig. 7 Gluon rejection defined as $1/\epsilon_{\text{gluon}}$ when using each 2-variable combination as a tagger with 50% acceptance for quark jets. Results are shown for $R=0.4$ jets with (top left) $p_T = 300 - 400$ GeV, (top right) $p_T = 500 - 600$ GeV and (bottom) $p_T = 1 - 1.1$ TeV. The rejection obtained with a tagger that uses all variables is also shown in the plots.

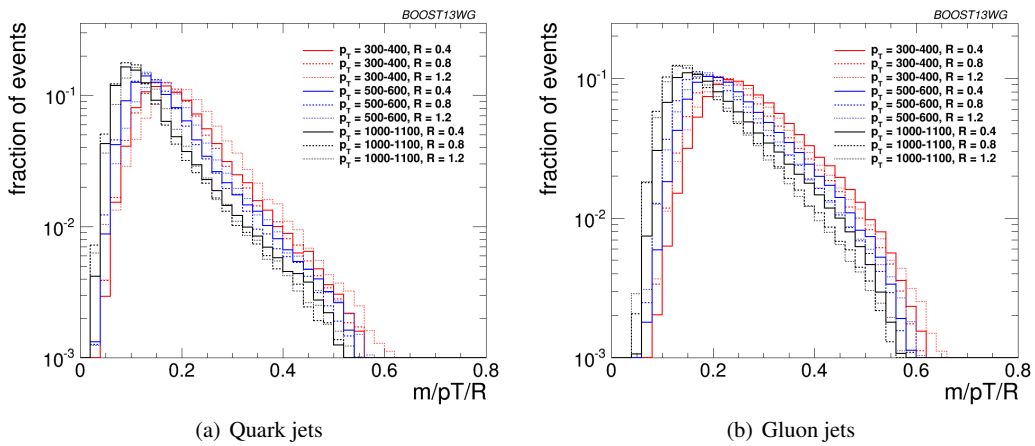


Fig. 8 Comparisons of quark and gluon ungroomed mass distributions versus the scaled variable $m/p_T/R$.

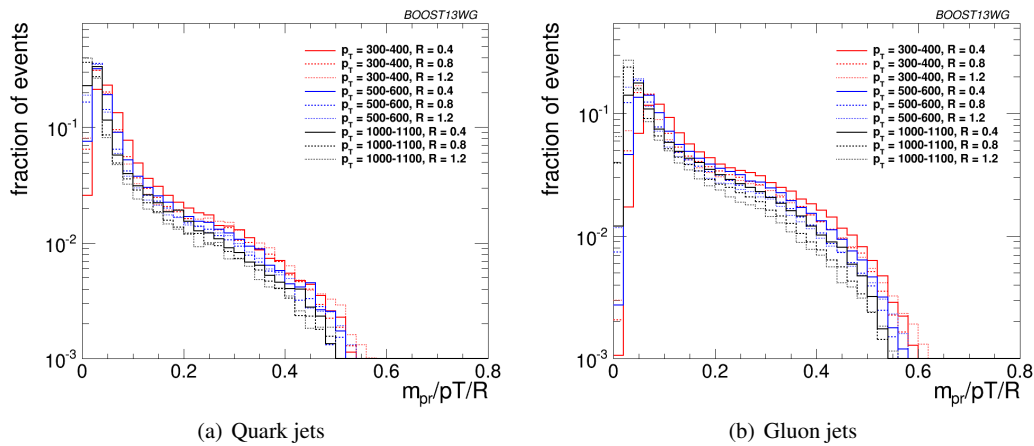


Fig. 9 Comparisons of quark and gluon pruned mass distributions versus the scaled variable $m_{pr}/p_T/R$.

proximate) picture provides an understanding of the bulk of the differences between the quark and gluon jet mass distributions. Since the probability of the single large angle, energetic emission is proportional to the color charge, the gluon distribution should be enhanced in this region by a factor of about $C_A/C_F = 9/4$, consistent with what is observed in Figure 8. Similarly the exponent in the Sudakov damping factor for the gluon jet mass distribution is enhanced by the same factor, leading to a peak “pushed” further from the origin. So the gluon jet mass distribution exhibits a larger average jet mass than the quark jet, with a larger relative contribution arising from the perturbative shoulder region. Recall also that the number of constituents in the jet is also larger (on average) for the gluon jet simply because a gluon will radiate more than a quark. These features explain much of what we observed earlier in terms of the effectiveness of the various observable to separate quark jets from gluon jets. Note in particular that the enhanced role of the shoulder for gluon jet explains, at least qualitatively, the difference in the distributions for the observable Γ_{Qjet} . Since the shoulder is dominated by a single large angle, hard emission, it is minimally impacted by pruning, which removes the large angle, soft constituents (as illustrated just below). Thus jets in the shoulder exhibit small volatility and they are a larger component in the gluon jet distribution. Hence gluon jets, on average, have smaller values of Γ_{Qjet} than quark jets as in Figure 1(b). Further this feature of gluon jets is distinct from fact that there are more constituents, which explains why Γ_{Qjet} and $N_{constits}$ supply largely independent information for distinguishing quark and gluon jets.

To illustrate some of these points in more detail, Figure 9 exhibits the jet mass distributions (of Figure 8) after pruning [34, 54]. Removing the large angle, soft constituents moves the peak in both of the distributions from $m/p_T/R \sim 0.1 - 0.2$ to the region around $m/p_T/R \sim 0.05$. This explains why pruning works to reduce the QCD back-

ground when looking for a signal in a specific jet mass bin. The “shoulder” feature is much more apparent after pruning, as is the larger shoulder for the gluon jets. A quantitative (all-orders) understanding of groomed mass distributions is also possible. For instance, resummation of the pruned mass distribution was achieved in [38, 55].

Our final topic in this section is the residual R and p_T dependence exhibited in Figures 8 and 9, where we are using the scaled variable $m/p_T/R$. As already suggested, the residual p_T dependence can be understood as arising primarily from the slow decrease of the strong coupling $\alpha_s(p_T)$ as p_T increases. This will lead to a corresponding decrease in the (largely perturbative) shoulder regime for both distributions as p_T increases. At the same time, and for the same reason, the Sudakov damping is less strong with increasing p_T and the peak moves towards the origin. Thus the overall impact of increasing p_T for both distributions is a (slow) shift to smaller values of $m/p_T/R$. This is just what is observed in Figures 8 and 9, although the numerical size of the effect is reduced in the pruned case. The R dependence is more complicated as there are effectively three different contributions to the mass distribution. The perturbative large angle, energetic single emission contribution largely scales in the variable $m/p_T/R$, which is why we see little residual R dependence in either figure for $m/p_T/R > 0.4$. The large angle soft emissions can both contribute at mass values that scale like R and increase in number as R increases (*i.e.*, as the area of the jet grows as R^2). Such contributions can yield a distribution that moves to the right as R increases and presumably explain the behavior at small p_T in Figure 8. Since pruning largely removes this contribution, we observe no such behavior in Figure 9. The contribution of small angle, soft emissions will be at fixed m values and thus shift to the left versus the scaled variable as R increases. This presumably explains the small shifts in this direction observed in both figures.

5.5 Conclusions

In Section 5 we have seen that a variety of jet observables provide information about the jet that can be employed effectively to separately tag quark and gluon jets. Further, when used in combination, these observables can provide even better separation. We saw that the best performing single observable is simply the number of constituents in the jet, N_{constits} , while the largest further improvement comes from combining with $C_1^{\beta=1}$ (or $\tau_1^{\beta=1}$), but the smallest R and p_T dependence arises from combining with $C_1^{\beta=0}$. On the other hand, some of the commonly used observables are highly correlated and do not provide extra information and enhanced tagging when used together. We have both demonstrated these correlations and provided a discussion of the physics behind the structure of the correlation. In particular, using the jet mass as a specific example observable we have tried to explicitly explain the differences between jets initiated by both quarks and gluons.

6 Boosted W -Tagging

In this section, we study the discrimination of a boosted hadronically decaying W signal against a gluon background, comparing the performance of various groomed jet masses, substructure variables, and BDT combinations of groomed mass and substructure. A range of different distance parameters R for the anti- k_T jet algorithm are explored, as well as a variety of kinematic regimes (lead jet p_T 300-400 GeV, 500-600 GeV, 1.0-1.1 TeV). This allows us to determine the performance of observables as a function of jet radius and jet boost, and to see where different approaches may break down. The groomed mass and substructure variables are then combined in a BDT as described in Section 4, and the performance of the resulting BDT discriminant explored through ROC curves to understand the degree to which variables are correlated, and how this changes with jet boost and jet radius.

6.1 Methodology

These studies use the WW samples as signal and the $dijet$ gg as background, described previously in Section 2. Whilst only gluonic backgrounds are explored here, the conclusions as to the dependence of the performance and correlations on the jet boost and radius are not expected to be substantially different for quark backgrounds; we will see that the differences in the substructure properties of quark- and gluon-initiated jets, explored in the last section, are significantly smaller than the differences between W -initiated and gluon-initiated jets.

As in the q/g tagging studies, the showered events were clustered with FASTJET 3.03 using the anti- k_T algorithm with jet radii of $R = 0.4, 0.8, 1.2$. In both signal and background samples, an upper and lower cut on the leading jet p_T is applied after showering/clustering, to ensure similar p_T spectra for signal and background in each p_T bin. The bins in leading jet p_T that are considered are 300-400 GeV, 500-600 GeV, 1.0-1.1 TeV, for the 300-400 GeV, 500-600 GeV, 1.0-1.1 TeV parton p_T slices respectively. The jets then have various grooming approaches applied and substructure observables reconstructed as described in Section 3.4. The substructure observables studied in this section are:

- The ungroomed, trimmed (m_{trim}), and pruned (m_{prun}) jet masses.
- The mass output from the modified mass drop tagger (m_{mmdt}).
- The soft drop mass with $\beta = -1, 2$ (m_{sd}).
- 2-point energy correlation function ratio $C_2^{\beta=1}$ (we also studied $\beta = 2$ but do not show its results because it showed poor discrimination power).
- N -subjettiness ratio τ_2/τ_1 with $\beta = 1$ ($\tau_{21}^{\beta=1}$) and with axes computed using one-pass k_t axis optimization (we also studied $\beta = 2$ but did not show its results because it showed poor discrimination power).
- The pruned Qjet mass volatility, Γ_{Qjet} .

6.2 Single Variable Performance

In this section we will explore the performance of the various groomed jet mass and substructure variables in terms of discriminating signal and background. Since we have not attempted to optimise the grooming parameter settings of each grooming algorithm, we do not want to place too much emphasis here on the relative performance of the groomed masses, but instead concentrate on how their performance changes depending on the kinematic bin and jet radius considered.

Figure 10 compares the signal and background in terms of the different groomed masses explored for the anti- k_T $R=0.8$ algorithm in the p_T 500-600 GeV bin. One can clearly see that in terms of separating signal and background the groomed masses will be significantly more performant than the ungroomed anti- k_T $R=0.8$ mass. Figure 11 compares signal and background in the different substructure variables explored for the same jet radius and kinematic bin.

Figures 12, 13 and 14 show the single variable ROC curves compared to the ROC curve for a BDT combination of all the variables (labelled “allvars”), for each of the anti- k_T distance parameters considered in each of the kinematic bins. One can see that, in all cases, the “allvars” option is considerably better performant than any of the individual

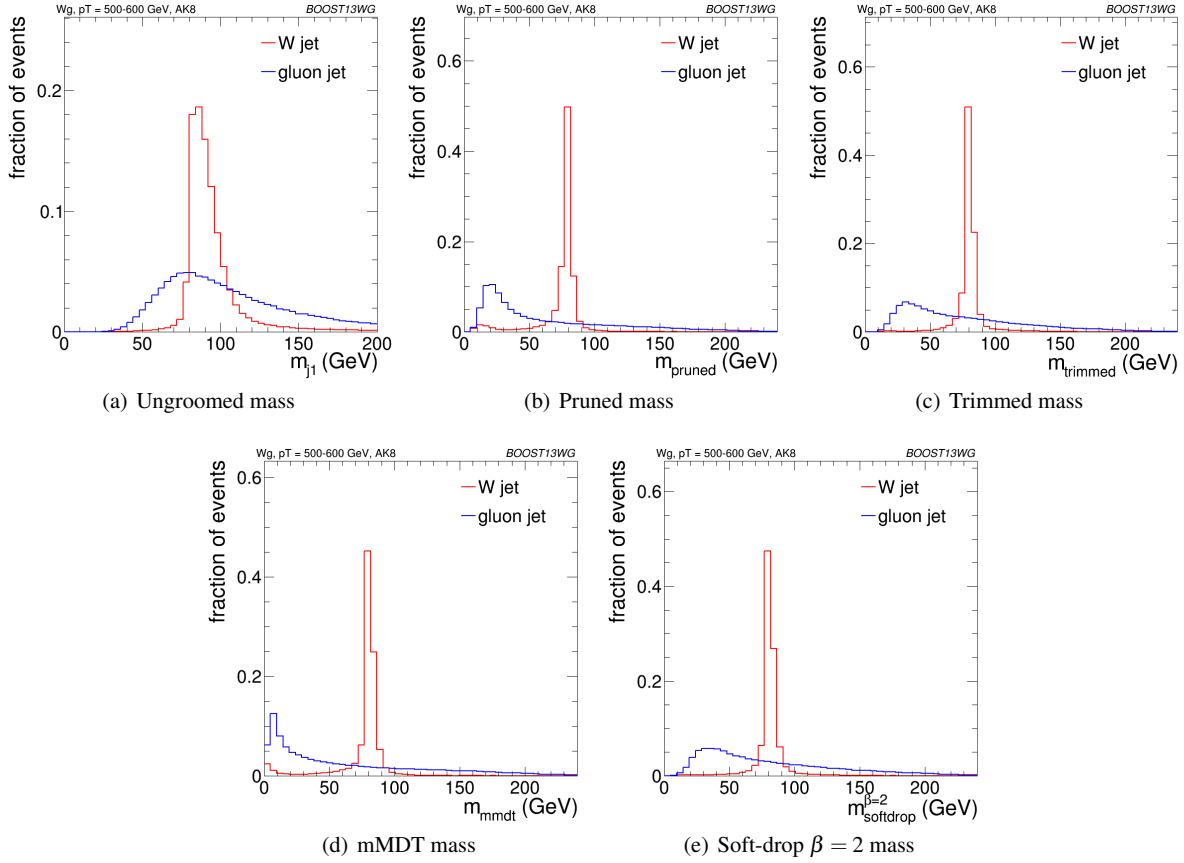


Fig. 10 Comparisons of the QCD background to the WW signal in the p_T 500-600 GeV bin using the anti- k_T $R=0.8$ algorithm: leading jet mass distributions.

single variables considered, indicating that there is considerable complementarity between the variables, and this will be explored further in the next section.

Although the ROC curves give all the relevant information, it is hard to compare performance quantitatively. Figures 15, 16 and 17 are shown matrices which give the background rejection for a signal efficiency of 70% when two variables (that on the x-axis and that on the y-axis) are combined in a BDT. These are shown separately for each p_T bin and jet radius considered. In the final column of these plots are shown the background rejection performance for three-variable BDT combinations of $m_{sd}^{\beta=2} + C_2^{\beta=1} + X$. These results will be discussed later in Section 6.3.3. The diagonal of these plots correspond to the background rejection for a single variable BDT, and can thus be examined to get a quantitative measure of the individual single variable performance, and to study how this changes with jet radius and momenta.

One can see that in general the most performant single variables are the groomed masses. However, in certain kinematic bins and for certain jet radii, $C_2^{\beta=1}$ has a background rejection that is comparable to or better than the groomed masses.

By comparing Figures 15(a), 16(a) and 17(b), we can see how the background rejection performance evolves as we increase momenta whilst keeping the jet radius fixed to $R=0.8$. Similarly, by comparing Figures 15(b), 16(b) and 17(c) we can see how performance evolves with p_T for $R=1.2$. For both $R=0.8$ and $R=1.2$ the background rejection power of the groomed masses increases with increasing p_T , with a factor 1.5-2.5 increase in rejection in going from the 300-400 GeV to 1.0-1.1 TeV bins. In Figure 18 we show the Soft-drop $\beta = 2$ groomed mass and the pruned mass for signal and background in the p_T 300-400 and p_T 1.0-1.1 TeV bins for $R=1.2$ jets. Two effects result in the improved performance of the groomed mass at high p_T . Firstly, as is evident from the figure, the resolution of the signal peak after grooming improves, because the groomer finds it easier to pick out the hard signal component of the jet against the softer components of the underlying event when the signal is boosted. Secondly, one can see from Figure 9 that as p_T increases the perturbative shoulder of the gluon distribution decreases in size, as discussed in Section 5.4, and thus there is a slight decrease (or at least no increase) in the level of background in the signal mass region ($m/p_T/R \sim 0.5$).

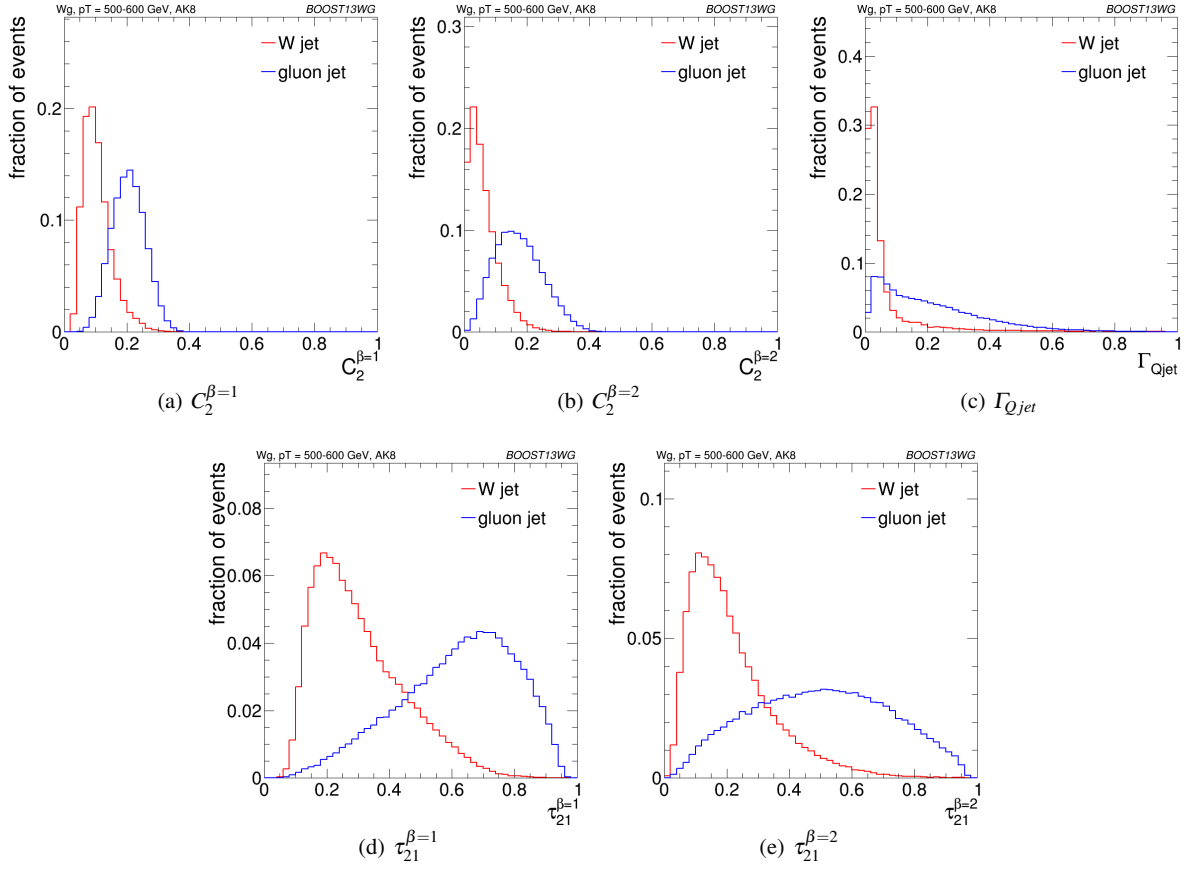


Fig. 11 Comparisons of the QCD background to the WW signal in the p_T 500-600 GeV bin using the anti- k_T R=0.8 algorithm: substructure variables.

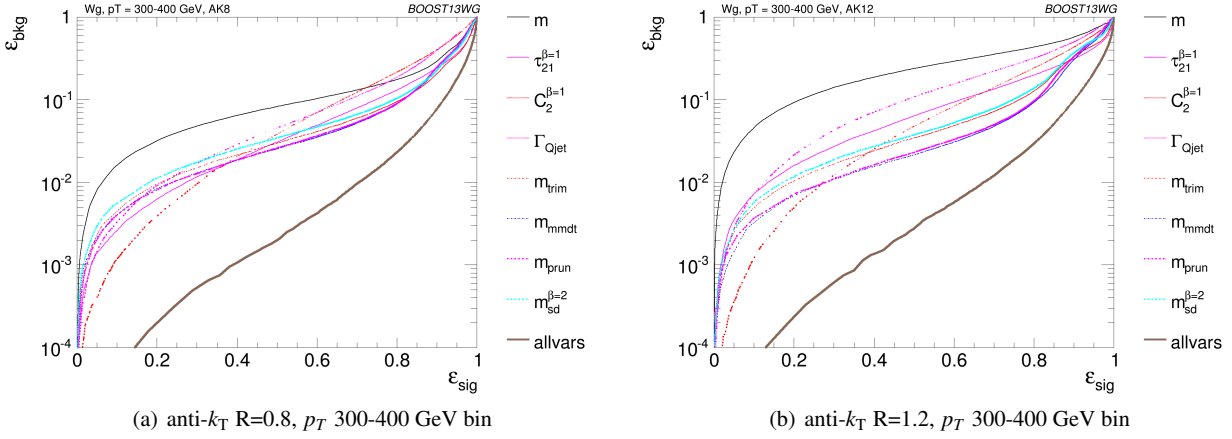


Fig. 12 The ROC curve for all single variables considered for W tagging in the p_T 300-400 GeV bin using the anti- k_T R=0.8 algorithm and R=1.2 algorithm.

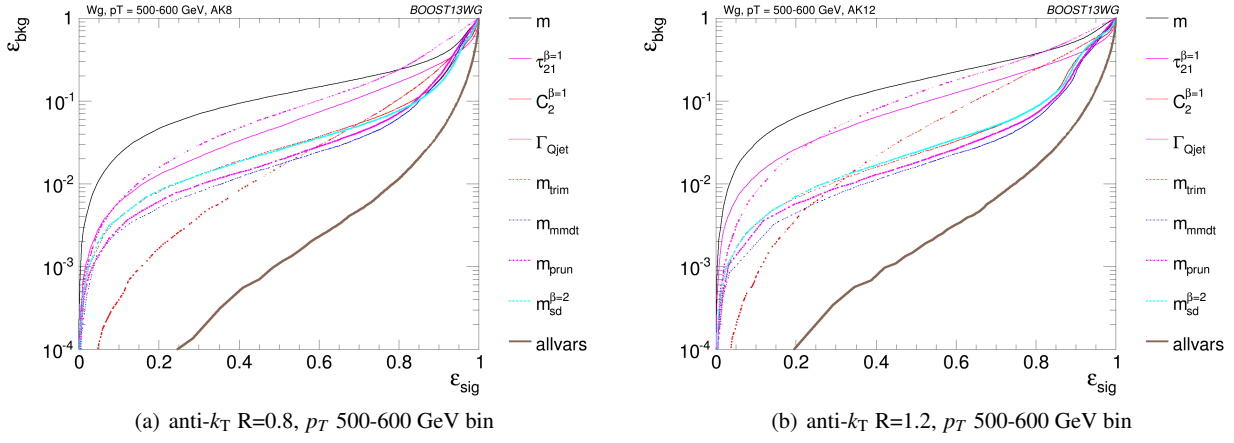


Fig. 13 The ROC curve for all single variables considered for W tagging in the p_T 500-600 GeV bin using the anti- k_T $R=0.8$ algorithm and $R=1.2$ algorithm.

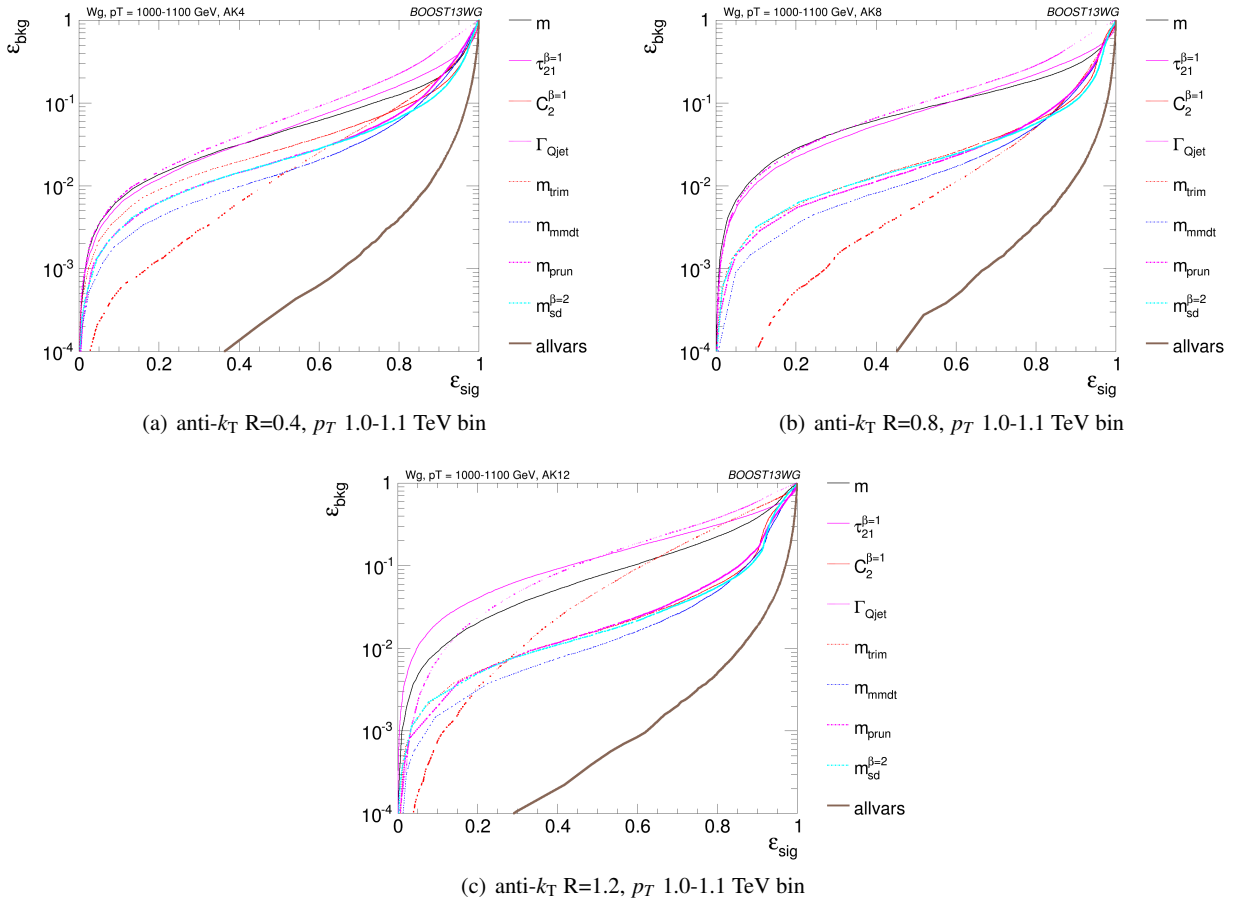


Fig. 14 The ROC curve for all single variables considered for W tagging in the p_T 1.0-1.1 TeV bin using the anti- k_T $R=0.4$ algorithm, anti- k_T $R=0.8$ algorithm and $R=1.2$ algorithm.

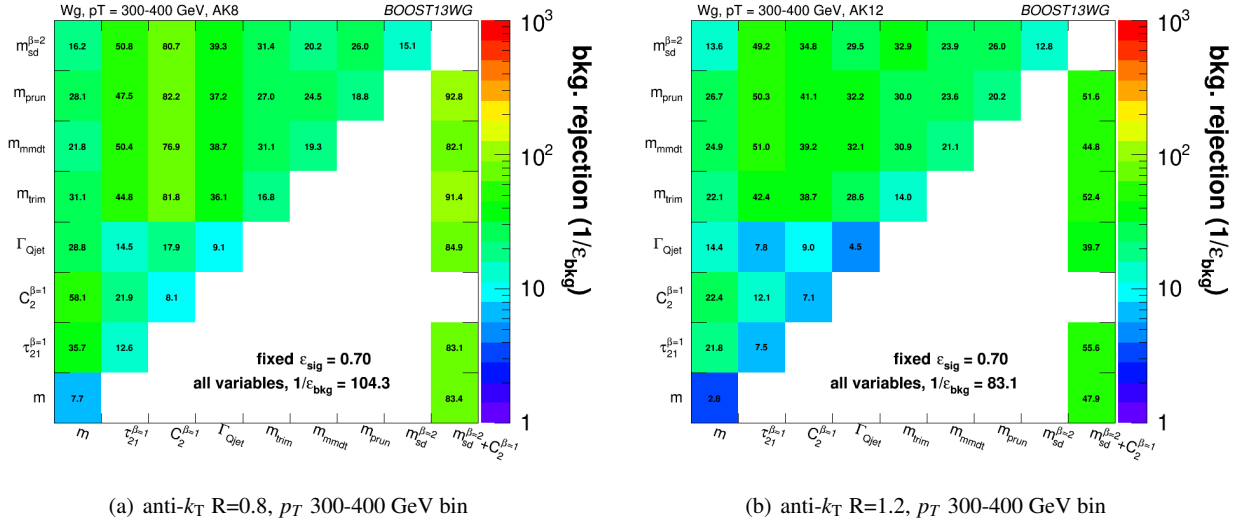


Fig. 15 The background rejection for a fixed signal efficiency (70%) of each BDT combination of each pair of variables considered, in the p_T 300-400 GeV bin using the anti- k_T $R=0.8$ algorithm and $R=1.2$ algorithm. Also shown is the background rejection for a BDT combination of all of the variables considered.

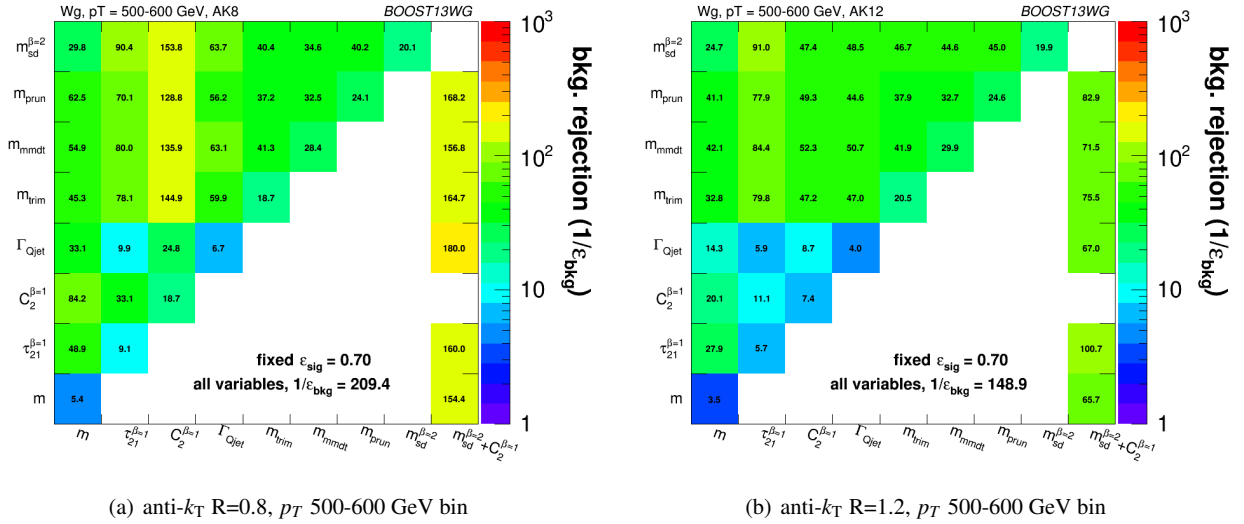


Fig. 16 The background rejection for a fixed signal efficiency (70%) of each BDT combination of each pair of variables considered, in the p_T 500-600 GeV bin using the anti- k_T $R=0.8$ algorithm and $R=1.2$ algorithm. Also shown is the background rejection for a BDT combination of all of the variables considered.

843 However, one can see from the Figures 15(b), 16(b) and 17(c)ing from the lower to the higher p_T bin, the signal peak re-
 844 mains fairly unchanged, whereas the background peak shifts
 845 somewhat differently. The background rejection power of
 846 the Γ_{Qjet} and $\tau_{21}^{\beta=1}$ variables both decrease with increasing
 847 p_T , by up to a factor two in going from the 300-400 GeV
 848 to 1.0-1.1 TeV bins. Conversely the rejection power of $C_2^{\beta=1}$
 849 dramatically increases with increasing p_T for $R=0.8$, but
 850 does not improve with p_T for the larger jet radius $R=1.2$.
 851 In Figure 19 we show the $\tau_{21}^{\beta=1}$ and $C_2^{\beta=1}$ distributions for
 852 signal and background in the p_T 300-400 and p_T 1.0-1.1
 853 TeV bins for $R=0.8$ jets. For $\tau_{21}^{\beta=1}$ one can see that in mov-
 854
 855
 856
 857
 858
 859
 860
 861
 862
 863
 864
 865
 866
 867
 868
 869
 870
 871
 872
 873
 874
 875
 876
 877
 878
 879
 880
 881
 882
 883
 884
 885
 886
 887
 888
 889
 890
 891
 892
 893
 894
 895
 896
 897
 898
 899
 900

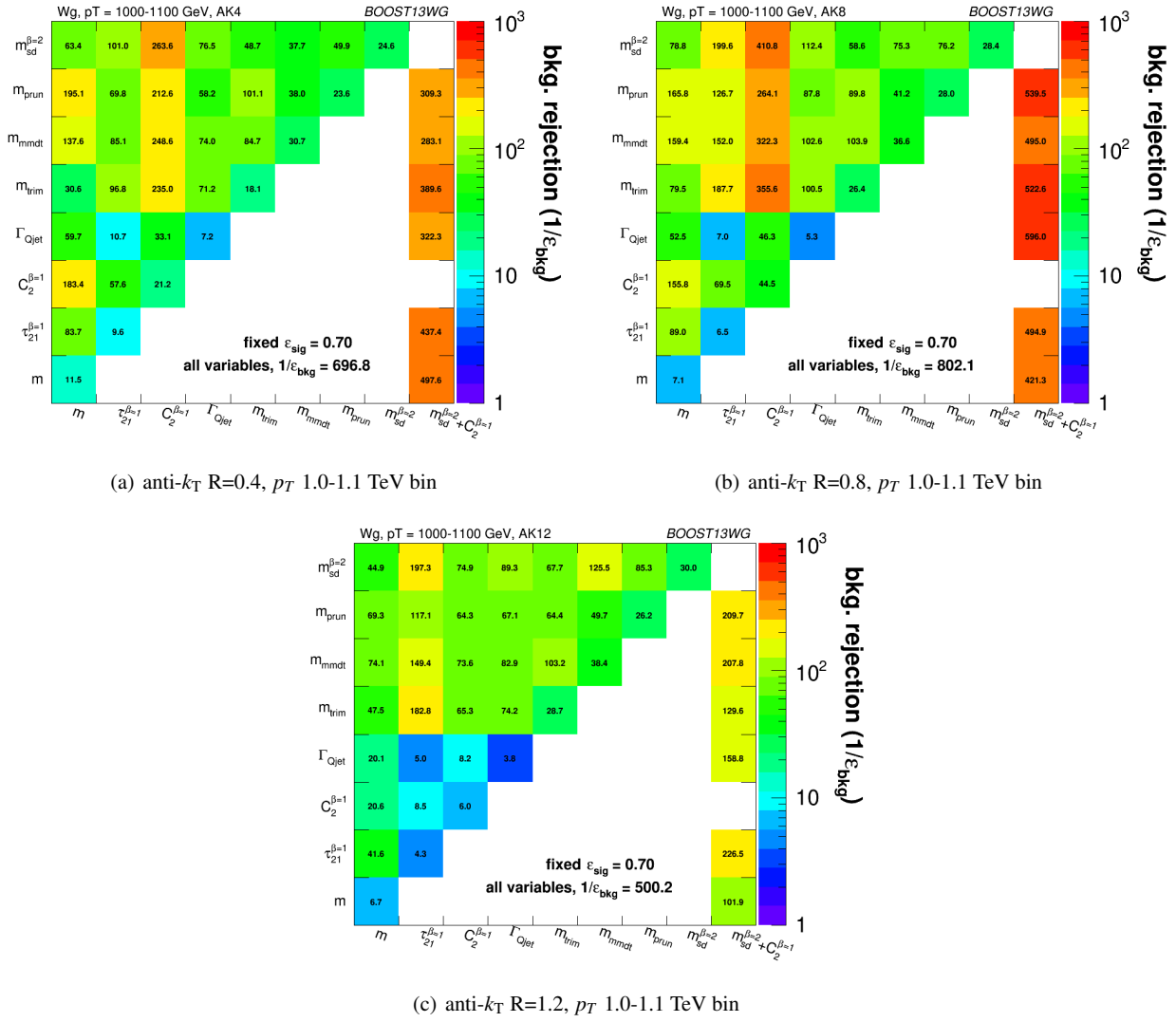


Fig. 17 The background rejection for a fixed signal efficiency (70%) of each BDT combination of each pair of variables considered, in the p_T 1.0-1.1 TeV bin using the anti- k_T $R=0.4$, $R=0.8$ and $R=1.2$ algorithm. Also shown is the background rejection for a BDT combination of all of the variables considered.

865 By comparing the individual sub-figures of Figures 15, 16
 866 and 17 we can see how the background rejection perfor-
 867 mance depends on jet radius within the same p_T bin. To
 868 within $\sim 25\%$, the background rejection power of the groomed
 869 masses remains constant with respect to the jet radius. Fig-
 870 ure 20 shows how the groomed mass changes for varying
 871 jet radius in the p_T 1.0-1.1 TeV bin. One can see that the
 872 signal mass peak remains unaffected by the increased radi-
 873 us, as expected, since grooming removes the soft contam-
 874 ination which could otherwise increase the mass of the jet
 875 as the radius increased. The gluon background in the sig-
 876 nal mass region also remains largely unaffected, as expected
 877 from Figure 9, which shows very little dependence of the
 878 groomed gluon mass distribution on R in the signal region
 879 ($m/p_T/R \sim 0.5$). This is discussed further in Section 5.4.

880 However, we again see rather different behaviour versus
 881 R for the substructure variables. In all p_T bins considered the
 882 most performant substructure variable, $C_2^{\beta=1}$, performs best
 883 for an anti- k_T distance parameter of $R=0.8$. The performance
 884 of this variable is dramatically worse for the larger jet radius
 885 of $R=1.2$ (a factor seven worse background rejection in the
 886 1.0-1.1 TeV bin), and substantially worse for $R=0.4$. For the
 887 other jet substructure variables considered, Γ_{Qjet} and $\tau_{21}^{\beta=1}$,
 888 their background rejection power also reduces for larger jet
 889 radius, but not to the same extent. Figure 21 shows the $\tau_{21}^{\beta=1}$
 890 and $C_2^{\beta=1}$ distributions for signal and background in the 1.0-
 891 1.1 TeV p_T bin for $R=0.8$ and $R=1.2$ jet radii. One can
 892 clearly see that for the larger jet radius the $C_2^{\beta=1}$ distribu-
 893 tion of both signal and background get wider, and conse-
 894 quently the discrimination power decreases. For $\tau_{21}^{\beta=1}$ there

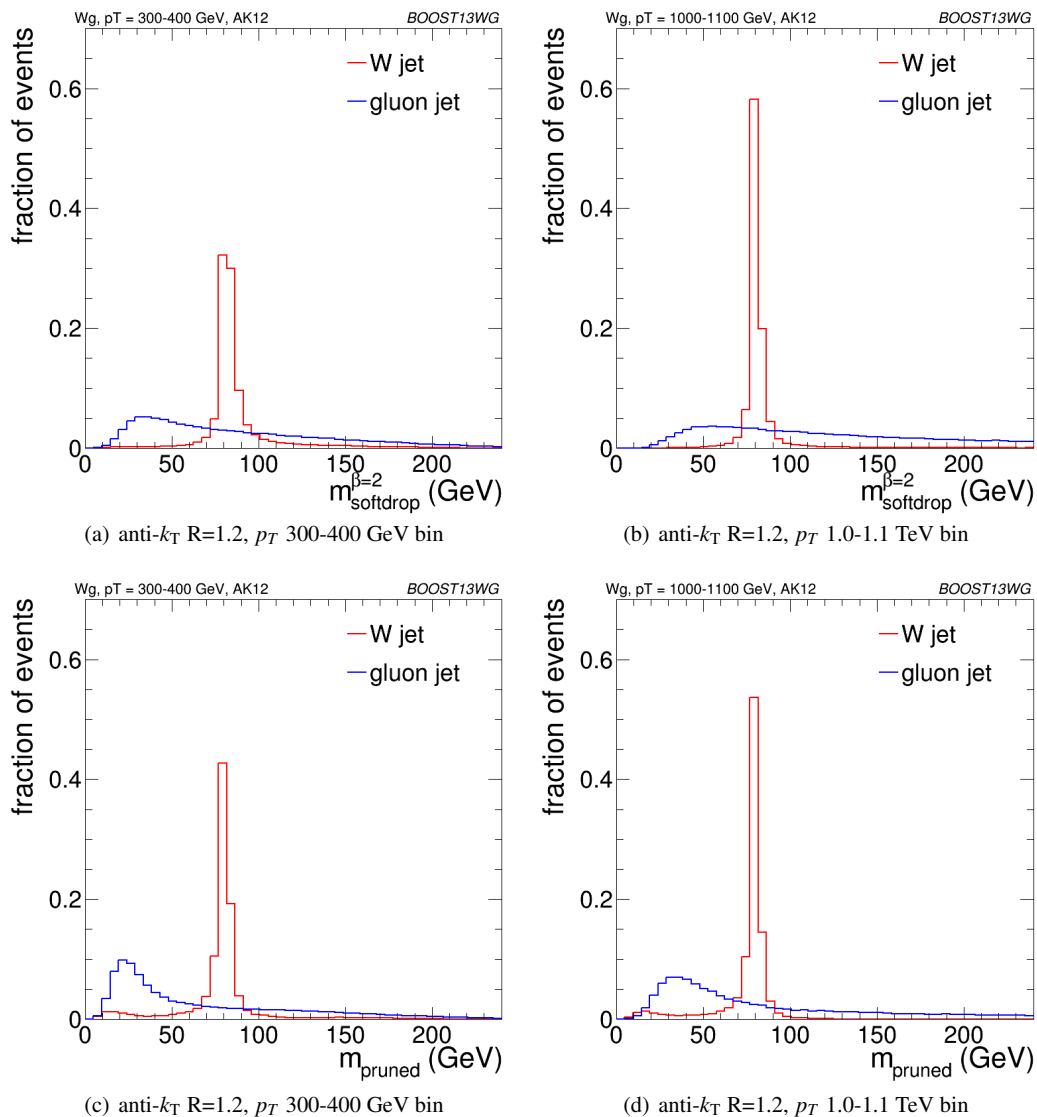


Fig. 18 The Soft-drop $\beta = 2$ and pruned groomed mass distribution for signal and background $R=1.2$ jets in two different p_T bins.

895 is comparatively little change in the distributions with in-907
 896 creasing jet radius. The increased sensitivity of C_2 to soft
 897 wide angle radiation in comparison to τ_{21} is a known feature
 898 of this variable [42], and a useful feature in discriminating 908
 899 coloured versus colour singlet jets. However, at very large 909
 900 jet radii ($R \sim 1.2$), this feature becomes disadvantageous; the 910
 901 jet can pick up a significant amount of initial state or other 911
 902 uncorrelated radiation, and C_2 is more sensitive to this than 912
 903 is τ_{21} . This uncorrelated radiation has no (or very little) 913
 904 dependence on whether the jet is W- or gluon-initiated, and 914
 905 so sensitivity to this radiation means that the discrimination 915
 906 power will decrease.

6.3 Combined Performance

The off-diagonal entries in Figures 15, 16 and 17 can be used to compare the performance of different BDT two-variable combinations, and see how this varies as a function of p_T and R . By comparing the background rejection achieved for the two-variable combinations to the background rejection of the “all variables” BDT, one can understand how much more discrimination is possible by adding further variables to the two-variable BDTs.

916 One can see that in general the most powerful two-variable
 917 combinations involve a groomed mass and a non-mass sub-
 918 structure variable ($C_2^{\beta=1}$, Γ_{Qjet} or $\tau_{21}^{\beta=1}$). Two-variable com-
 919 binations of the substructure variables are not powerful in
 920 comparison. Which particular mass + substructure variable

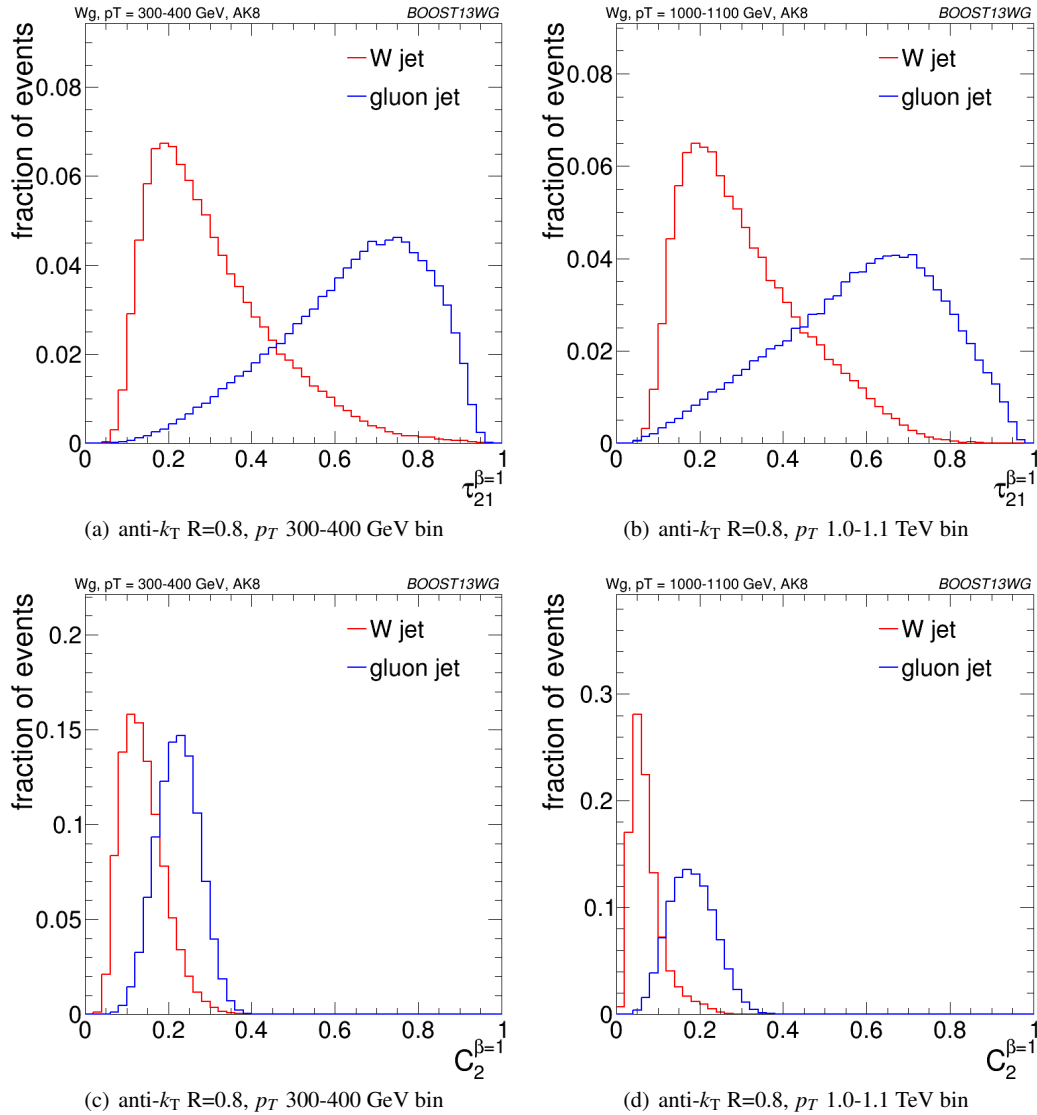


Fig. 19 The $\tau_{21}^{\beta=1}$ and $C_2^{\beta=1}$ distributions for signal and background $R=0.8$ jets in two different p_T bins.

921 combination is the most powerful depends strongly on the p_T and R of the jet, as discussed in the sections that follow. 938

923 There is also modest improvement in the background rejection when different groomed masses are combined, compared to the single variable groomed mass performance, indicating that there is complementary information between the different groomed masses. In addition, there is an improvement in the background rejection when the groomed masses are combined with the ungroomed mass, indicating that grooming removes some useful discriminatory information from the jet. These observations are explored further in the section below. 946

933 Generally one can see that the $R=0.8$ jets offer the best two-variable combined performance in all p_T bins explored here. This is despite the fact that in the highest $1.0-1.1$ GeV p_T bin the average separation of the quarks from the

decay is much smaller than 0.8 , and well within 0.4 . This conclusion could of course be susceptible to pile-up, which is not considered in this study.

6.3.1 Mass + Substructure Performance

As already noted, the largest background rejection at 70% signal efficiency are in general achieved using those two variable BDT combinations which involve a groomed mass and a non-mass substructure variable. For both $R=0.8$ and $R=1.2$ jets, the rejection power of these two variable combinations increases substantially with increasing p_T , at least within the p_T range considered here.

For a jet radius of $R=0.8$, across the full p_T range considered, the groomed mass + substructure variable combinations with the largest background rejection are those which

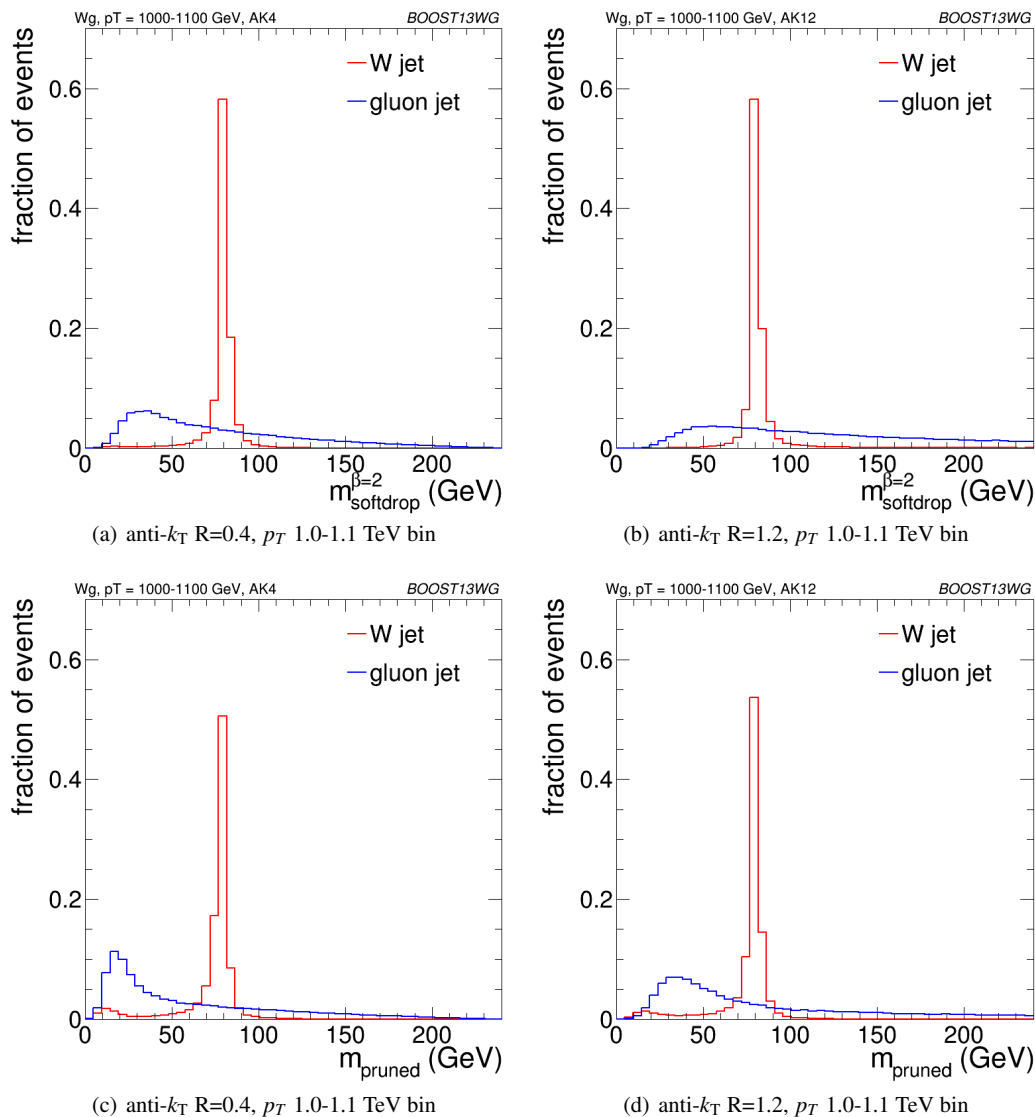


Fig. 20 The Soft-drop $\beta = 2$ and pruned groomed mass distribution for signal and background $R=0.4$ and $R=1.2$ jets in the 1.0-1.1 TeV p_T bin.

951 involve $C_2^{\beta=1}$. For example, in combination with $m_{sd}^{\beta=2}$, this 966
 952 produces a five-, eight- and fifteen-fold increase in back- 967
 953 ground rejection compared to using the groomed mass alone. 968
 954 In Figure 22 the low degree of correlation between $m_{sd}^{\beta=2}$ 969
 955 versus $C_2^{\beta=1}$ that leads to these large improvements in back- 970
 956 ground rejection can be seen. One can also see that what 971
 957 little correlation exists is rather non-linear in nature, chang- 972
 958 ing from a negative to a positive correlation as a function of 973
 959 the groomed mass, something which helps to improve the 974
 960 background rejection in the region of the W mass peak. 975

961 However, when we switch to a jet radius of $R=1.2$ the 976
 962 picture for $C_2^{\beta=1}$ combinations changes dramatically. These 977
 963 become significantly less powerful, and the most powerful 978
 964 variable in groomed mass combinations becomes $\tau_{21}^{\beta=1}$ for 979
 965 all jet p_T considered. Figure 23 shows the correlation be-

tween $m_{sd}^{\beta=2}$ and $C_2^{\beta=1}$ in the p_T 1.0 - 1.2 TeV bin for the
 various jet radii considered. Figure 24 is the equivalent set of
 distributions for $m_{sd}^{\beta=2}$ and $\tau_{21}^{\beta=1}$. One can see from Figure 23
 that, due to the sensitivity of the observable to soft, wide-
 angle radiation, as the jet radius increases $C_2^{\beta=1}$ increases
 and becomes more and more smeared out for both signal and
 background, leading to worse discrimination power. This
 does not happen to the same extent for $\tau_{21}^{\beta=1}$. We can see
 from Figure 24 that the negative correlation between $m_{sd}^{\beta=2}$
 and $\tau_{21}^{\beta=1}$ that is clearly visible for $R=0.4$ decreases for larger
 jet radius, such that the groomed mass and substructure vari-
 able are far less correlated and $\tau_{21}^{\beta=1}$ offers improved dis-
 crimination within a $m_{sd}^{\beta=2}$ mass window.

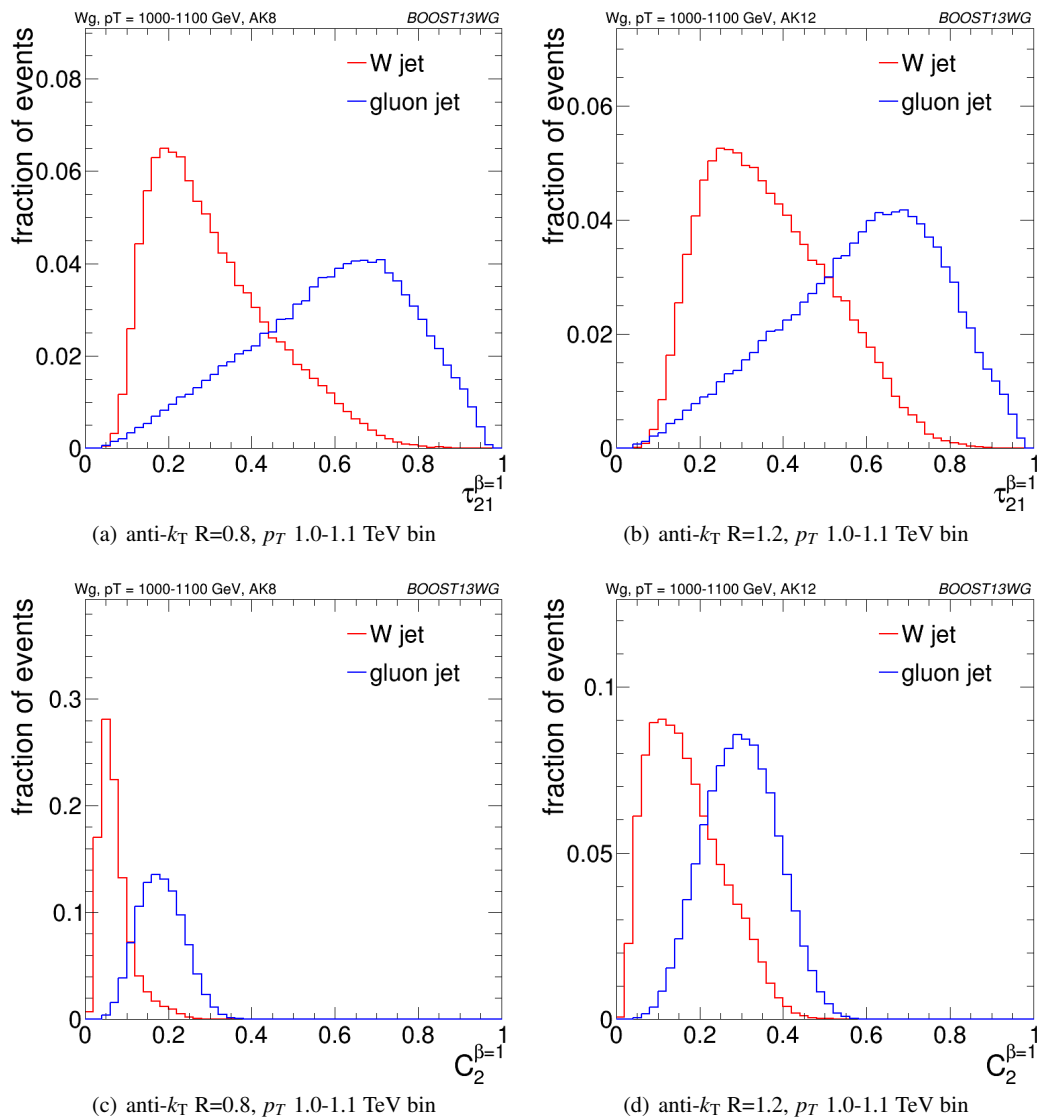


Fig. 21 The $\tau_{21}^{\beta=1}$ and $C_2^{\beta=1}$ distributions for signal and background $R=0.8$ and $R=1.2$ jets in the 1.0-1.1 TeV p_T bin.

6.3.2 Mass + Mass Performance

The different groomed masses and the ungroomed mass are of course not fully correlated, and thus one can always see some kind of improvement in the background rejection (relative to the single mass performance) when two different mass variables are combined in the BDT. However, in some cases the improvement can be dramatic, particularly at higher p_T , and particularly for combinations with the ungroomed mass. For example, in Figure 17 we can see that in the 1.0-1.1 TeV bin the combination of pruned mass with ungroomed mass produces a greater than eight-fold improvement in the background rejection for $R=0.4$ jets, a greater than five-fold improvement for $R=0.8$ jets, and a factor \sim two improvement for $R=1.2$ jets. A similar behaviour can be seen for mMDT mass. In Figures 25, 26 and 27 is shown the 2-D

correlation plots of the pruned mass versus the ungroomed mass separately for the WW signal and gg background samples in the p_T 1.0-1.1 TeV bin, for the various jet radii considered. For comparison, the correlation of the trimmed mass with the ungroomed mass, a combination that does not improve on the single mass as dramatically, is shown. In all cases one can see that there is a much smaller degree of correlation between the pruned mass and the ungroomed mass in the backgrounds sample than for the trimmed mass and the ungroomed mass. This is most obvious in Figure 25, where the high degree of correlation between the trimmed and ungroomed mass is expected, since with the parameters used (in particular $R_{trim} = 0.2$) we cannot expect trimming to have a significant impact on an $R=0.4$ jet. The reduced correlation with ungroomed mass for pruning in the background means that, once we have made the requirement that

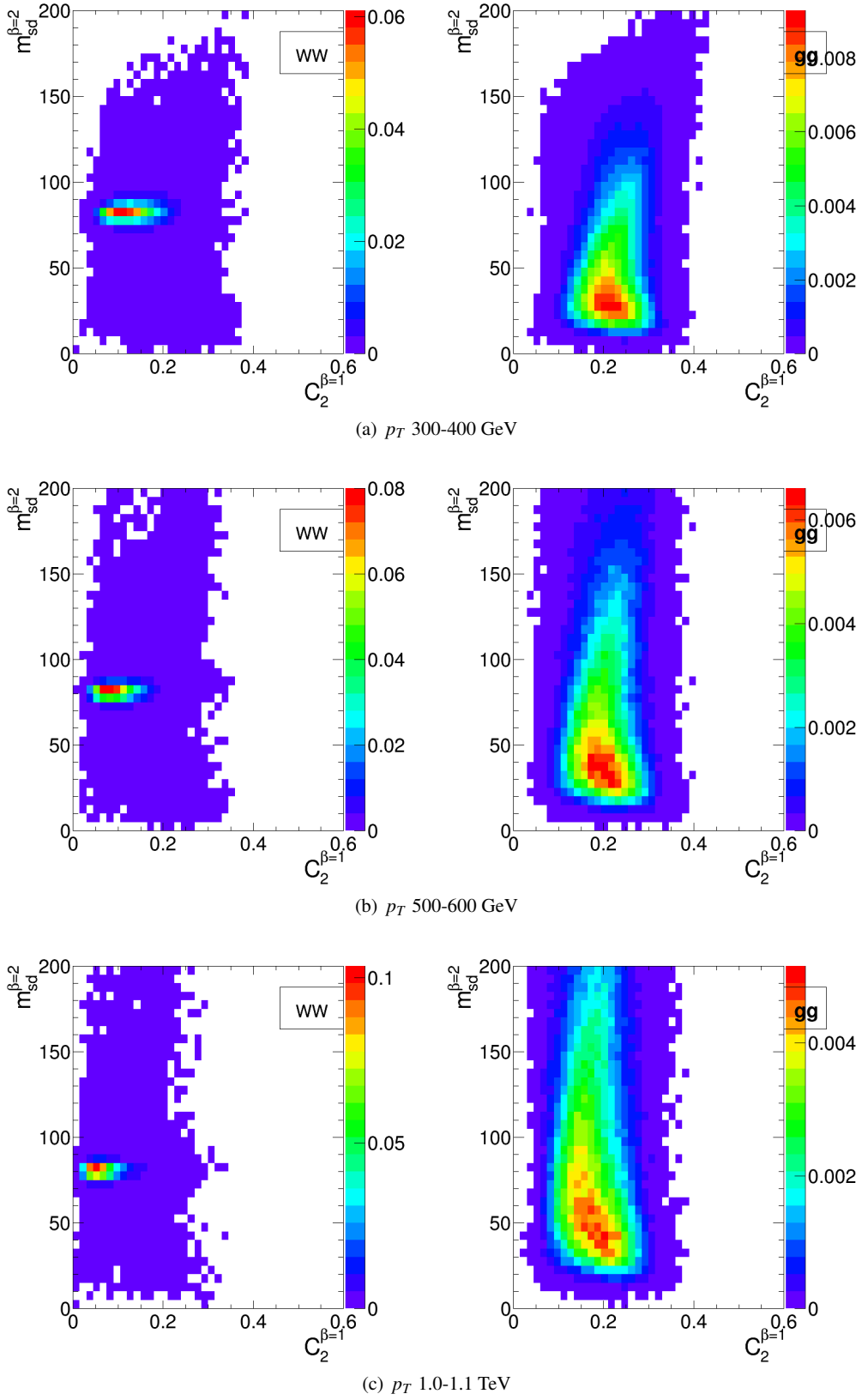


Fig. 22 2-D plots showing $m_{sd}^{\beta=2}$ versus $C_2^{\beta=1}$ for $R=0.8$ jets in the various p_T bins considered.

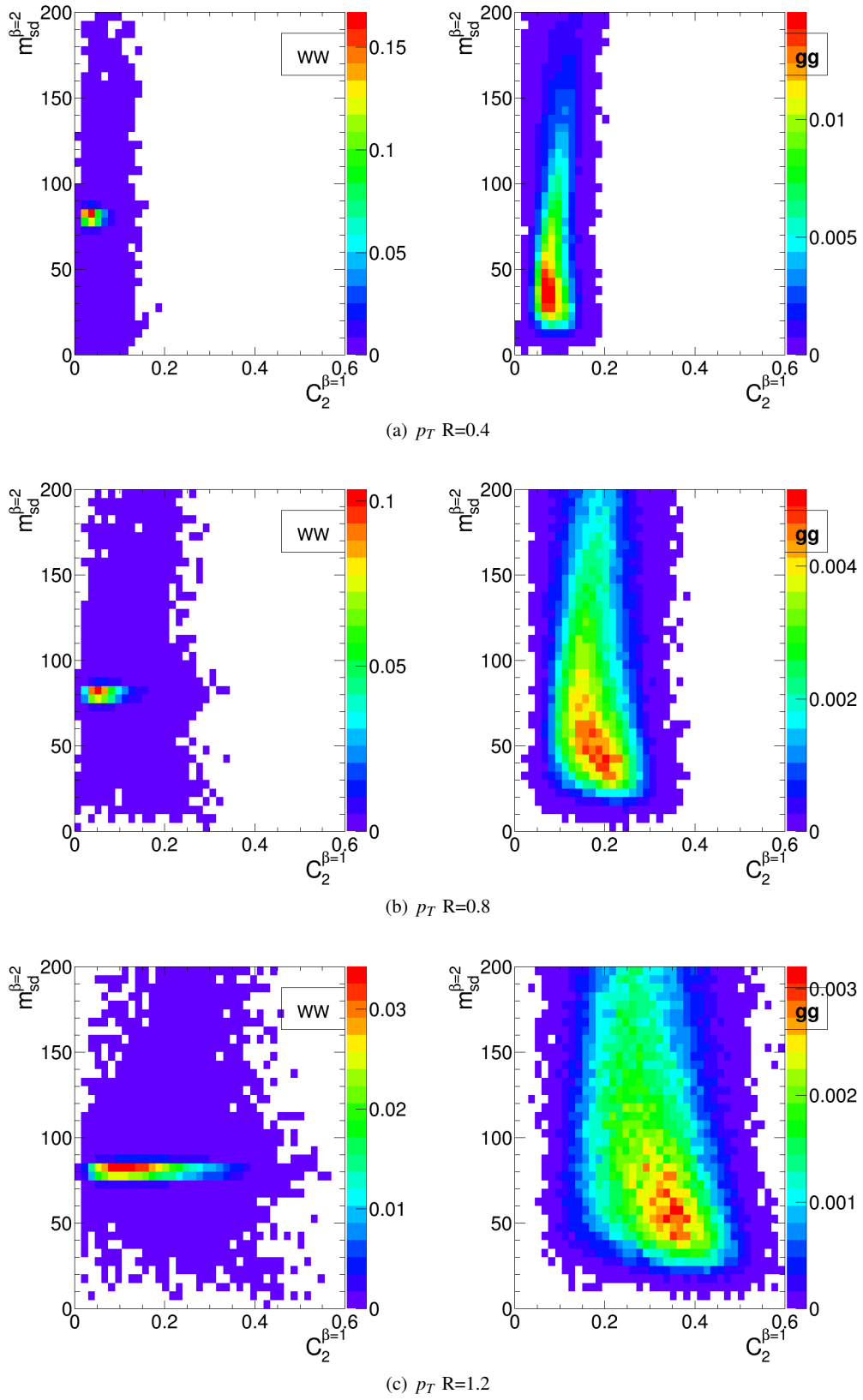


Fig. 23 2-D plots showing $m_{sd}^{\beta=2}$ versus $C_2^{\beta=1}$ for $R=0.4, 0.8$ and 1.2 jets in the p_T 1.0-1.1 TeV bin.

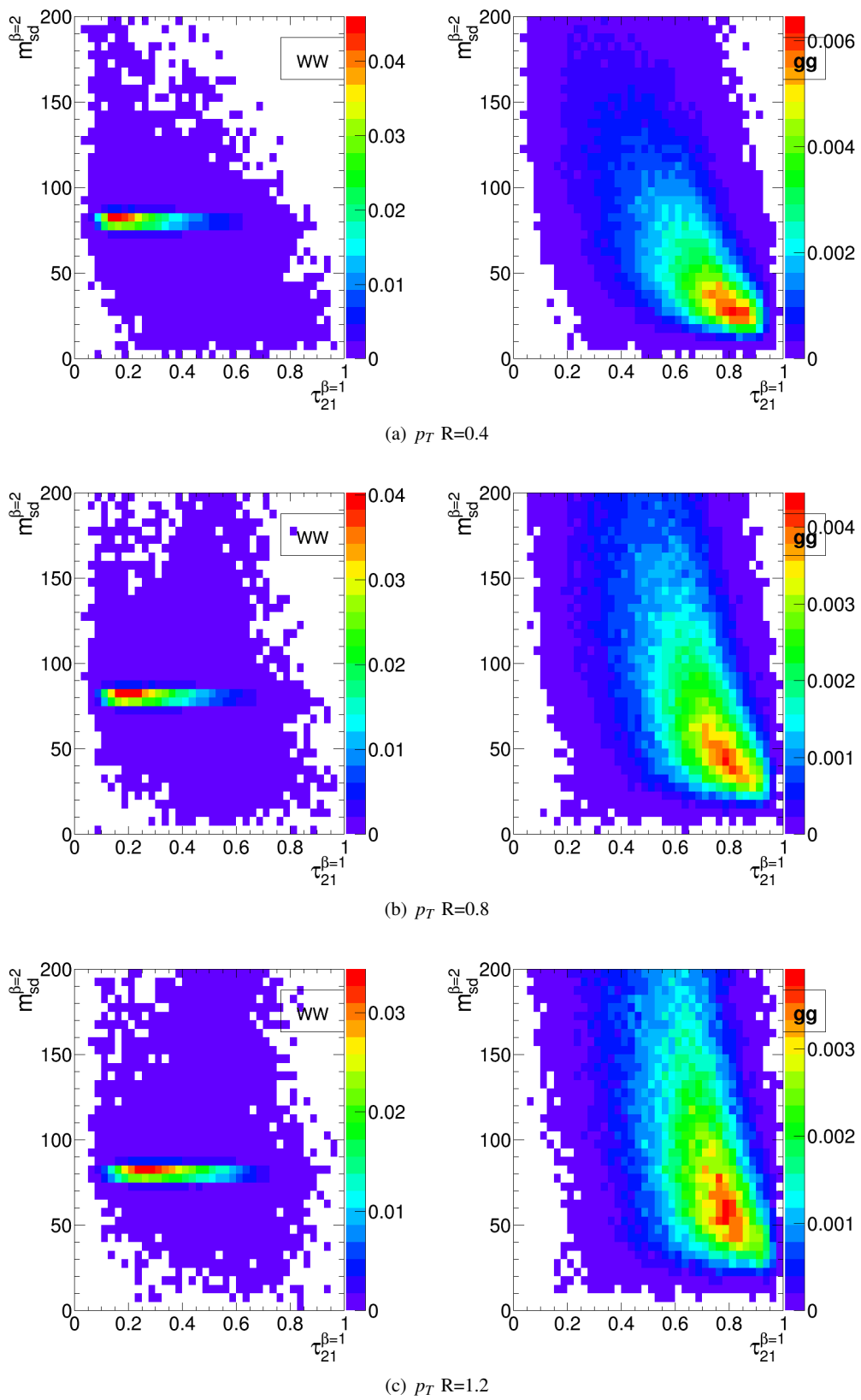


Fig. 24 2-D plots showing $m_{sd}^{\beta=2}$ versus $\tau_{21}^{\beta=1}$ for $R=0.4, 0.8$ and 1.2 jets in the p_T 1.0-1.1 TeV bin.

the pruned mass is consistent with a W (i.e. ~ 80 GeV), relatively large difference between signal and background in the ungroomed mass still remains, and can be exploited to improve the background rejection further. In other words, many of the background events which pass the pruned mass requirement do so because they are shifted to lower mass (to be within a signal mass window) by the grooming, but these events still have the property that they look very much like background events before the grooming. A single requirement on the groomed mass only does not exploit this. Of course, the impact of pile-up, not considered in this study, could significantly limit the degree to which the ungroomed mass could be used to improve discrimination in this way.

6.3.3 “All Variables” Performance

As well as the background rejection at a fixed 70% signal efficiency for two-variable combinations, Figures 15, 16 and 17 also report the background rejection achieved by a combination of all the variables considered into a single BDT discriminant. One can see that, in all cases, the rejection power of this “all variables” BDT is significantly larger than the best two-variable combination. This indicates that beyond the best two-variable combination there is still significant complementary information available in the remaining variables in order to improve the discrimination of signal and background. How much complementary information is available appears to be p_T dependent. In the lower p_T 300-400 and 500-600 GeV bins the background rejection of the “all variables” combination is a factor ~ 1.5 greater than the best two-variable combination, but in the highest p_T bin it is a factor ~ 2.5 greater.

The final column in Figures 15, 16 and 17 allows us to explore the all variables performance a little further. It shows the background rejection for three variable BDT combinations of $m_{sd}^{\beta=2} + C_2^{\beta=1} + X$, where X is the variable on the y-axis. For jets with $R=0.4$ and $R=0.8$, the combination $m_{sd}^{\beta=2} + C_2^{\beta=1}$ is the best performant (or very close to the best performant) two-variable combination in every p_T bin considered. For $R=1.2$ this is not the case, as $C_2^{\beta=1}$ is superseded by $\tau_{21}^{\beta=1}$ in performance, as discussed earlier. Thus, in considering the three-variable combination results it is best to focus on the $R=0.4$ and $R=0.8$ cases. Here we see that, for the lower p_T 300-400 and 500-600 GeV bins, adding the third variable to the best two-variable combination brings us to within $\sim 15\%$ of the “all variables” background rejection. However, in the highest p_T 1.0-1.1 TeV bin, whilst adding the third variable does improve the performance considerably, we are still $\sim 40\%$ from the observed “all variables” background rejection, and clearly adding a fourth or maybe even fifth variable would bring considerable gains. In terms of which variable offers the best improvement when added to the $m_{sd}^{\beta=2} + C_2^{\beta=1}$ combination, it is hard to see an obvious

pattern; the best third variable changes depending on the p_T and R considered.

In conclusion, it appears that there is a rich and complex structure in terms of the degree to which the discriminatory information provided by the set of variables considered overlaps, with the degree of overlap apparently decreasing at higher p_T . This suggests that in all p_T ranges, but especially at higher p_T , there are substantial performance gains to be made by designing a more complex multivariate W tagger.

6.4 Conclusions

We have studied the performance, in terms of the degree to which a hadronically decaying W boson can be separated from a gluonic background, of a number of groomed jet masses, substructure variables, and BDT combinations of the above. We have used this to build a picture of how the discriminatory information contained in the variables overlaps, and how this complementarity between the variables changes with p_T and anti- k_T distance parameter R .

In terms of the performance of individual variables, we find that, in agreement with other studies [56], in general the groomed masses perform best, with a background rejection power that increases with increasing p_T , but which is more constant with respect to changes in R . We have explained the dependence of the groomed mass performance on p_T and R using the understanding of the QCD mass distribution gleaned in Section 5.4. Conversely, the performance of other substructure variables, such as $C_2^{\beta=1}$ and $\tau_{21}^{\beta=1}$ is more susceptible to changes in radius, with background rejection power decreasing with increasing R . This is due to the inherent sensitivity of these observables to soft, wide angle radiation.

The best two-variable performance is obtained by combining a groomed mass with a substructure variable. Which particular substructure variable works best in combination is strongly dependent on p_T and R . $C_2^{\beta=1}$ offers significant complementarity to groomed mass at smaller R , owing to the small degree of correlation between the variables. However, the sensitivity of $C_2^{\beta=1}$ to soft, wide-angle radiation leads to worse discrimination power at large R , where $\tau_{21}^{\beta=1}$ performs better in combination. Our studies also demonstrate the potential for enhanced discrimination by combining groomed and ungroomed mass information, although the use of ungroomed mass in this may in practice be limited by the presence of pile-up that is not considered in these studies.

By examining the performance of a BDT combination of all the variables considered, it is clear that there are potentially substantial performance gains to be made by designing a more complex multivariate W tagger, especially at higher p_T .

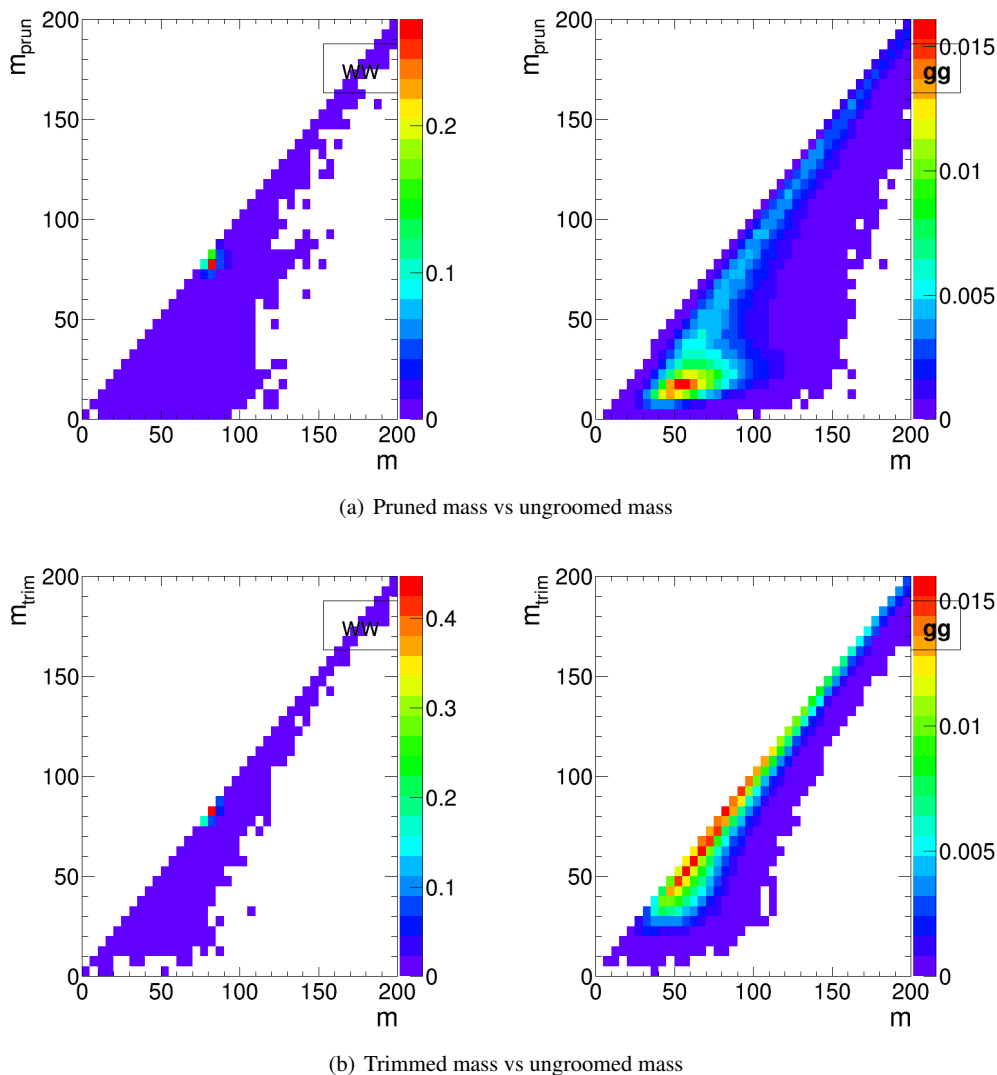


Fig. 25 2-D plots showing the correlation between groomed and ungroomed mass for WW and gg events in the p_T 1.0-1.1 TeV bin using the anti- k_T $R=0.4$ algorithm.

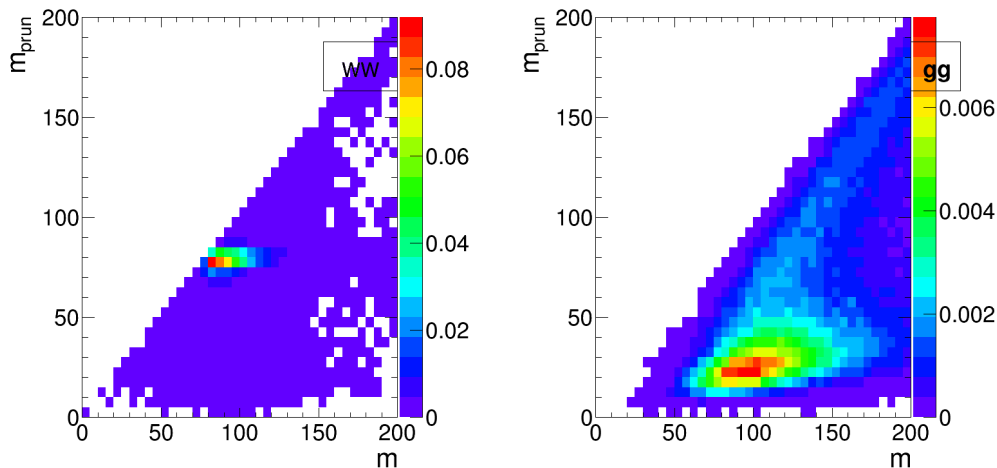
7 Top Tagging

In this section, we study the identification of boosted top quarks at Run II of the LHC. Boosted top quarks result in large-radius jets with complex substructure, containing a b subjet and a boosted W . The additional kinematic handles coming from the reconstruction of the W mass and b -tagging allow a very high degree of discrimination of top quark jets from QCD backgrounds. We study fully hadronic decays of the top quark.

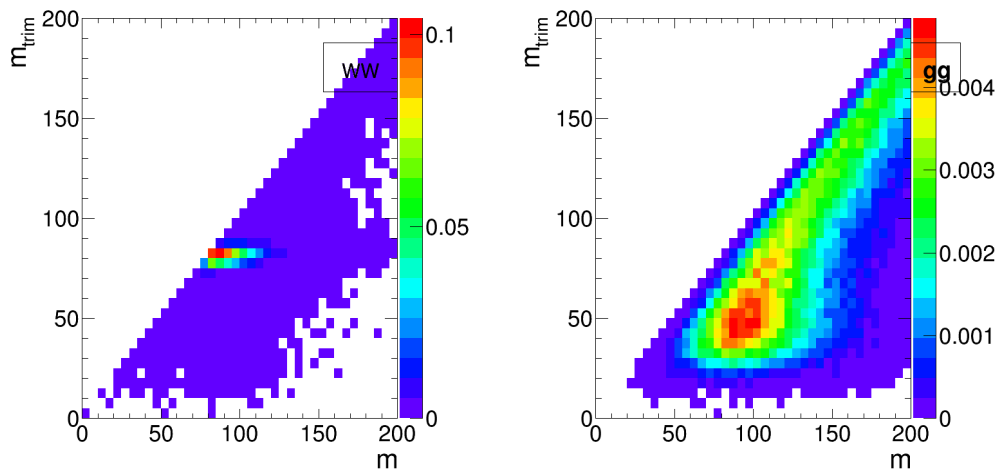
We consider top quarks with moderate boost (600-1000 GeV), and perhaps most interestingly, at high boost ($\gtrsim 1500$ GeV). Top tagging faces several challenges in the high- p_T regime. For such high- p_T jets, the b -tagging efficiencies are no longer reliably known. Also, the top jet can also be accompanied by additional radiation with $p_T \sim m_t$, leading to com-

binatoric ambiguities of reconstructing the top and W , and the possibility that existing taggers or observables shape the background by looking for subjet combinations that reconstruct m_t/m_W . To study this, we examine the performance of both mass-reconstruction variables, as well as shape observables that probe the three-pronged nature of the top jet and the accompanying radiation pattern.

We use the top quark MC samples for each bin described in Section 2.2. The analysis relies on FASTJET 3.0.3 for jet clustering and calculation of jet substructure observables. Jets are clustered using the anti- k_t algorithm. An upper and lower p_T cut are applied after jet clustering to each sample to ensure similar p_T spectra in each bin. The bins in leading jet p_T that are investigated for top tagging are 600-700 GeV, 1-1.1 TeV, and 1.5-1.6 TeV. Jets are clustered with radii $R = 0.4, 0.8, \text{ and } 1.2$; $R = 0.4$ jets are only studied in the 1.5-



(a) Pruned mass vs ungroomed mass



(b) Trimmed mass vs ungroomed mass

Fig. 26 2-D plots showing the correlation between groomed and ungroomed mass for WW and gg events in the p_T 1.0-1.1 TeV bin using the anti- k_T $R=0.8$ algorithm.

1141 1.6 TeV bin because for top quarks with this boost, the top
1142 decay products are all contained within an $R = 0.4$ jet.

1143 7.1 Methodology

1144 We study a number of top-tagging strategies, in particular:

- 1145 1. HEPTopTagger
- 1146 2. Johns Hopkins Tagger (JH)
- 1147 3. Trimming
- 1148 4. Pruning

1149 The top taggers have criteria for reconstructing a top and
1150 W candidate, and a corresponding top and W mass, as de-
1151 scribed in Section 3.3, while the grooming algorithms (trim-
1152 ming and pruning) do not incorporate a W -identification step.

1153 For a level playing field, where grooming is used we con-
1154 struct a W candidate mass, m_W , from the three leading sub-
1155 jets by taking the mass of the pair of subjets with the smallest
1156 invariant mass; in the case that only two subjets are recon-
1157 structed, we take the mass of the leading subjet. The top
1158 mass, m_t , is the mass of the groomed jet. All of the above
1159 taggers and groomers incorporate a step to remove pile-up
1160 and other soft radiation.

1161 We also consider the performance of the following jet
1162 shape observables:

- 1163 – The ungroomed jet mass.
- 1164 – N -subjettiness ratios τ_2/τ_1 and τ_3/τ_2 with $\beta = 1$ and the
1165 “winner-takes-all” axes.
- 1166 – 2-point energy correlation function ratios $C_2^{\beta=1}$ and $C_3^{\beta=1}$.
- 1167 – The pruned Qjet mass volatility, Γ_{Qjet} .

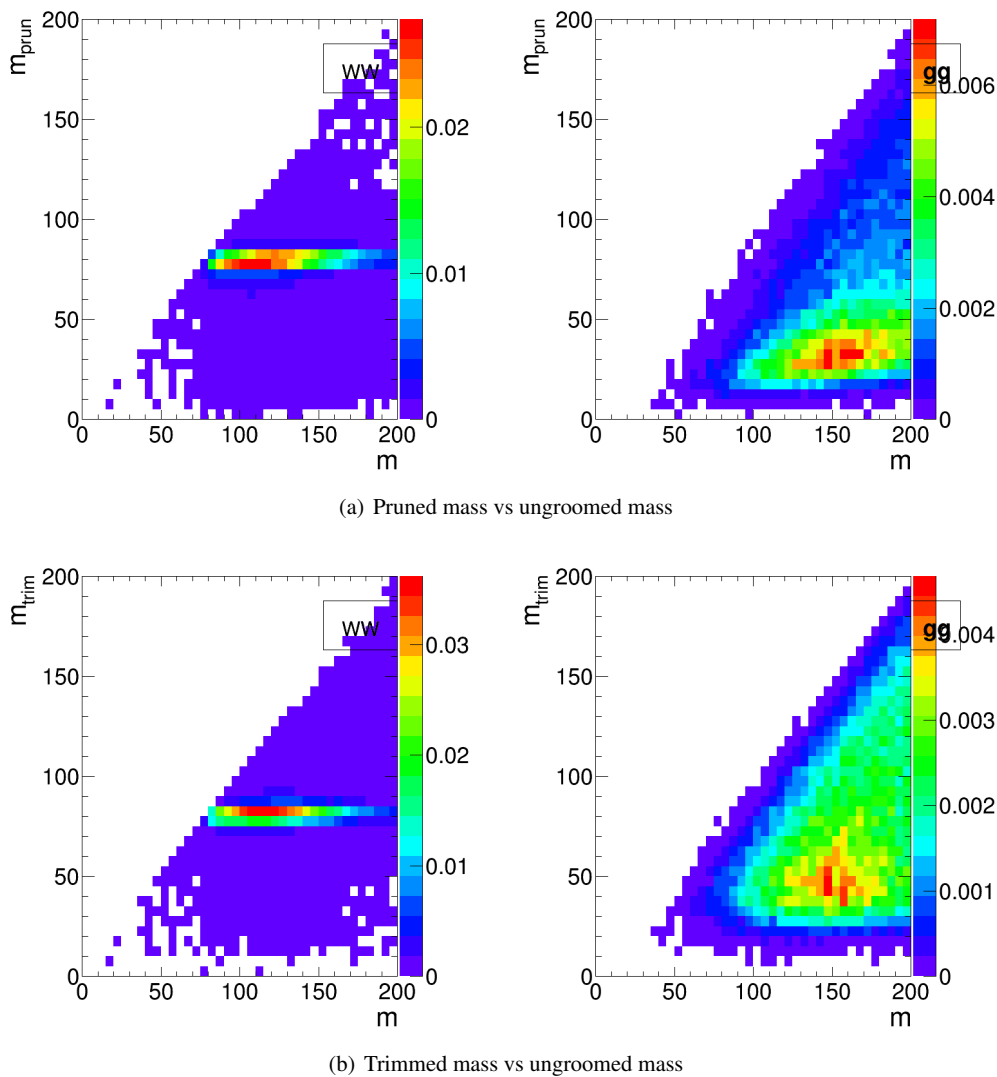


Fig. 27 2-D plots showing the correlation between groomed and ungroomed mass for WW and gg events in the p_T 1.0-1.1 TeV bin using the anti- k_T $R=1.2$ algorithm.

1168 In addition to the jet shape performance, we combine the
 1169 jet shapes with the mass-reconstruction methods described
 1170 above to determine the optimal combined performance.

1171 For determining the performance of multiple variables,
 1172 we combine the relevant tagger output observables and/or jet
 1173 shapes into a boosted decision tree (BDT), which determines
 1174 the optimal cut. Additionally, because each tagger has two
 1175 input parameters, as described in Section 3.3, we scan over
 1176 reasonable values of the parameters to determine the optimal
 1177 value that gives the largest background rejection for each top
 1178 tagging signal efficiency. This allows a direct comparison
 1179 of the optimized version of each tagger. The input values
 1180 scanned for the various algorithms are:

- 1181 – **HEPTopTagger:** $m \in [30, 100]$ GeV, $\mu \in [0.5, 1]$
- 1182 – **JH Tagger:** $\delta_p \in [0.02, 0.15]$, $\delta_R \in [0.07, 0.2]$
- 1183 – **Trimming:** $f_{\text{cut}} \in [0.02, 0.14]$, $R_{\text{trim}} \in [0.1, 0.5]$

- **Pruning:** $z_{\text{cut}} \in [0.02, 0.14]$, $R_{\text{cut}} \in [0.1, 0.6]$

7.2 Single-observable performance

We start by investigating the behaviour of individual jet sub-structure observables. Because of the rich, three-pronged structure of the top decay, it is expected that combinations of masses and jet shapes will far outperform single observables in identifying boosted tops. However, a study of the top-tagging performance of single variables facilitates a direct comparison with the W tagging results in Section 6, and also allows a straightforward examination of the performance of each observable for different p_T and jet radius.

Fig. 28 shows the ROC curves for each of the top-tagging observables, with the bare (ungroomed) jet mass also plotted for comparison. The jet shape observables all perform sub-

stantially worse than jet mass, unlike W tagging for which several observables are competitive with or perform better than jet mass (see, for example, Fig. 10). To understand why this is the case, consider N -subjettiness. The W is two-pronged and the top is three-pronged; therefore, we expect τ_{21} and τ_{32} to be the best-performant N -subjettiness ratio, respectively. However, τ_{21} also contains an implicit cut on the denominator, τ_1 , which is strongly correlated with jet mass. Therefore, τ_{21} combines both mass and shape information to some extent. By contrast, and as is clear in Fig. 28(a), the best shape for top tagging is τ_{32} , which contains no information on the mass. Therefore, it is unsurprising that the shapes most useful for top tagging are less sensitive to the jet mass and under-perform relative to the corresponding observables for W tagging.

Of the two top tagging algorithms, we can see from Figure 28 that the Johns Hopkins (JH) tagger out-performs HEPTopTagger in terms of its signal-to-background separation power in both the top and W candidate masses; this is expected, as the HEPTopTagger was designed to reconstruct moderate p_T top jets in ttH events (for a proposal for a high- p_T variant of the HEPTopTagger, see [57]). In Figure 29 we show the histograms for the top mass output from the JH and HEPTopTagger for different R in the p_T 1.5-1.6 TeV bin, and in Figure 30 for different p_T at $R=0.8$, optimized at a signal efficiency of 30%. One can see from these figures that the likely reason for the better performance of the JH tagger is that, in the HEPTopTagger algorithm, the jet is filtered to select the five hardest subjects, and then three jets are chosen which reconstruct the top mass. This requirement tends to shape a peak in the QCD background around m_t for the HEPTopTagger, while the JH tagger has no such requirement. It has been suggested [58] that performance of the HEPTopTagger may be improved by selecting the three subjects reconstructing the top only among those that pass the W mass constraints, which somewhat reduces the shaping of the background. The discrepancy between the JH and HEPTopTaggers is more pronounced at higher p_T and larger jet radius (see Figs. 33 and 36).

We also see in Figure 28(b) that the top mass from the JH tagger and the HEPTopTagger has superior performance relative to either of the grooming algorithms; this is because the pruning and trimming algorithms do not have inherent W -identification steps and are not optimized for this purpose. Indeed, because of the lack of a W -identification step grooming algorithms are forced to strike a balance between under-grooming the jet, which broadens the signal peak due to UE contamination and features a larger background rate, and over-grooming the jet, which occasionally throws out the b -jet and preserves only the W components inside the jet. We demonstrate this effect in Figures 29 and 30, showing that with $\epsilon_{\text{sig}} = 0.3 - 0.35$, the optimal performance of the tagger over-grooms a substantial fraction of the jets (20 – 30%), leading to a spurious second peak at the W mass.

This effect is more pronounced at large R and p_T , since more aggressive grooming is required in these limits to combat the increased contamination from UE and QCD radiation.

In Figures 31 and 33 we directly compare ROC curves for jet shape observable performance and top mass performance respectively in the three different p_T bins considered whilst keeping the jet radius fixed at $R=0.8$. The input parameters of the taggers, groomers and shape variables are separately optimized in each p_T bin. One can see from Figure 31 that the tagging performance of jet shapes do not change substantially with p_T . The observables $\tau_{32}^{(\beta=1)}$ and Qjet volatility Γ have the most variation and tend to degrade with higher p_T , as can be seen in Figure 32. This makes sense, as higher- p_T QCD jets have more, harder emissions within the jet, giving rise to substructure that fakes the signal. By contrast, from Figure 33 we can see that most of the top mass observables have superior performance at higher p_T due to the radiation from the top quark becoming more collimated. The notable exception is the HEPTopTagger, which degrades at higher p_T , likely in part due to the background-shaping effects discussed earlier.

In Figures 34 and 36 we directly compare ROC curves for jet shape observable performance and top mass performance respectively for the three different jet radii considered within the p_T 1.5-1.6 TeV bin. Again, the input parameters of the taggers, groomers and shape variables are separately optimized for each jet radius. We can see from these figures that most of the top tagging variables, both shape and reconstructed top mass, perform best for smaller radius. This is likely because, at such high p_T , most of the radiation from the top quark is confined within $R = 0.4$, and having a larger jet radius makes the observable more susceptible to contamination from the underlying event and other uncorrelated radiation. In Figure 35, we compare the individual top signal and QCD background distributions for each shape variable considered in the p_T 1.5-1.6 TeV bin for the various jet radii. One can see that the distributions for both signal and background broaden with increasing R , degrading the discriminating power. For $C_2^{(\beta=1)}$ and $C_3^{(\beta=1)}$, the background distributions are shifted upward as well. Therefore, the discriminating power generally gets worse with increasing R . The main exception is for $C_3^{(\beta=1)}$, which performs optimally at $R = 0.8$; in this case, the signal and background coincidentally happen to have the same distribution around $R = 0.4$, and so $R = 0.8$ gives better discrimination.

7.3 Performance of multivariable combinations

We now consider various BDT combinations of the observables from Section 7.2, using the techniques described in Section 4. In particular, we consider the performance of in-

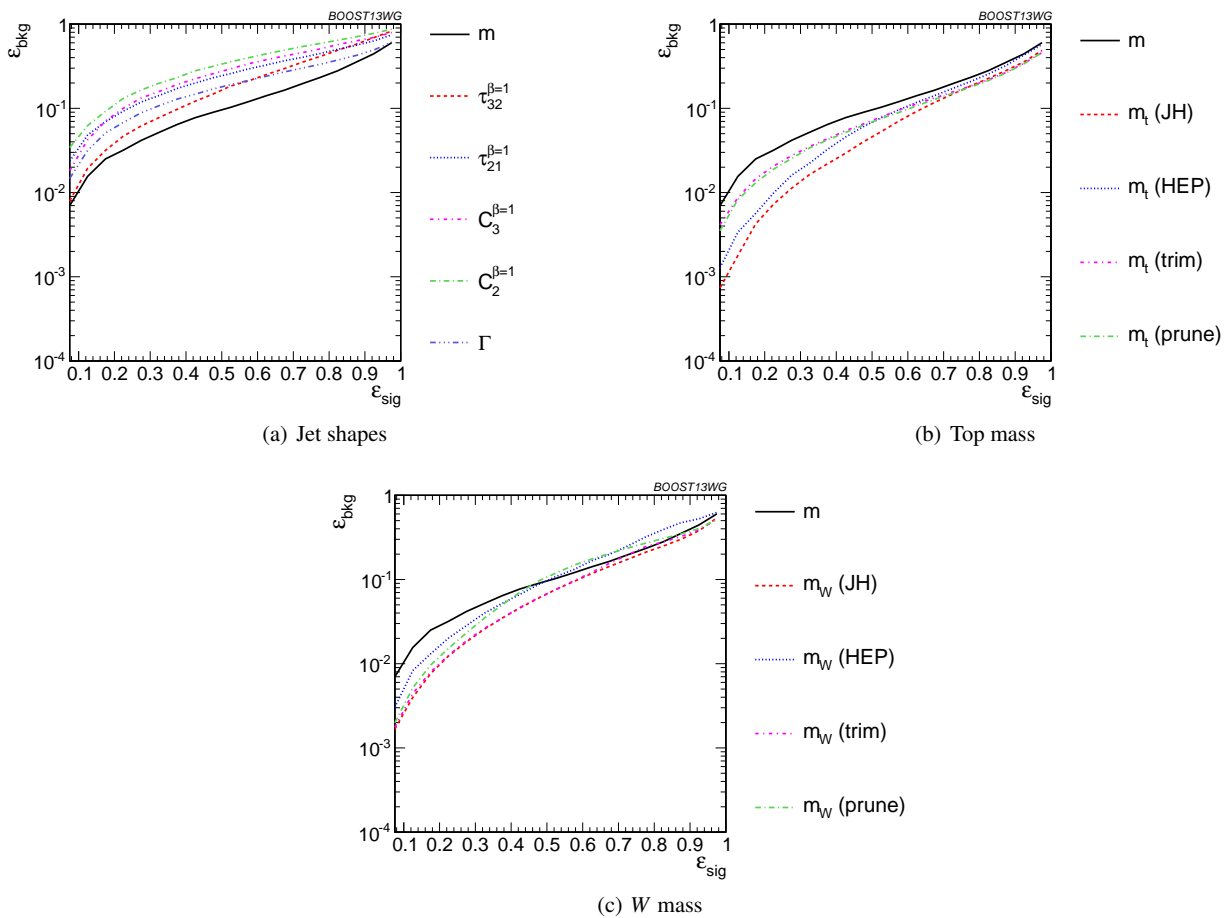


Fig. 28 Comparison of single-variable top-tagging performance in the $p_T = 1 - 1.1$ GeV bin using the anti- k_T , $R=0.8$ algorithm.

1301 individual taggers such as the JH tagger and HEPTopTagger
 1302 which output information about the top and W candidate
 1303 masses and the helicity angle; groomers, such as trimming
 1304 and pruning, which remove soft, uncorrelated radiation from
 1305 the top candidate to improve mass reconstruction, and
 1306 which we have added a W reconstruction step; and the com-
 1307 bination of the outputs of the above taggers/groomers, both
 1308 with each other, and with shape variables such as N -subjettiness
 1309 ratios and energy correlation ratios. For all observables with
 1310 tuneable input parameters, we scan and optimize over real-
 1311 istic values of such parameters, as described in Section 7.1.

1312 In Figure 37, we directly compare the performance of
 1313 the HEPTopTagger, the JH tagger, trimming, and pruning
 1314 in the $p_T = 1 - 1.1$ TeV bin using jet radius $R=0.8$, where
 1315 both m_t and m_W are used in the groomers. Generally, we
 1316 find that pruning, which does not naturally incorporate sub-
 1317 jets into the algorithm, does not perform as well as the oth-
 1318 ers. Interestingly, trimming, which does include a subject-
 1319 identification step, performs comparably to the HEPTopTag-
 1320 ger over much of the range, possibly due to the background
 1321 shaping observed in Section 7.2. By contrast, the JH tag-
 1322 ger outperforms the other algorithms. To determine whether

there is complementary information in the mass outputs from
 different top taggers, we also consider in Figure 37 a mul-
 tivari-able combination of all of the JH and HEPTopTagger
 outputs. The maximum efficiency of the combined JH and
 HEPTopTaggers is limited, as some fraction of signal events
 inevitably fails either one or other of the taggers. We do see
 a 20-50% improvement in performance when combining all
 outputs, which suggests that the different algorithms used to
 identify the top and W for different taggers contains com-
 plementary information.

In Figure 38 we present the results for multivariable com-
 binations of the top tagger outputs with and without shape
 variables. We see that, for both the HEPTopTagger and the
 JH tagger, the shape observables contain additional infor-
 mation uncorrelated with the masses and helicity angle, and
 give on average a factor 2-3 improvement in signal discrimi-
 nation. We see that, when combined with the tagger outputs,
 both the energy correlation functions $C_2 + C_3$ and the N -
 subjettiness ratios $\tau_{21} + \tau_{32}$ give comparable performance,
 while the Qjet mass volatility is slightly worse; this is un-
 surprising, as Qjets accesses shape information in a more
 indirect way from other shape observables. Combining all

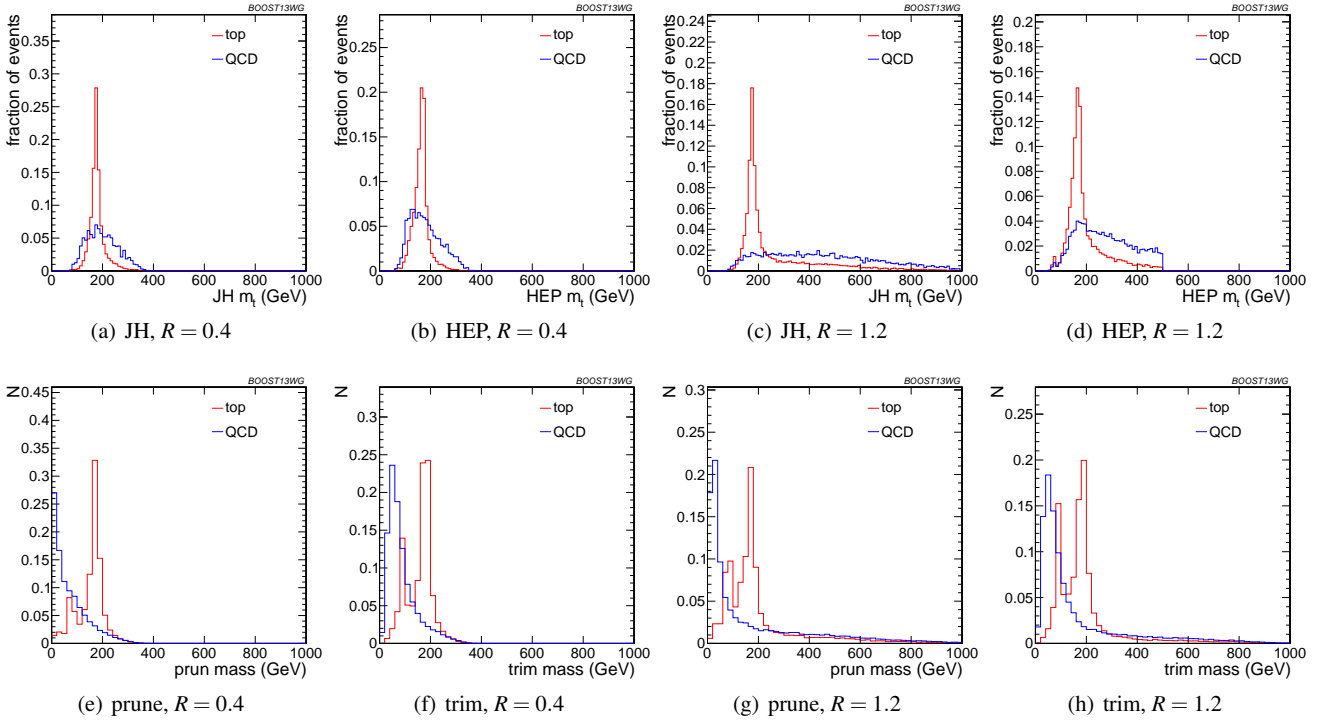


Fig. 29 Comparison of top mass reconstruction with the Johns Hopkins (JH), HEPTopTaggers (HEP), pruning, and trimming at different R using the anti- k_T algorithm, $p_T = 1.5 - 1.6$ TeV. Each histogram is shown for the working point optimized for best performance with m_t in the $0.3 - 0.35$ signal efficiency bin, and is normalized to the fraction of events passing the tagger. In this and subsequent plots, the HEPTopTagger distribution cuts off at 500 GeV because the tagger fails to tag jets with a larger mass.

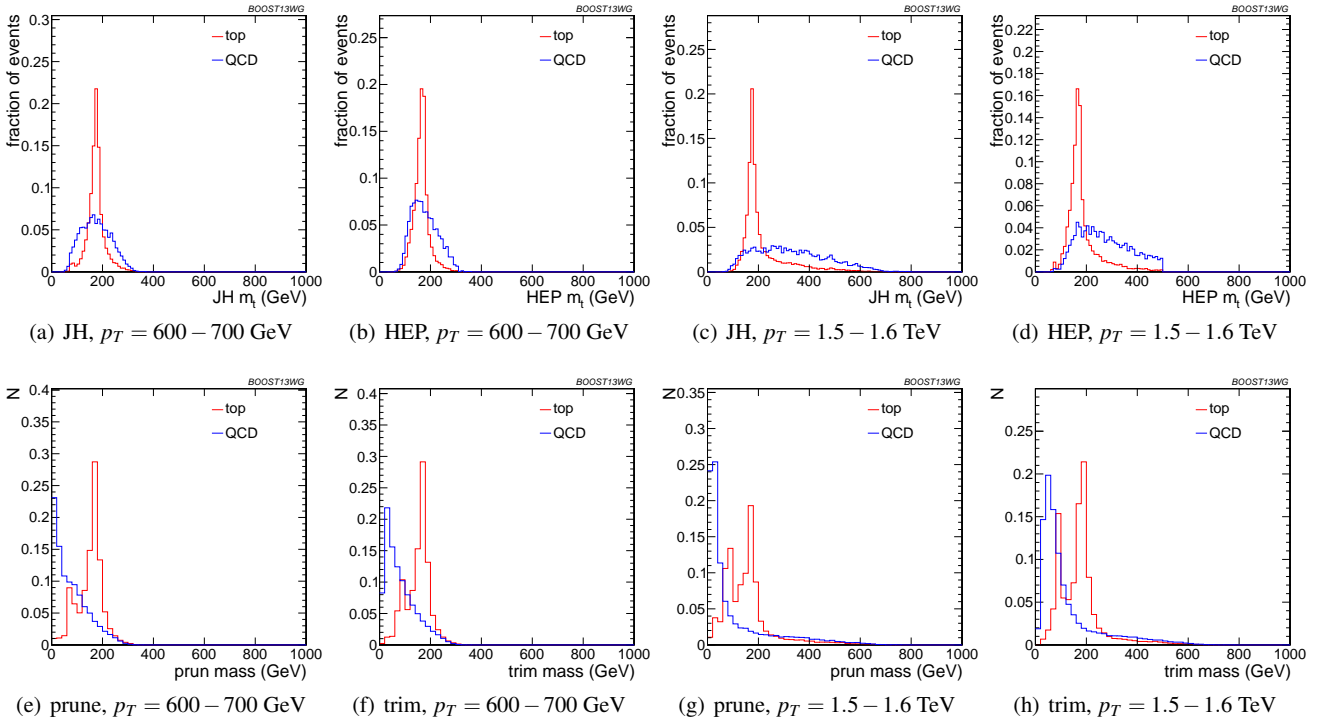


Fig. 30 Comparison of top mass reconstruction with the Johns Hopkins (JH), HEPTopTaggers (HEP), pruning, and trimming at different p_T using the anti- k_T algorithm, $R = 0.8$. Each histogram is shown for the working point optimized for best performance with m_t in the $0.3 - 0.35$ signal efficiency bin, and is normalized to the fraction of events passing the tagger.

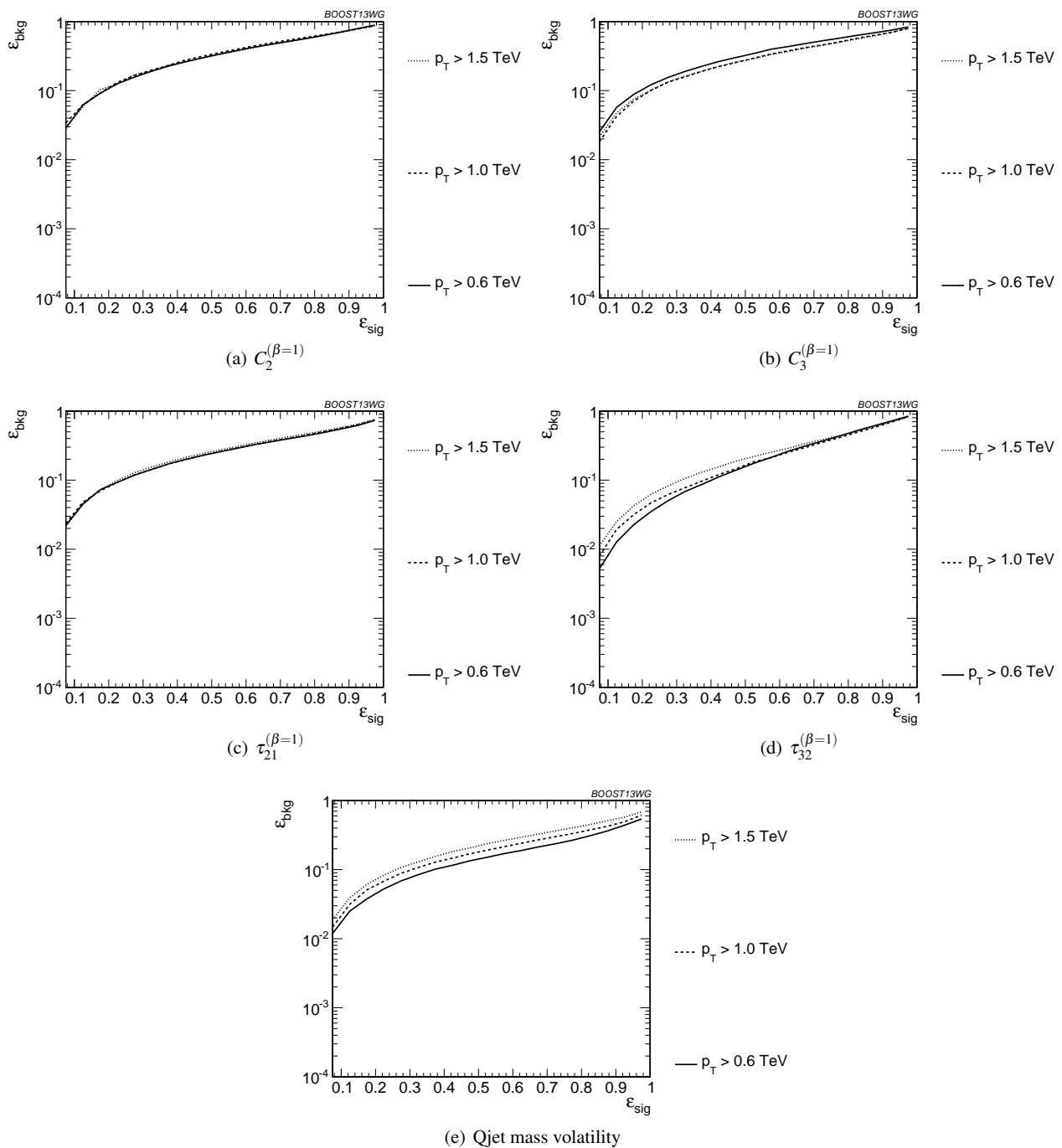


Fig. 31 Comparison of individual jet shape performance at different p_T using the anti- k_T $R=0.8$ algorithm.

1345 shape observables with a single top tagger provides even greater
 1346 greater enhancement in discrimination power. We directly compare
 1347 the performance of the JH and HEPTopTaggers in Figure 38(c).
 1348 Combining the taggers with shape information nearly erases the
 1349 difference between the tagging methods observed in Figure 37;
 1350 this indicates that combining the shape information with the
 1351 HEPTopTagger identifies the differences between signal and
 1352 background missed by the tagger alone.

1353 This also suggests that further improvement to discriminating
 1354 power may be minimal, as various multivariable combinations
 1355 are converging to within a factor of 20% or so.

1356 In Figure 39 we present the results for multivariable combinations
 1357 of groomer outputs with and without shape variables. As with
 1358 the tagging algorithms, combinations of groomers with shape
 1359 observables improves their discriminating power;

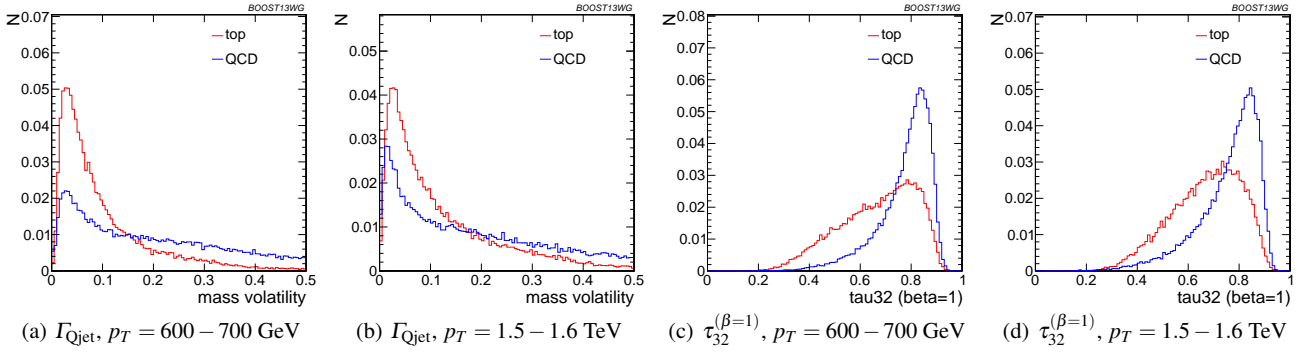


Fig. 32 Comparison of Γ_{Qjet} and $\tau_{32}^{\beta=1}$ at $R = 0.8$ and different values of the p_T . These shape observables are the most sensitive to varying p_T .

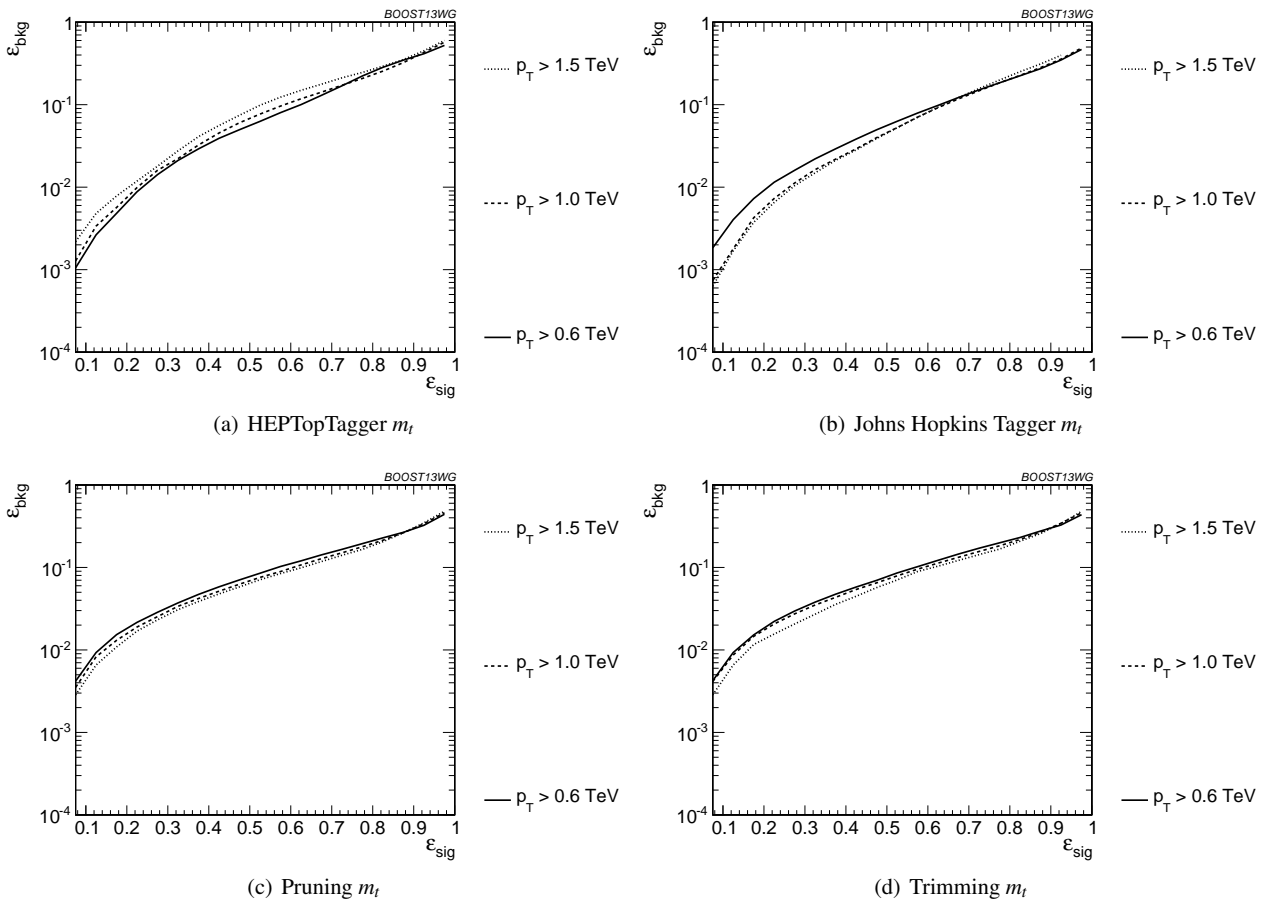


Fig. 33 Comparison of top mass performance of different taggers at different p_T using the anti- k_T $R=0.8$ algorithm.

1361 combinations with $\tau_{32} + \tau_{21}$ perform comparably to those
 1362 with $C_3 + C_2$, and both of these are superior to combina-
 1363 tions with the mass volatility, Γ . Substantial improvement is
 1364 further possible by combining the groomers with all shape
 1365 observables. Not surprisingly, the taggers that lag behind
 1366 in performance enjoy the largest gain in signal-background
 1367 discrimination with the addition of shape observables. Once
 1368 again, in Figure 39(c), we find that the differences between

1369 pruning and trimming are erased when combined with shape
 1370 information.

1371 Finally, in Figure 40, we compare the performance of
 1372 each of the tagger/groomers when their outputs are com-
 1373 bined with all of the shape observables considered. One can
 1374 see that the discrepancies between the performance of the
 1375 different taggers/groomers all but vanishes, suggesting per-
 1376 haps that we are here utilising all available signal-background
 1377 discrimination information, and that this is the optimal top

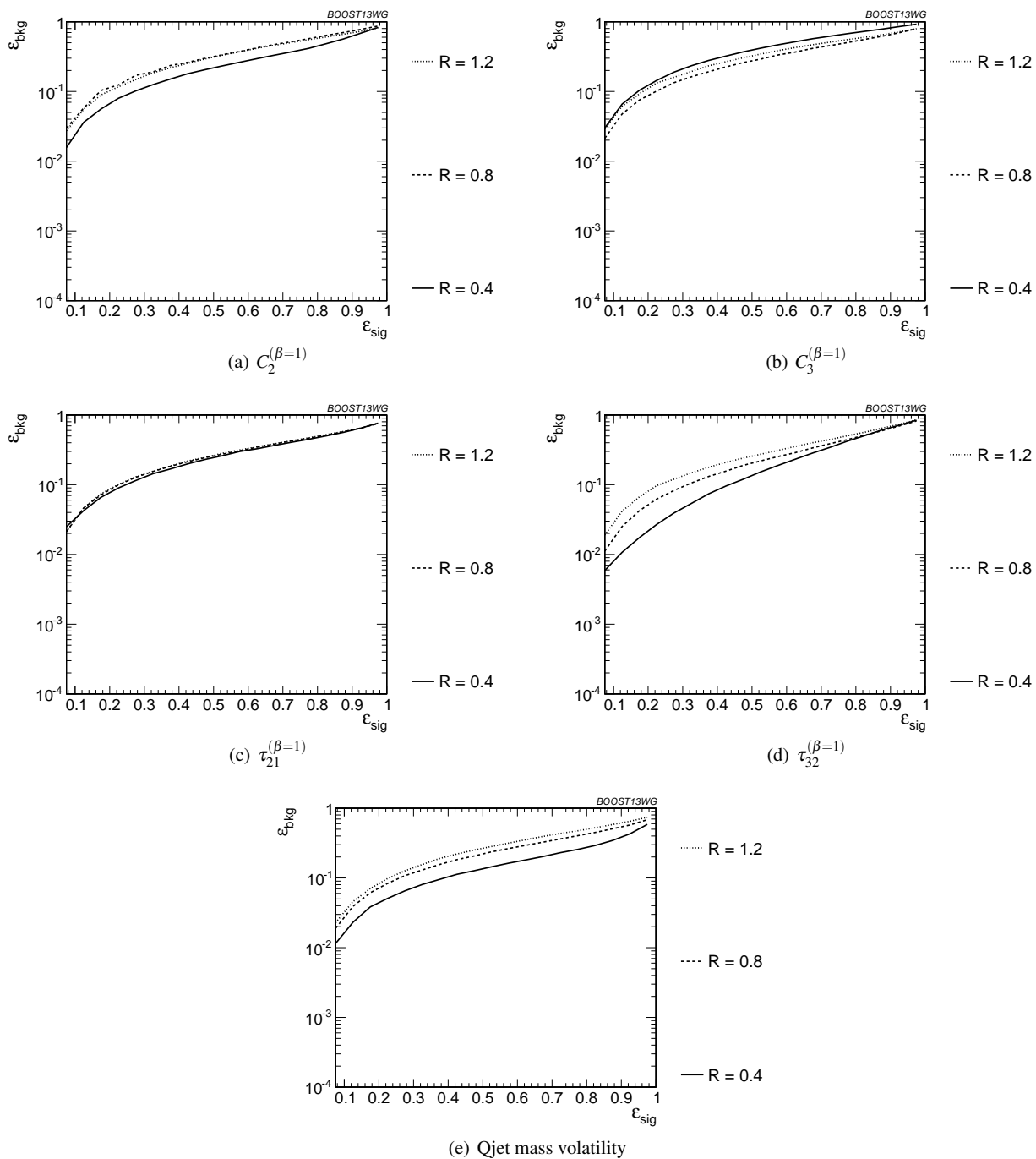


Fig. 34 Comparison of individual jet shape performance at different R in the $p_T = 1.5 - 1.6$ TeV bin.

1378 tagging performance that could be achieved in these conditions.
1379

1380 Up to this point we have just considered the combined
1381 multivariable performance in the p_T 1.0-1.1 TeV bin with
1382 jet radius $R=0.8$. We now compare the BDT combinations
1383 of tagger outputs, with and without shape variables, at dif-
1384 ferent p_T . The taggers are optimized over all input param-
1385 eters for each choice of p_T and signal efficiency. As with the

1386 single-variable study, we consider anti- k_T jets clustered with
1387 $R = 0.8$ and compare the outcomes in the $p_T = 500 - 600$
1388 GeV, $p_T = 1 - 1.1$ TeV, and $p_T = 1.5 - 1.6$ TeV bins. The
1389 comparison of the taggers/groomers is shown in Figure 41.
1390 The behaviour with p_T is qualitatively similar to the be-
1391 haviour of the m_t observable for each tagger/groomer shown
1392 in Figure 33; this suggests that the p_T behaviour of the tag-
1393 gers is dominated by the top mass reconstruction. As before,

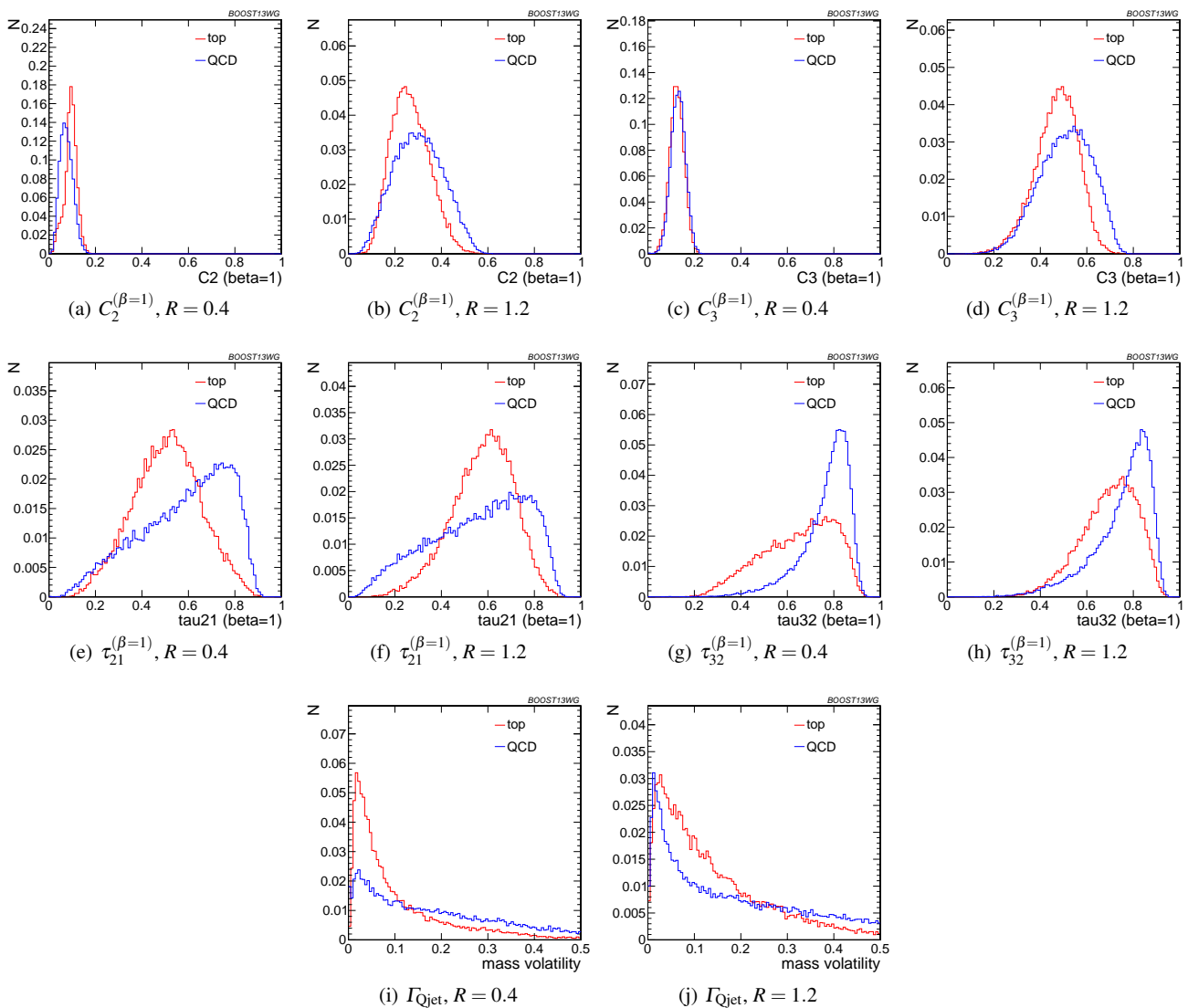


Fig. 35 Comparison of various shape observables in the $p_T = 1.5 - 1.6$ TeV bin and different values of the anti- k_T radius R .

1394 the HEPTopTagger performance degrades slightly with in-410
 1395 creased p_T due to the background shaping effect, while the 1411
 1396 JH tagger and groomers modestly improve in performance. 1412

1397 In Figure 42, we show the p_T dependence of BDT 1413
 1398 combinations of the JH tagger output combined with shape ob- 1414
 1399 servables. We find that the curves look nearly identical: the 1415
 1400 p_T dependence is dominated by the top mass reconstruc- 1416
 1401 tion, and combining the tagger outputs with different shape 1417
 1402 observables does not substantially change this behaviour. 1418
 1403 The same holds true for trimming and pruning. By contrast, 1419
 1404 HEPTopTagger ROC curves, shown in Figure 43, do change 1420
 1405 somewhat when combined with different shape observables. 1421
 1406 At high p_T , we find that combining the HEPTopTagger with 1422
 1407 $C_3^{(\beta=1)}$, which in Figure 31(b) is seen to have some mod- 1423
 1408 est improvement at high p_T , can improve its performance 1424
 1409 1425

Combining the HEPTopTagger with multiple shape observ-
 1409 ables gives the maximum improvement in performance at
 1410 high p_T relative to at low p_T .

In Figure 44 we compare the BDT combinations of tag-
 1411 ger outputs, with and without shape variables, at different jet
 1412 radius R in the $p_T = 1.5 - 1.6$ TeV bin. The taggers are opti-
 1413 mized over all input parameters for each choice of R and sig-
 1414 nal efficiency. We find that, for all taggers and groomers, the
 1415 performance is always best at small R ; the choice of R is suf-
 1416 ficiently large to admit the full top quark decay at such high
 1417 p_T , but is small enough to suppress contamination from addi-
 1418 tional radiation. This is not altered when the taggers are
 1419 combined with shape observable. For example, in Figure 45
 1420 is shown the dependence on R of the JH tagger when com-
 1421 bined with shape observables, where one can see that the

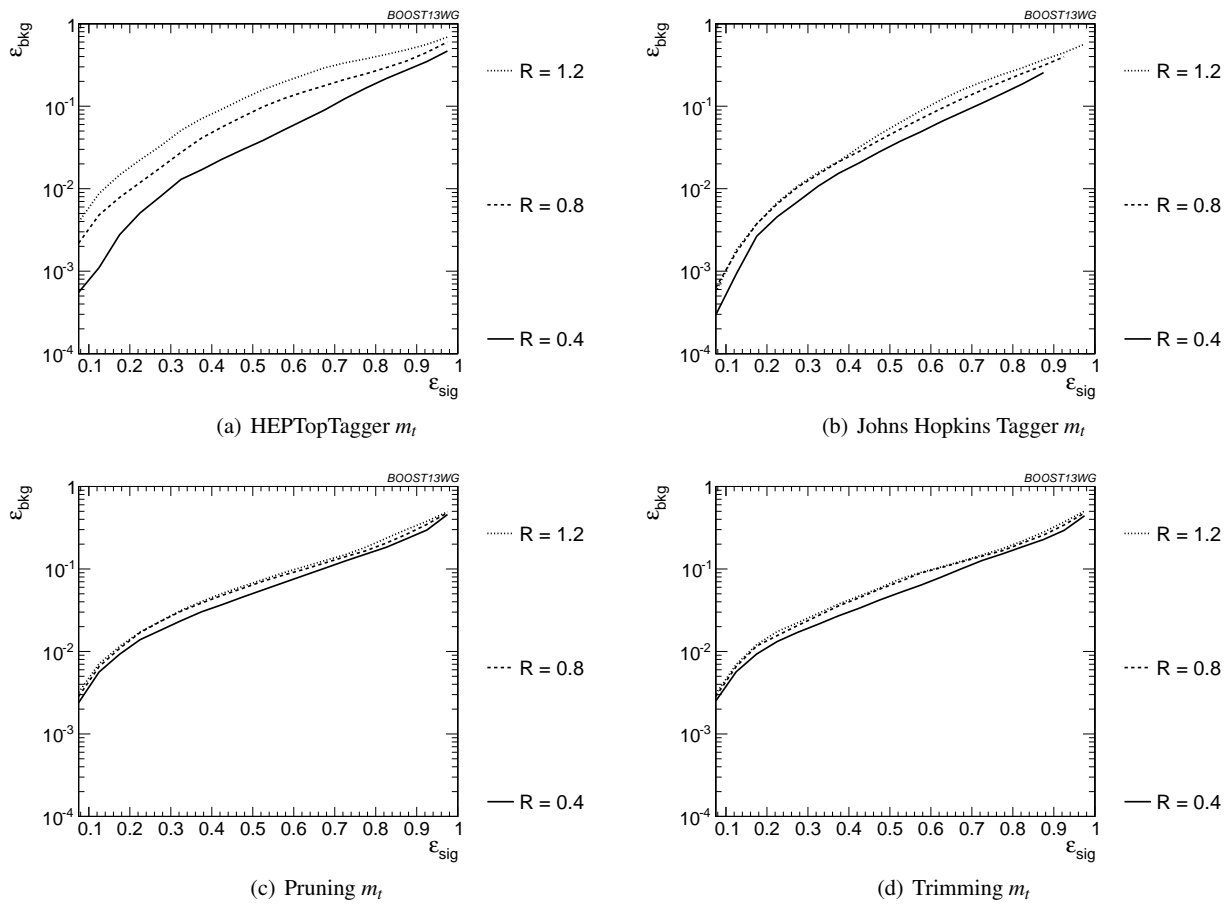


Fig. 36 Comparison of top mass performance of different taggers at different R in the $p_T = 1.5 - 1.6$ TeV bin.

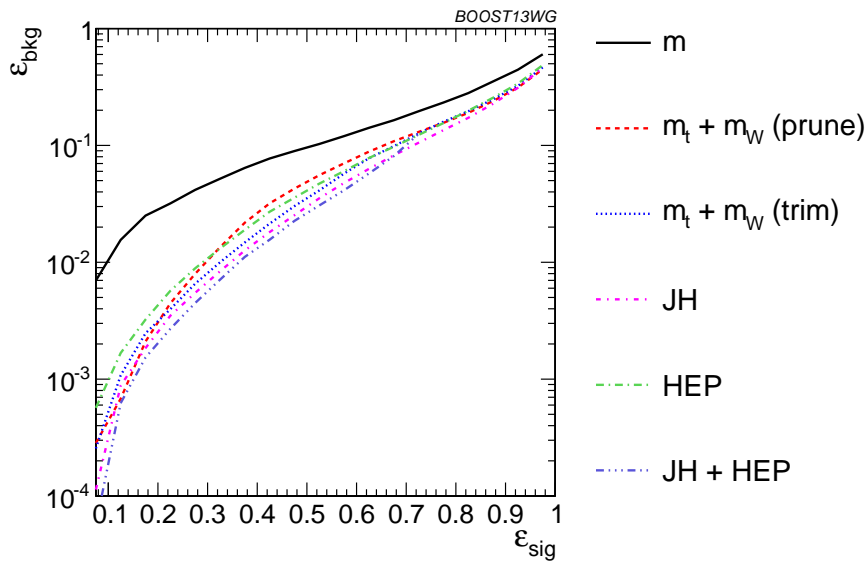


Fig. 37 The performance of the various taggers in the $p_T = 1 - 1.1$ TeV bin using the anti- k_T $R=0.8$ algorithm. For the groomers a BDT combination of the reconstructed m_t and m_W are used. Also shown is a multivariable combination of all of the JH and HEPTopTagger outputs. The ungroomed mass performance is shown for comparison.

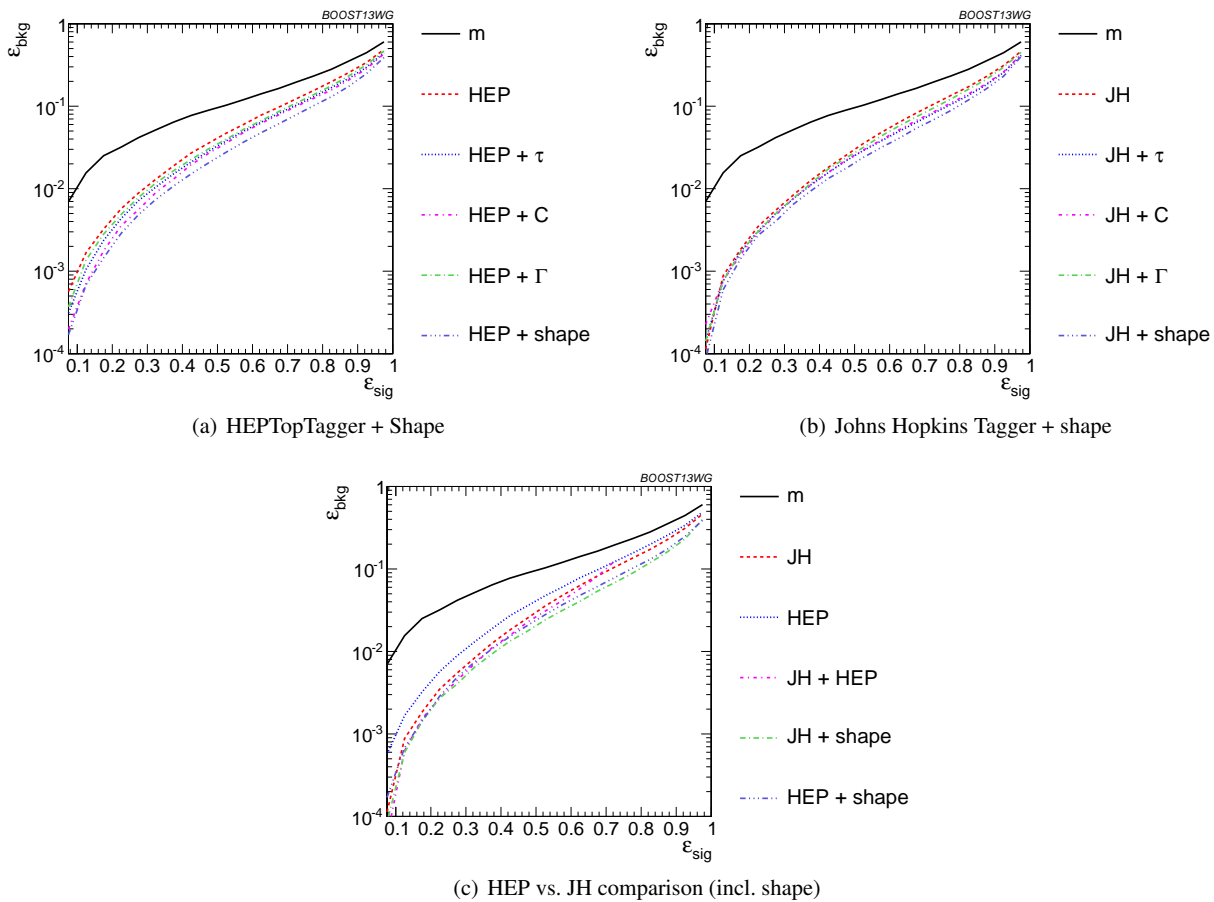


Fig. 38 The performance of BDT combinations of the JH and HepTopTagger outputs with various shape observables in the $p_T = 1 - 1.1$ TeV bin using the anti- k_T $R=0.8$ algorithm. Taggers are combined with the following shape observables: $\tau_{21}^{(\beta=1)} + \tau_{32}^{(\beta=1)}$, $C_2^{(\beta=1)} + C_3^{(\beta=1)}$, Γ_{Qjet} , and all of the above (denoted “shape”).

1426 R -dependence is identical for all combinations. The same 1443
 1427 holds true for the HEPTopTagger, trimming, and pruning. 1444

1428 7.4 Performance at Sub-Optimal Working Points 1448

1429 Up until now, we have re-optimized our tagger and groomer 1450
 1430 parameters for each p_T , R , and signal efficiency working 1451
 1431 point. In reality, experiments will choose a finite set of work 1452
 1432 ing points to use. How do our results hold up when this 1453
 1433 is taken into account? To address this concern, we repli 1454
 1434 cate our analyses, but only optimize the top taggers for 1455
 1435 particular p_T/R /efficiency and apply the same parameters 1456
 1436 to other scenarios. This allows us to determine the exten 1457
 1437 to which re-optimization is necessary to maintain the high 1458
 1438 signal-background discrimination power seen in the top tag 1459
 1439 ging algorithms we study. The shape observables typically 1460
 1440 do not have any input parameters to optimize. Therefore, we 1461
 1441 focus on the taggers and groomers, and their combination 1462
 1442 with shape observables, in this section. 1463

Optimizing at a single p_T : We show in Figure 46 the per-
 formance of the top taggers, using just the reconstructed top
 mass as the discriminating variable, with all input param-
 eters optimized to the $p_T = 1.5 - 1.6$ TeV bin, relative to
 the performance optimized at each p_T . We see that while
 the performance degrades by about 50% when the high- p_T
 optimized points are used at other momenta, this is only an
 order-one adjustment of the tagger performance, with trim-
 ming and the Johns Hopkins tagger degrading the most. The
 jagged behaviour of the points is due to the finite resolu-
 tion of the scan. We also observe a particular effect asso-
 ciated with using suboptimal taggers: since taggers some-
 times fail to return a top candidate, parameters optimized
 for a particular efficiency ϵ_S at $p_T = 1.5 - 1.6$ TeV may
 not return enough signal candidates to reach the same effi-
 ciency at a different p_T . Consequently, no point appears
 for that p_T value. This is not often a practical concern, as
 the largest gains in signal discrimination and significance
 are for smaller values of ϵ_S , but it is something that must
 be considered when selecting benchmark tagger parameters
 and signal efficiencies.

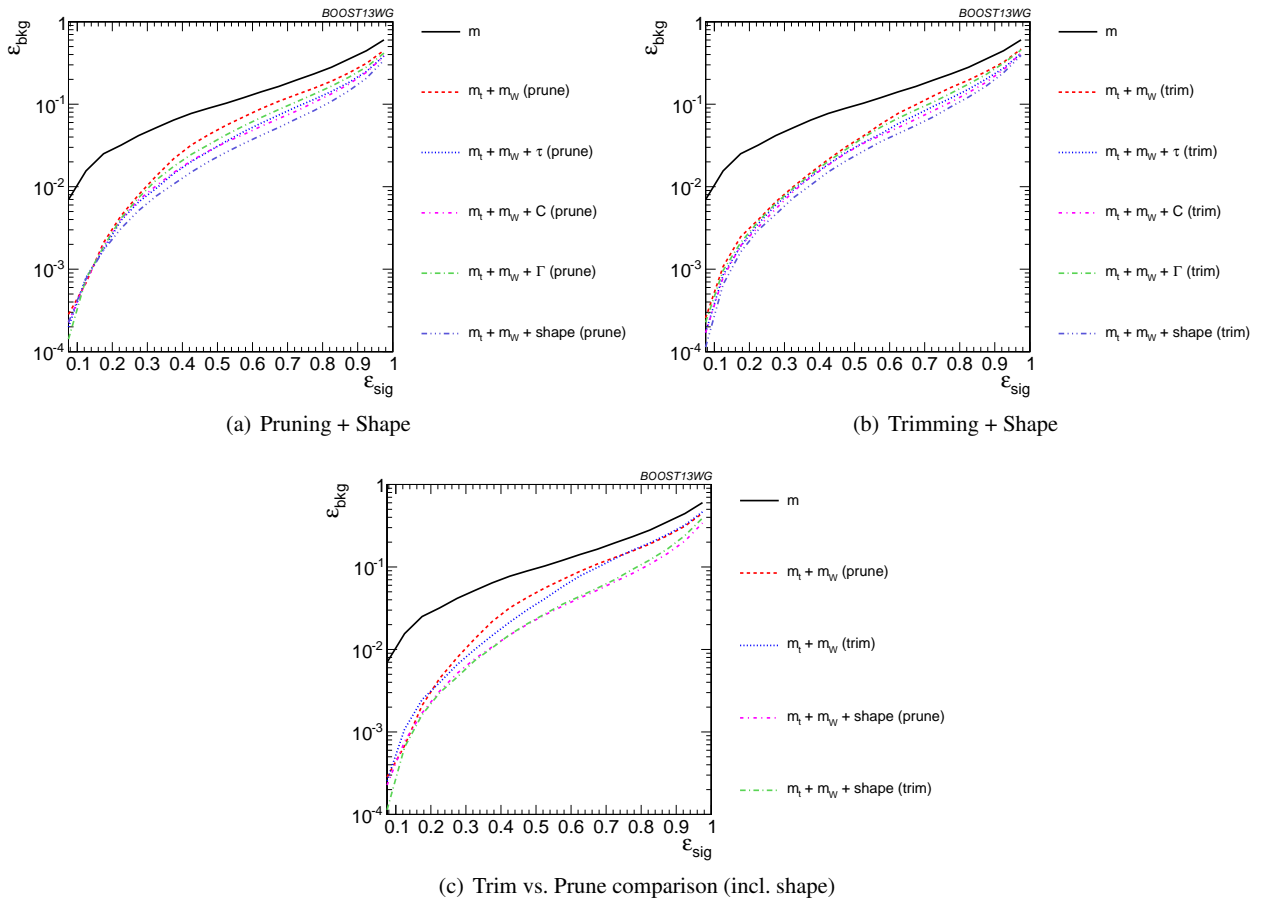


Fig. 39 The performance of the BDT combinations of the trimming and pruning outputs with various shape observables in the $p_T = 1 - 1.1$ TeV bin using the anti- k_T $R=0.8$ algorithm. Groomer mass outputs are combined with the following shape observables: $\tau_{21}^{(\beta=1)} + \tau_{32}^{(\beta=1)}$, $C_2^{(\beta=1)} + C_3^{(\beta=1)}$, Γ_{Qjet} , and all of the above (denoted “shape”).

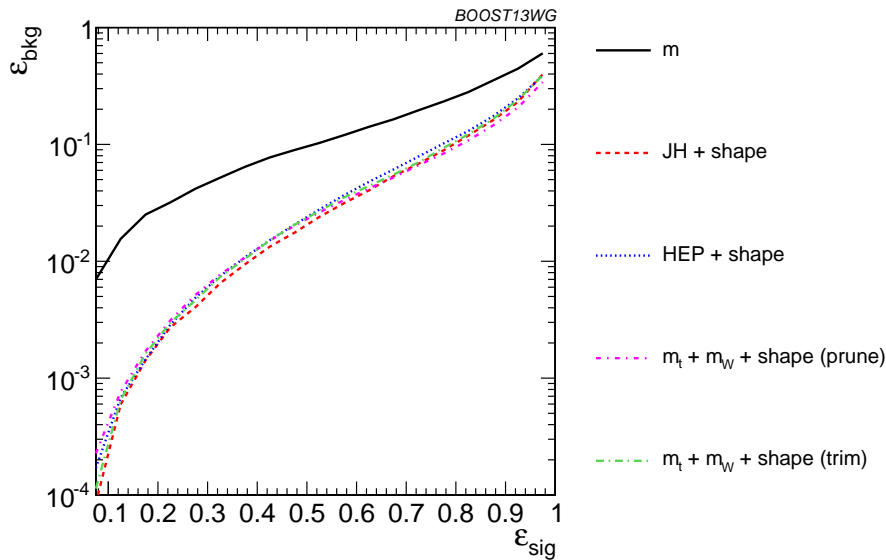


Fig. 40 Comparison of the performance of the BDT combinations of all the groomer/tagger outputs with all the available shape observables in the $p_T = 1 - 1.1$ TeV bin using the anti- k_T $R=0.8$ algorithm. Tagger/groomer outputs are combined with all of the following shape observables: $\tau_{21}^{(\beta=1)} + \tau_{32}^{(\beta=1)}$, $C_2^{(\beta=1)} + C_3^{(\beta=1)}$, Γ_{Qjet} .

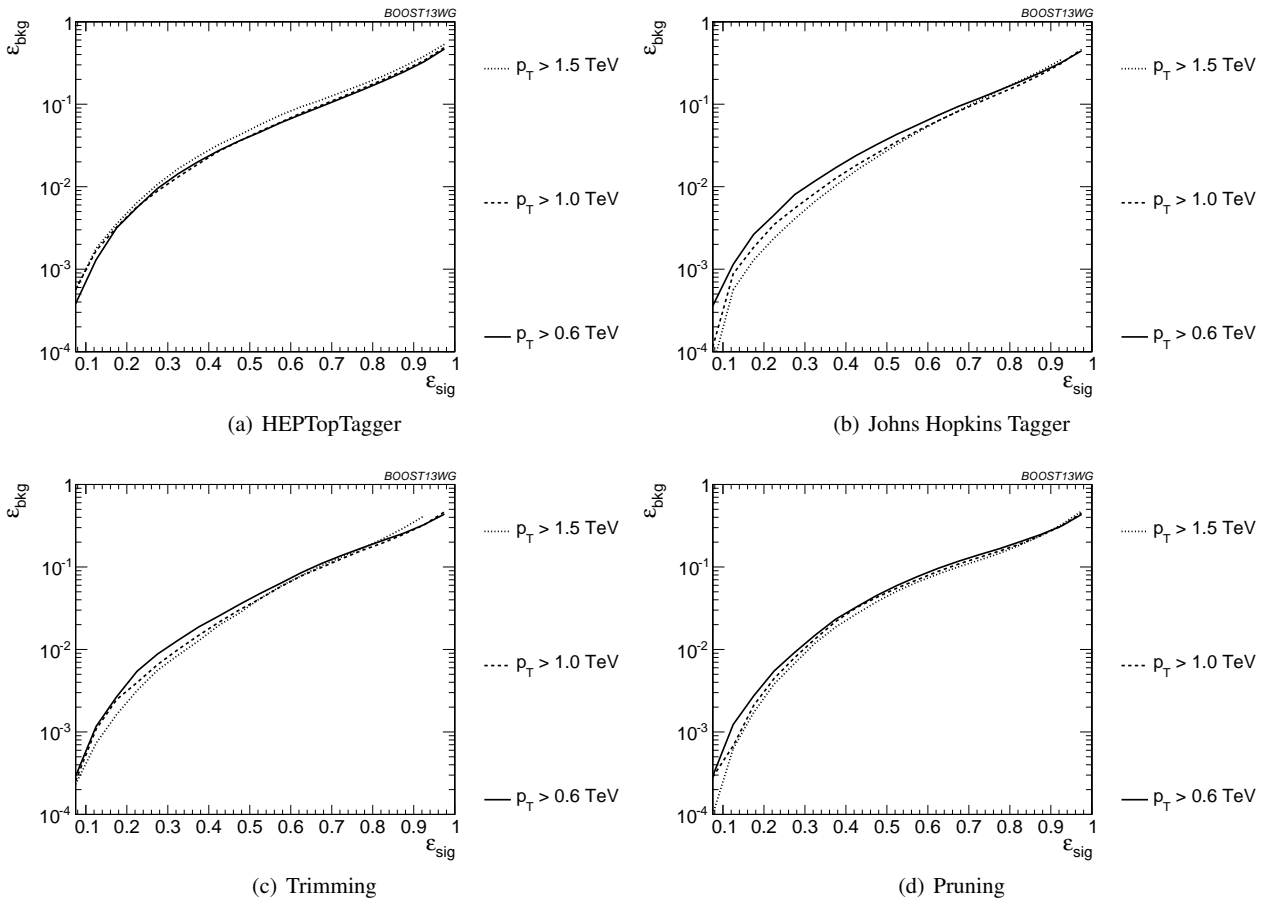


Fig. 41 Comparison of BDT combination of tagger performance at different p_T using the anti- k_T $R=0.8$ algorithm.

1464 The degradation in performance is more pronounced for
 1465 the BDT combinations of the full tagger outputs, shown in
 1466 Figure 47), particularly at very low signal efficiency where
 1467 the optimization picks out a cut on the tail of some distri-
 1468 bution that depends precisely on the p_T/R of the jet. Once
 1469 again, trimming and the Johns Hopkins tagger degrade more
 1470 markedly. Similar behaviour holds for the BDT combina-
 1471 tions of tagger outputs plus all shape observables.
 1472

1473 **Optimizing at a single R :** We perform a similar analysis,
 1474 optimizing tagger parameters for each signal efficiency at
 1475 $R = 1.2$, and then use the same parameters for smaller R , in
 1476 the p_T 1.5-1.6 TeV bin. In Figure 48 we show the ratio of the
 1477 performance of the top taggers, using just the reconstructed
 1478 top mass as the discriminating variable, with all input pa-
 1479 rameters optimized to the $R = 1.2$ values compared to input
 1480 parameters optimized separately at each radius. While the
 1481 performance of each observable degrades at small ϵ_{sig} com-
 1482 pared to the optimized search, the HEPTopTagger fares the
 1483 worst as the observed is quite sensitive to the selected value
 1484 of R . It is not surprising that a tagger whose top mass recon-
 1485 struction is susceptible to background-shaping at large R and

p_T would require a more careful optimization of parameters to obtain the best performance.

The same holds true for the BDT combinations of the full tagger outputs, shown in Figure 49). The performance for the sub-optimal taggers is still within an $O(1)$ factor of the optimized performance, and the HEPTopTagger performs better with the combination of all of its outputs relative to the performance with just m_t . The same behaviour holds for the BDT combinations of tagger outputs and shape observables.

Optimizing at a single efficiency: The strongest assumption we have made so far is that the taggers can be re-optimized for each signal efficiency point. This is useful for making a direct comparison of the power of different top tagging algorithms, but is not particularly practical for the LHC analyses. We now consider the effects when the tagger inputs are optimized once, in the $\epsilon_S = 0.3 - 0.35$ bin, and then used to determine the full ROC curve. We do this in the p_T 1 - 1.1 TeV bin and with $R = 0.8$.

The performance of each tagger, normalized to its performance optimized in each bin, is shown in Figure 50 for

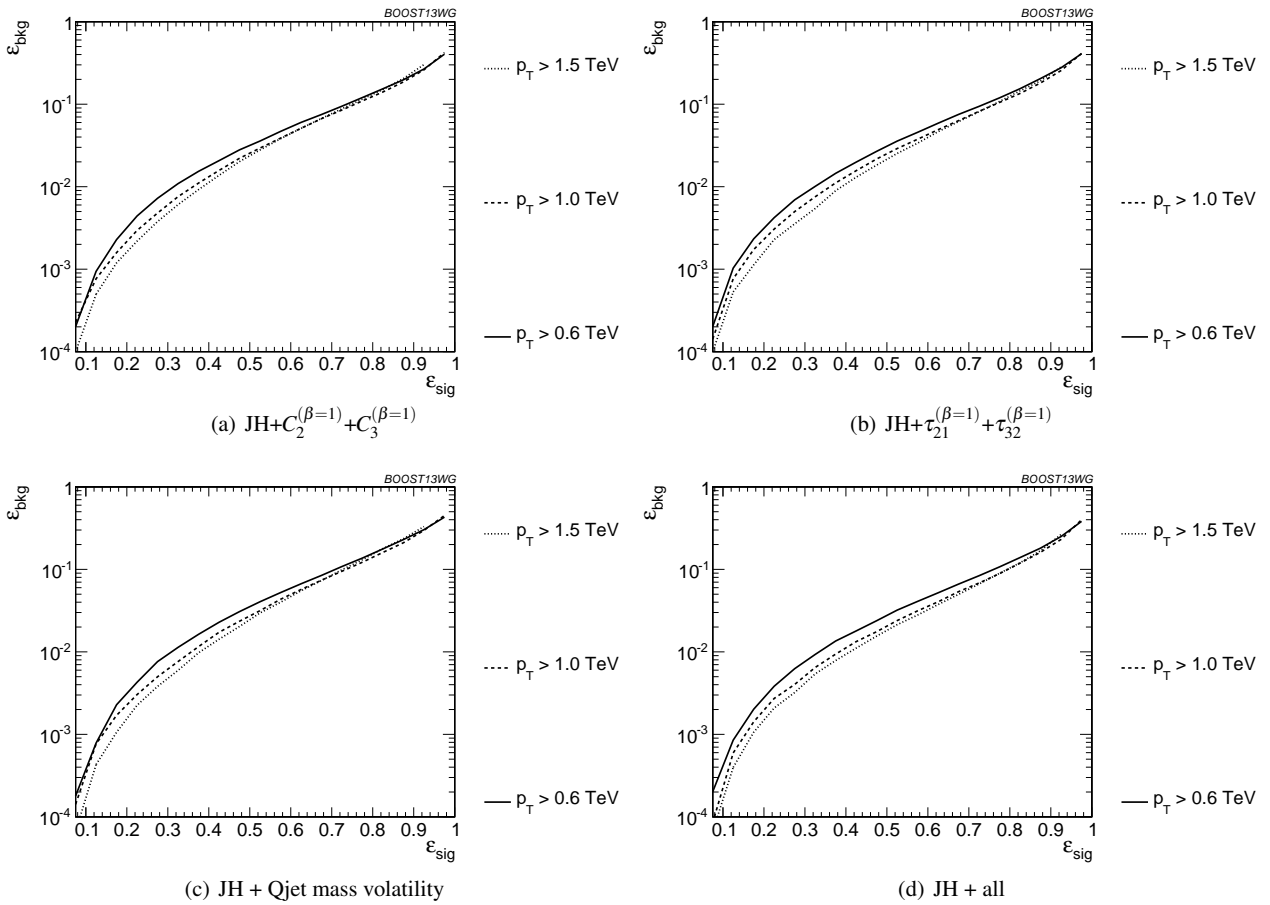


Fig. 42 Comparison of BDT combination of JH tagger + shape at different p_T using the anti- k_T $R=0.8$ algorithm.

1508 cuts on the top mass and W mass, and in Figure 51 for BDT
 1509 combinations of tagger outputs and shape variables. In both
 1510 plots, it is apparent that optimizing the taggers in the 0.3-
 1511 0.35 efficiency bin gives comparable performance over ef-
 1512 ficiencies ranging from 0.2-0.5, although performance de-
 1513 grades at small and large signal efficiencies. Pruning appears
 1514 to give especially robust signal-background discrimination
 1515 without re-optimization, possibly due to the fact that there
 1516 are no absolute distance or p_T scales that appear in the algo-
 1517 rithm. Figures 50 and 51 suggest that, while optimization at
 1518 all signal efficiencies is a useful tool for comparing differ-
 1519 ent algorithms, it is not crucial to achieve good top-tagging
 1520 performance in experiments.

1521 7.5 Conclusions

1522 We have studied the performance of various jet substructure
 1523 observables, groomed masses, and top taggers to study the
 1524 performance of top tagging at different p_T and jet radius pa-
 1525 rameter. At each p_T , R , and signal efficiency working point,
 1526 we optimize the parameters for those observables with tuned
 1527 able inputs. Overall, we have found that these techniques

1540 individually and in combination, continue to perform well
 1541 at high p_T , which is important for future LHC running. In
 1542 general, the John Hopkins tagger performs best, while jet
 1543 grooming algorithms under-perform relative to the best top
 taggers due to the lack of an optimized W -identification step;
 as expected from its design, the HEPTopTagger performance
 degrades at high p_T . Tagger performance can be improved
 by a further factor of 2-4 through combination with jet sub-
 structure observables such as τ_{32} , C_3 , and Qjet mass volatili-
 ty; when combined with jet substructure observables, the
 performance of various groomers and taggers becomes very
 comparable, suggesting that, taken together, the observables
 studied are sensitive to nearly all of the physical differences
 between top and QCD jets. A small improvement is also
 found by combining the Johns Hopkins and HEPTopTag-
 gers, indicating that different taggers are not fully correlated.

Comparing results at different p_T and R , top tagging per-
 formance is generally better at smaller R due to less contam-
 ination from uncorrelated radiation. Similarly, most observ-
 ables perform better at larger p_T due to the higher degree
 of collimation of radiation. Some observables fare worse at
 higher p_T , such as the N -subjettiness ratio τ_{32} and the Qjet

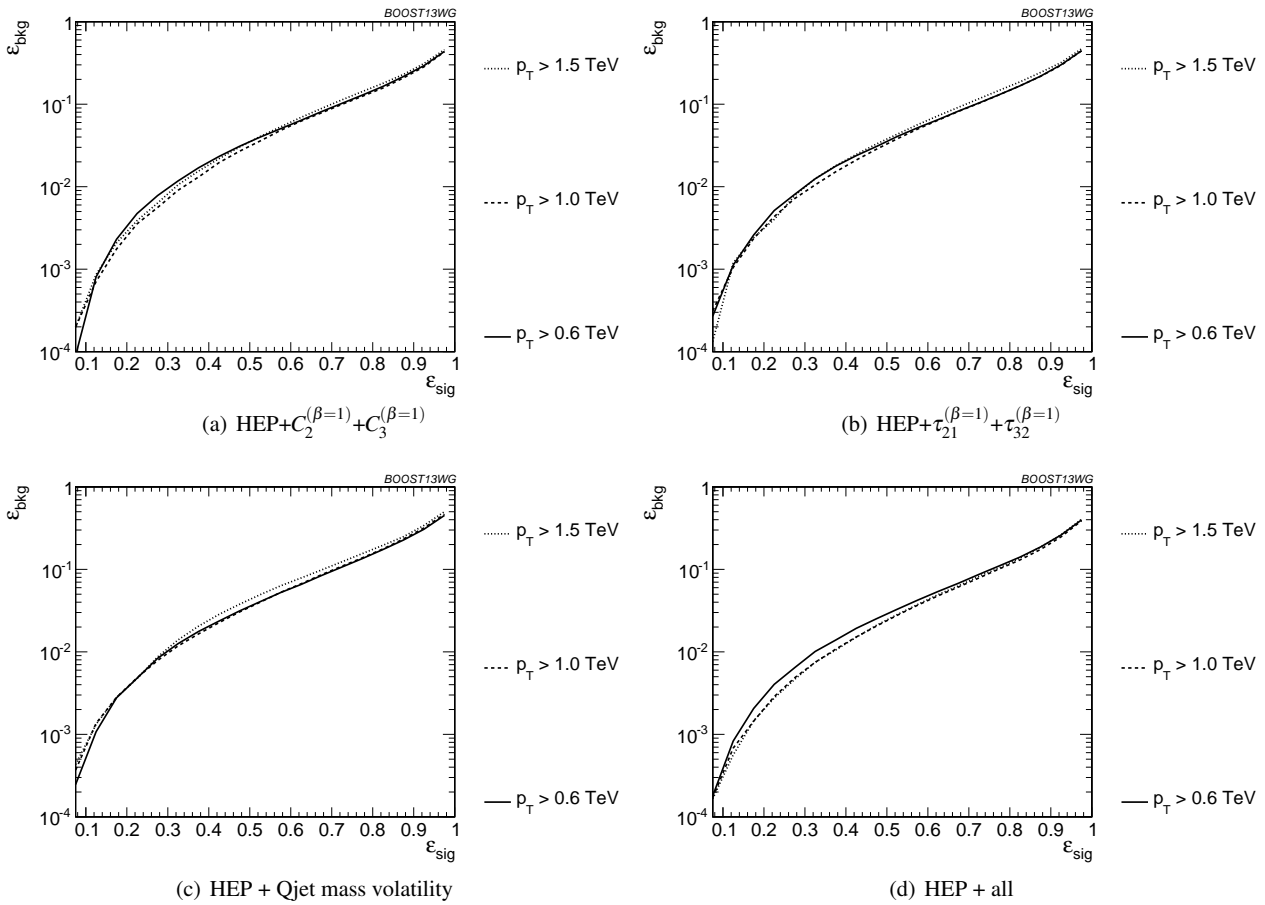


Fig. 43 Comparison of BDT combination of HEP tagger + shape at different p_T using the anti- k_T $R=0.8$ algorithm.

1550 mass volatility Γ , as higher- p_T QCD jets have more, harder
 1551 emissions that fake the top jet substructure. The HEPTop-
 1552 Tagger is also worse at large p_T due to the tendency of
 1553 the tagger to shape backgrounds around the top mass. The
 1554 p_T - and R -dependence of the multivariable combinations is
 1555 dominated by the p_T - and R -dependence of the top mass re-
 1556 construction component of the tagger/groomer.

1557 Finally, we consider the performance of various observ-
 1558 able combinations under the more realistic assumption that
 1559 the input parameters are only optimized at a single p_T , R , or
 1560 signal efficiency, and then the same inputs are used at other
 1561 working points. Remarkably, the performance of all observ-
 1562 ables is typically within a factor of 2 of the fully optimized
 1563 inputs, suggesting that while optimization can lead to sub-
 1564 stantial gains in performance, the general behaviour found
 1565 in the fully optimized analyses extends to more general ap-
 1566 plications of each variable. In particular, the performance of
 1567 pruning typically varies the least when comparing subopti-
 1568 mal working points to the fully optimized tagger due to the
 1569 scale-invariant nature of the pruning algorithm.

8 Summary & Conclusions

Furthering our understanding of jet substructure is crucial
 to improving our understanding of QCD and enhancing the
 prospects for the discovery of new physical processes at Run
 II of the LHC. In this report we have studied the perform-
 ance of jet substructure techniques over a wide range of
 kinematic regimes that will be encountered in Run II of the
 LHC. The performance of observables and their correlations
 have been studied by combining the variables into BDT dis-
 criminants, and comparing the background rejection power
 of this discriminant to the rejection power achieved by the
 individual variables. The performance of “all variables” BDT
 discriminants has also been investigated, to understand the
 potential of the “ultimate” tagger where “all” available in-
 formation (at least, all of that provided by the variables con-
 sidered) is used.

We focused on the discrimination of quark jets from gluon
 jets, and the discrimination of boosted W bosons and top
 quarks from the QCD backgrounds. For each, we have iden-
 tified the best-performing jet substructure observables, both
 individually and in combination with other observables. In

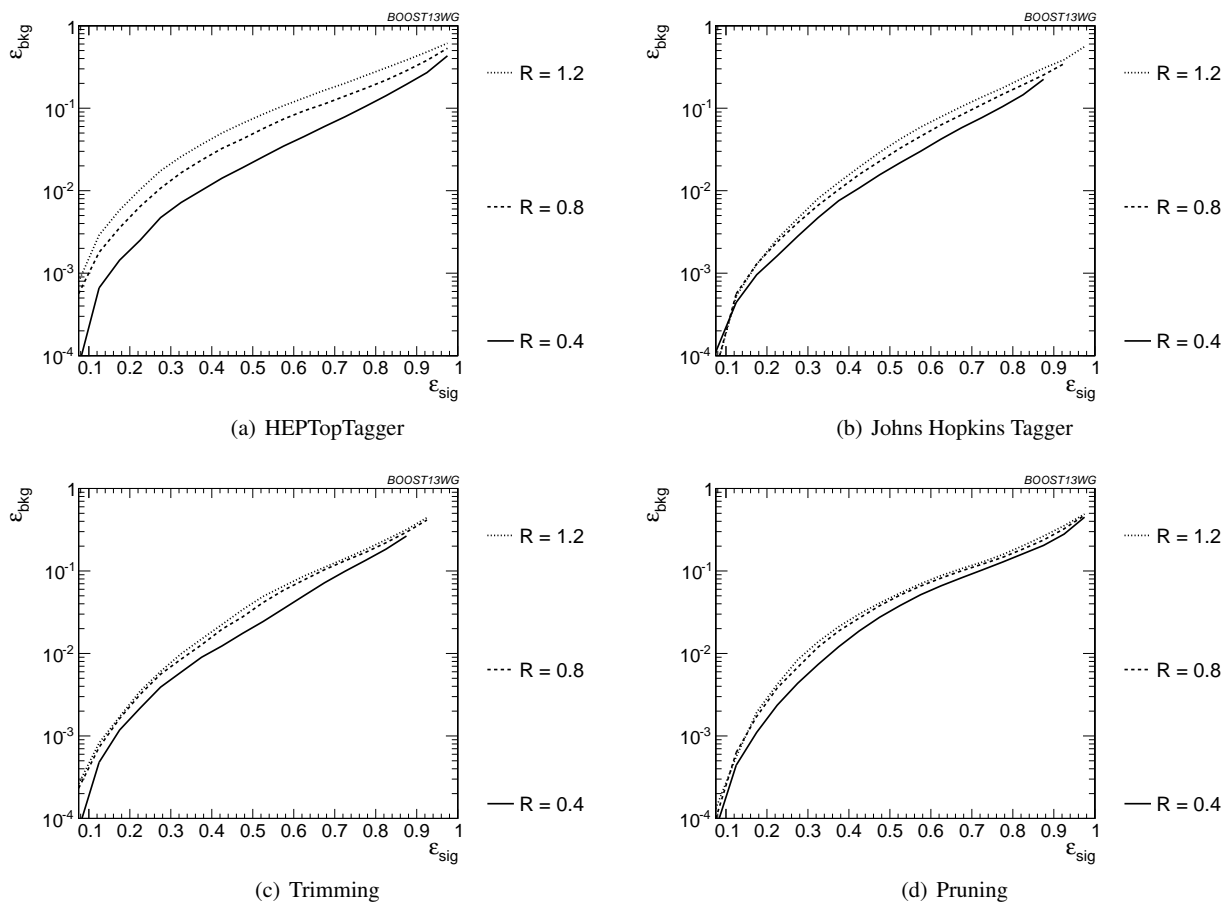


Fig. 44 Comparison of tagger and jet shape performance at different radius at $p_T = 1.5\text{-}1.6$ TeV.

1591 doing so, we have also provided a physical picture of why 1613
 1592 certain sets of observables are (un)correlated. Additionally, 1614
 1593 we have investigated how the performance of jet substructure 1615
 1594 observables varies with R and p_T , identifying observables 1616
 1595 that are particularly robust against or susceptible to 1617
 1596 these changes. In the case of q/g tagging, it seems that close 1618
 1597 to the ultimate performance can be achieved by combining 1619
 1598 the most powerful discriminant, the number of constituents 1620
 1599 of a jet, with just one other variable, $C_1^{\beta=1}$ (or $\tau_1^{\beta=1}$). Many 1621
 1600 of the other variables considered are highly correlated and 1622
 1601 provide little additional discrimination. For both top and W 1623
 1602 tagging, the groomed mass is a very important discriminating 1624
 1603 variable, but one that can be substantially improved in 1625
 1604 combination with other variables. There is clearly a rich 1626
 1605 and complex relationship between the variables considered 1627
 1606 for W and top tagging, and the performance and correlations 1628
 1607 between these variables can change considerably with 1629
 1608 changing jet p_T and R . In the case of W tagging, even after 1630
 1609 combining groomed mass with two other substructure 1631
 1610 observables, we are still some way short of the ultimate tagger 1632
 1611 performance, indicating the complexity of the information 1633
 1612 available, and the complementarity between the observables 1634

ables considered. In the case of top tagging, we have shown that the performance of both the John Hopkins and Hep Top Tagger can be improved when their outputs are combined with substructure observables such as τ_{32} and C_3 , and that the performance of a discriminant built from groomed mass information plus substructure observables is very comparable to the performance of the taggers. We have optimized the top taggers for a particular value of p_T , R , and signal efficiency, and studied their performance at other working points. We have found that the performance of observables remains within a factor of two of the optimized value, suggesting that the performance of jet substructure observables is not significantly degraded when tagger parameters are only optimized for a few select benchmark points.

Our analyses were performed with ideal detector and pile-up conditions in order to most clearly elucidate the underlying physical scaling with p_T and R . At higher boosts, detector resolution effects will become more important, and with the higher pile-up expected at Run II of the LHC, pile-up mitigation will be crucial for future jet substructure studies. Future studies will be needed to determine which of the observables we have studied are most robust against pile-up

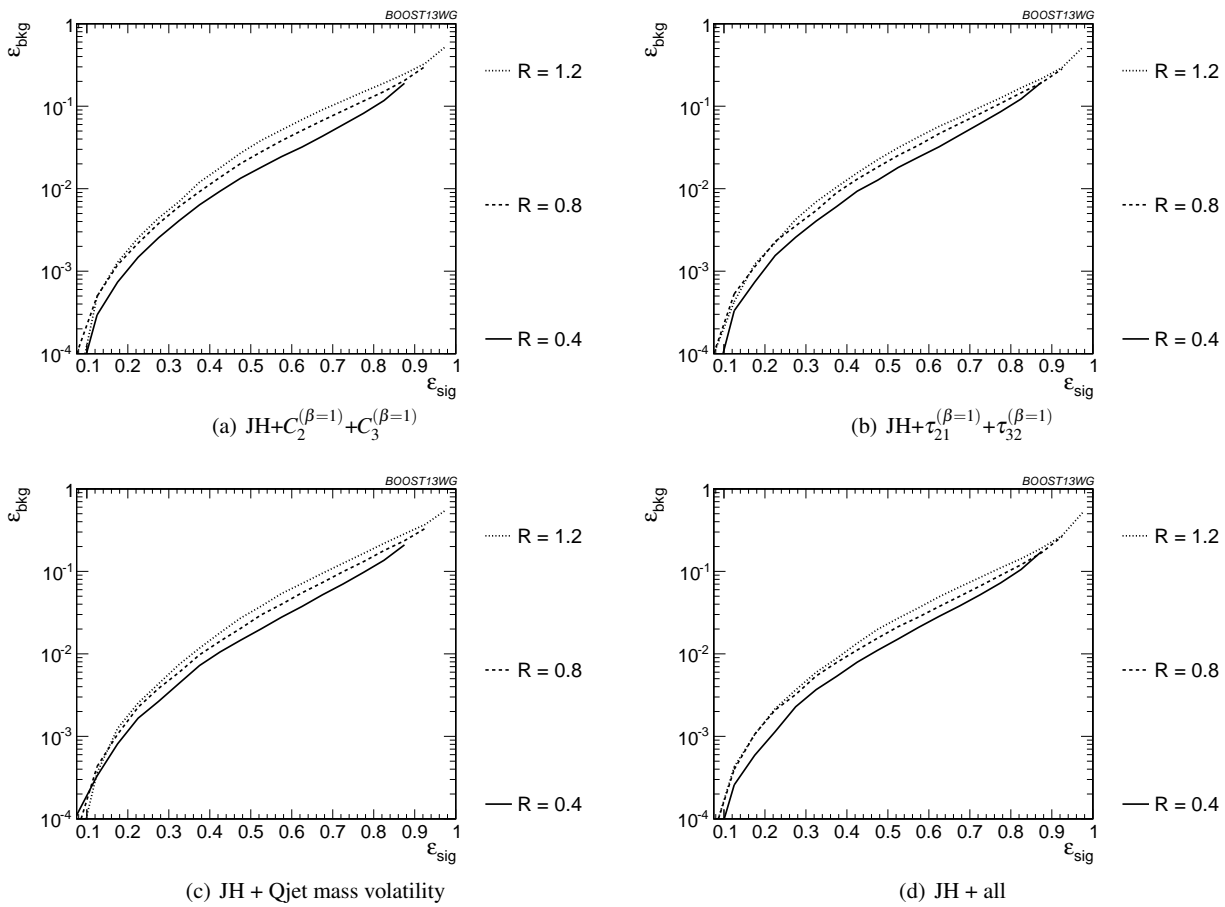


Fig. 45 Comparison of BDT combination of JH tagger + shape at different radius at $p_T = 1.5-1.6$ TeV.

1635 and detector effects, and our analyses suggest particularly useful combinations of observables to consider in such studies.

1638 At the new energy frontier of Run II of the LHC boosted jet substructure techniques will be more central to our search for new physics than ever before, and by achieving a deeper understanding of the underlying structure of quark, gluon, W and Top initiated jets, and how the observables that try to elucidate this structure are related, the hope is that more sophisticated taggers can be commissioned that will extend the reach for new physics as far as possible.

1646 References

- 1647 1. *Boost2009*, SLAC National Accelerator Laboratory, 9-10 July, 2009, [\[http://www-conf.slac.stanford.edu/Boost2009/\]](http://www-conf.slac.stanford.edu/Boost2009/).
- 1648 2. *Boost2010*, University of Oxford, 22-25 June 2010, [\[http://www.physics.ox.ac.uk/boost2010/\]](http://www.physics.ox.ac.uk/boost2010/).
- 1649 3. *Boost2011*, Princeton University, 22-26 May 2011, [\[https://indico.cern.ch/event/138809/\]](https://indico.cern.ch/event/138809/).

4. *Boost2012*, IFIC Valencia, 23-27 July 2012, [\[http://ific.uv.es/boost2012/\]](http://ific.uv.es/boost2012/).
5. *Boost2013*, University of Arizona, 12-16 August 2013, [\[https://indico.cern.ch/event/215704/\]](https://indico.cern.ch/event/215704/).
6. *Boost2014*, University College London, 18-22 August 2014, [\[http://http://www.hep.ucl.ac.uk/boost2014/\]](http://http://www.hep.ucl.ac.uk/boost2014/).
7. A. Abdesselam, E. B. Kuutmann, U. Bitenc, G. Brooijmans, J. Butterworth, et al., *Boosted objects: A Probe of beyond the Standard Model physics*, *Eur.Phys.J.* **C71** (2011) 1661, [[arXiv:1012.5412](https://arxiv.org/abs/1012.5412)].
8. A. Altheimer, S. Arora, L. Asquith, G. Brooijmans, J. Butterworth, et al., *Jet Substructure at the Tevatron and LHC: New results, new tools, new benchmarks*, *J.Phys.* **G39** (2012) 063001, [[arXiv:1201.0008](https://arxiv.org/abs/1201.0008)].
9. A. Altheimer, A. Arce, L. Asquith, J. Backus Mayes, E. Bergeaas Kuutmann, et al., *Boosted objects and jet substructure at the LHC*, [arXiv:1311.2708](https://arxiv.org/abs/1311.2708).
10. M. Cacciari, G. P. Salam, and G. Soyez, *FastJet User Manual*, *Eur.Phys.J.* **C72** (2012) 1896, [[arXiv:1111.6097](https://arxiv.org/abs/1111.6097)].

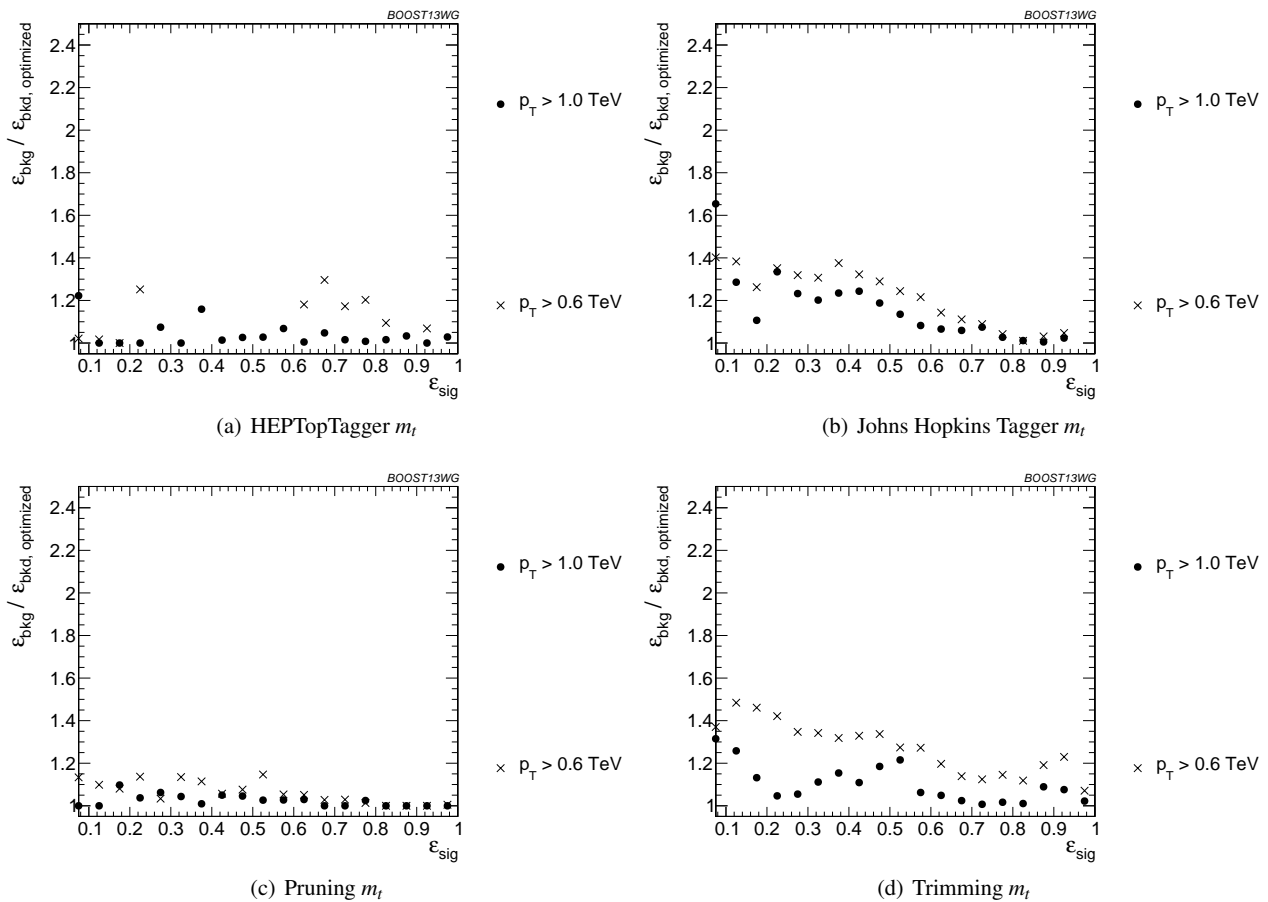


Fig. 46 Comparison of top mass performance of different taggers at different p_T using the anti- k_T $R=0.8$ algorithm; the tagger inputs are set to the optimum value for $p_T = 1.5 - 1.6$ TeV.

- 1675 11. T. Plehn, M. Spannowsky, M. Takeuchi, and 1697 **D89** (2014) 035007, [[arXiv:1309.4819](#)].
- 1676 D. Zerwas, *Stop Reconstruction with Tagged Tops*, 1698 17. J. Pumplin, D. Stump, J. Huston, H. Lai, P. M.
- 1677 *JHEP* **1010** (2010) 078, [[arXiv:1006.2833](#)]. 1699 Nadolsky, et al., *New generation of parton*
- 1678 12. D. E. Kaplan, K. Rehermann, M. D. Schwartz, and 1700 *distributions with uncertainties from global QCD*
- 1679 B. Tweedie, *Top Tagging: A Method for Identifying* 1701 *analysis*, *JHEP* **0207** (2002) 012, [[hep-ph/0201195](#)].
- 1680 *Boosted Hadronically Decaying Top Quarks*, 1702 18. T. Sjostrand, S. Mrenna, and P. Z. Skands, *A Brief*
- 1681 *Phys.Rev.Lett.* **101** (2008) 142001, 1703 *Introduction to PYTHIA 8.1*, *Comput.Phys.Commun.*
- 1682 [[arXiv:0806.0848](#)]. 1704 **178** (2008) 852–867, [[arXiv:0710.3820](#)].
- 1683 13. J. Alwall, M. Herquet, F. Maltoni, O. Mattelaer, and 1705 19. A. Buckley, J. Butterworth, S. Gieseke, D. Grellscheid,
- 1684 T. Stelzer, *MadGraph 5 : Going Beyond*, *JHEP* **1106** 1706 S. Hoche, et al., *General-purpose event generators for*
- 1685 (2011) 128, [[arXiv:1106.0522](#)]. 1707 *LHC physics*, *Phys.Rept.* **504** (2011) 145–233,
- 1686 14. Y. Gao, A. V. Gritsan, Z. Guo, K. Melnikov, 1708 [[arXiv:1101.2599](#)].
- 1687 M. Schulze, et al., *Spin determination of* 1709 20. T. Gleisberg, S. Hoeche, F. Krauss, M. Schonherr,
- 1688 *single-produced resonances at hadron colliders*, 1710 S. Schumann, et al., *Event generation with SHERPA*
- 1689 *Phys.Rev.* **D81** (2010) 075022, [[arXiv:1001.3396](#)]. 1711 *1.1*, *JHEP* **0902** (2009) 007, [[arXiv:0811.4622](#)].
- 1690 15. S. Bolognesi, Y. Gao, A. V. Gritsan, K. Melnikov, 1712 21. S. Schumann and F. Krauss, *A Parton shower*
- 1691 M. Schulze, et al., *On the spin and parity of a* 1713 *algorithm based on Catani-Seymour dipole*
- 1692 *single-produced resonance at the LHC*, *Phys.Rev.* **D86** 1714 *factorisation*, *JHEP* **0803** (2008) 038,
- 1693 (2012) 095031, [[arXiv:1208.4018](#)]. 1715 [[arXiv:0709.1027](#)].
- 1694 16. I. Anderson, S. Bolognesi, F. Caola, Y. Gao, A. V. 1716 22. F. Krauss, R. Kuhn, and G. Soff, *AMEGIC++ 1.0: A*
- 1695 Gritsan, et al., *Constraining anomalous HVV* 1717 *Matrix element generator in C++*, *JHEP* **0202** (2002)
- 1696 *interactions at proton and lepton colliders*, *Phys.Rev.* 1718 044, [[hep-ph/0109036](#)].

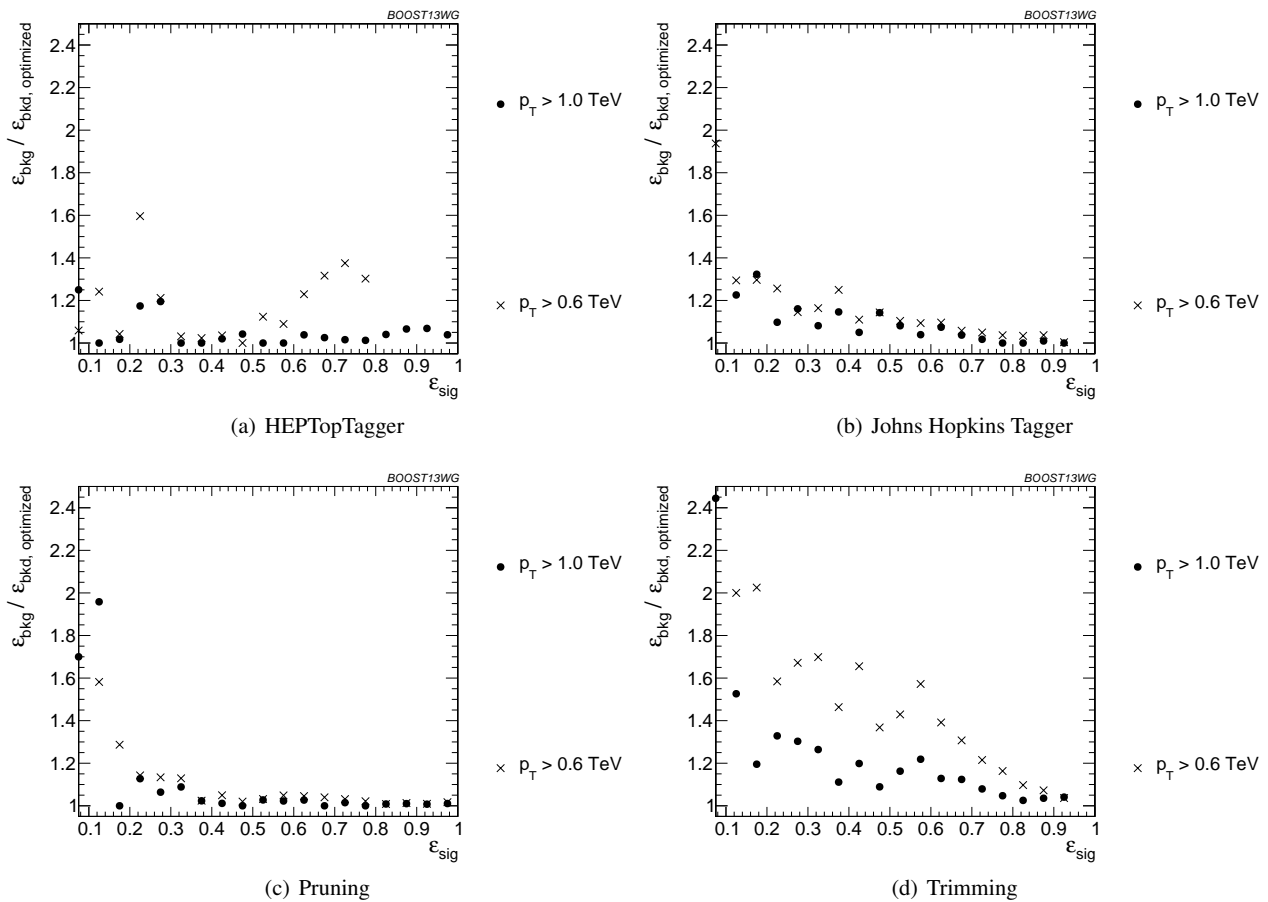


Fig. 47 Comparison of BDT combination of tagger performance at different p_T using the anti- k_T $R=0.8$ algorithm; the tagger inputs are set to the optimum value for $p_T = 1.5 - 1.6$ TeV.

- 1719 23. T. Gleisberg and S. Hoeche, *Comix, a new matrix* 1741
 1720 *element generator*, *JHEP* **0812** (2008) 039, 1742
 1721 [[arXiv:0808.3674](#)]. 1743
- 1722 24. S. Hoeche, F. Krauss, S. Schumann, and F. Siegert, 1744
 1723 *QCD matrix elements and truncated showers*, *JHEP* 1745
 1724 **0905** (2009) 053, [[arXiv:0903.1219](#)]. 1746
- 1725 25. M. Schonherr and F. Krauss, *Soft Photon Radiation in* 1747
 1726 *Particle Decays in SHERPA*, *JHEP* **0812** (2008) 018, 1748
 1727 [[arXiv:0810.5071](#)]. 1749
- 1728 26. **JADE Collaboration** Collaboration, S. Bethke et al., 1750
 1729 *Experimental Investigation of the Energy Dependence* 1751
 1730 *of the Strong Coupling Strength*, *Phys.Lett.* **B213** 1752
 1731 (1988) 235. 1753
- 1732 27. M. Cacciari, G. P. Salam, and G. Soyez, *The Anti- $k(t)$* 1754
 1733 *jet clustering algorithm*, *JHEP* **0804** (2008) 063, 1755
 1734 [[arXiv:0802.1189](#)]. 1756
- 1735 28. Y. L. Dokshitzer, G. Leder, S. Moretti, and B. Webber, 1757
 1736 *Better jet clustering algorithms*, *JHEP* **9708** (1997) 1758
 1737 001, [[hep-ph/9707323](#)]. 1759
- 1738 29. M. Wobisch and T. Wengler, *Hadronization* 1760
 1739 *corrections to jet cross-sections in deep inelastic* 1761
 1740 *scattering*, [hep-ph/9907280](#). 1762
30. S. Catani, Y. L. Dokshitzer, M. Seymour, and 1741
 B. Webber, *Longitudinally invariant K_t clustering*
algorithms for hadron hadron collisions, *Nucl.Phys.*
B406 (1993) 187–224. 1742
31. S. D. Ellis and D. E. Soper, *Successive combination jet*
algorithm for hadron collisions, *Phys.Rev.* **D48** (1993)
 3160–3166, [[hep-ph/9305266](#)]. 1743
32. S. D. Ellis, A. Hornig, T. S. Roy, D. Krohn, and M. D.
 Schwartz, *Qjets: A Non-Deterministic Approach to*
Tree-Based Jet Substructure, *Phys.Rev.Lett.* **108** (2012)
 182003, [[arXiv:1201.1914](#)]. 1744
33. S. D. Ellis, A. Hornig, D. Krohn, and T. S. Roy, *On*
Statistical Aspects of Qjets, *JHEP* **1501** (2015) 022,
 [[arXiv:1409.6785](#)]. 1745
34. S. D. Ellis, C. K. Vermilion, and J. R. Walsh,
Recombination Algorithms and Jet Substructure:
Pruning as a Tool for Heavy Particle Searches,
Phys.Rev. **D81** (2010) 094023, [[arXiv:0912.0033](#)]. 1746
35. D. Krohn, J. Thaler, and L.-T. Wang, *Jet Trimming*,
JHEP **1002** (2010) 084, [[arXiv:0912.1342](#)]. 1747
36. J. M. Butterworth, A. R. Davison, M. Rubin, and G. P.
 Salam, *Jet substructure as a new Higgs search channel* 1748

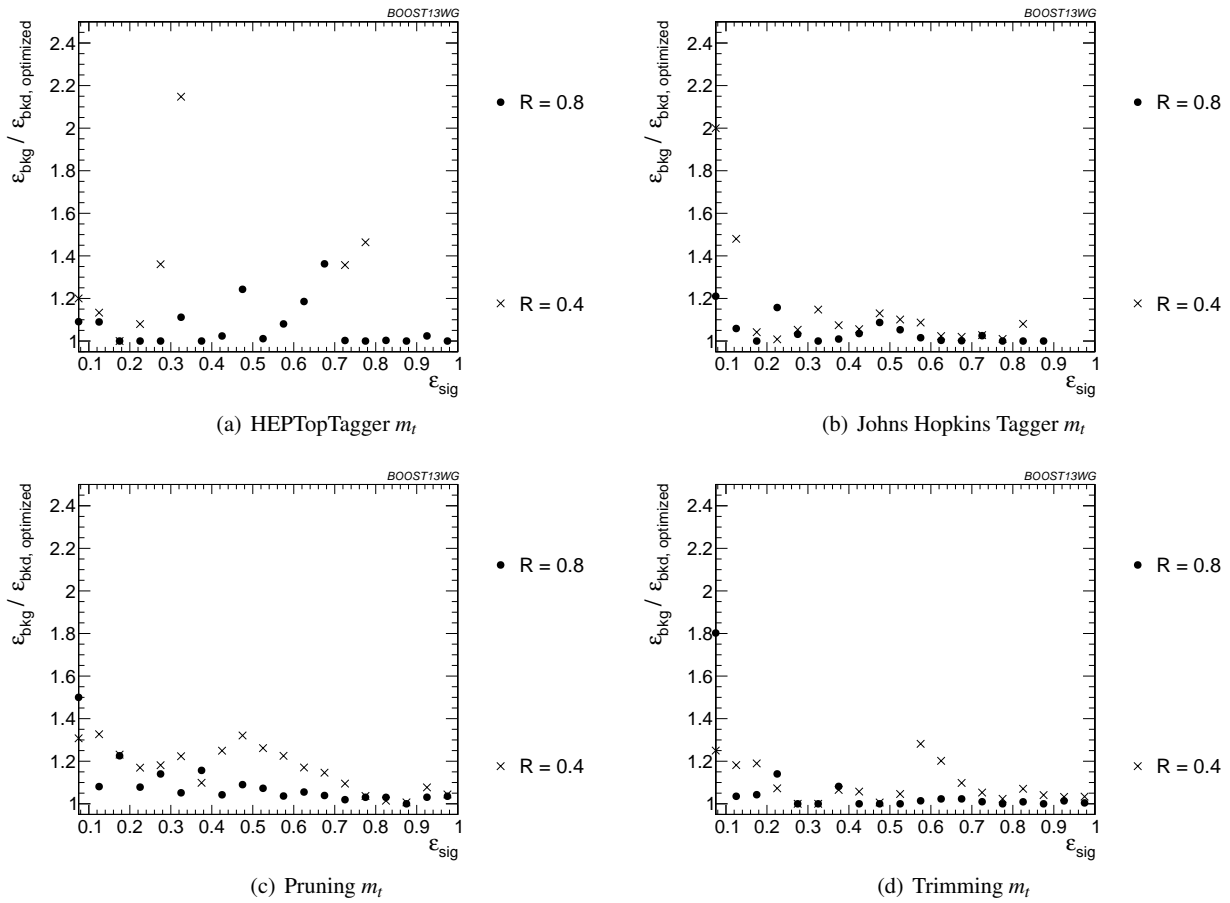


Fig. 48 Comparison of top mass performance of different taggers at different R in the $p_T = 1500 - 1600$ GeV bin; the tagger inputs are set to the optimum value for $R = 1.2$.

- 1763 at the LHC, *Phys.Rev.Lett.* **100** (2008) 242001, 1785
 1764 [[arXiv:0802.2470](#)]. 1786
- 1765 37. A. J. Larkoski, S. Marzani, G. Soyez, and J. Thaler, 1787
 1766 *Soft Drop*, *JHEP* **1405** (2014) 146, 1788
 1767 [[arXiv:1402.2657](#)]. 1789
- 1768 38. M. Dasgupta, A. Fregoso, S. Marzani, and G. P. Salam, 1790
 1769 *Towards an understanding of jet substructure*, *JHEP* 1791
 1770 **1309** (2013) 029, [[arXiv:1307.0007](#)]. 1792
- 1771 39. J. Thaler and K. Van Tilburg, *Identifying Boosted* 1793
 1772 *Objects with N -subjettiness*, *JHEP* **1103** (2011) 015, 1794
 1773 [[arXiv:1011.2268](#)]. 1795
- 1774 40. A. J. Larkoski, D. Neill, and J. Thaler, *Jet Shapes with* 1796
 1775 *the Broadening Axis*, *JHEP* **1404** (2014) 017, 1797
 1776 [[arXiv:1401.2158](#)]. 1798
- 1777 41. A. J. Larkoski and J. Thaler, *Unsafe but Calculable:* 1799
 1778 *Ratios of Angularities in Perturbative QCD*, *JHEP* 1800
 1779 **1309** (2013) 137, [[arXiv:1307.1699](#)]. 1801
- 1780 42. A. J. Larkoski, G. P. Salam, and J. Thaler, *Energy* 1802
 1781 *Correlation Functions for Jet Substructure*, *JHEP* **1306** 1803
 1782 (2013) 108, [[arXiv:1305.0007](#)]. 1804
- 1783 43. **CMS Collaboration** Collaboration, S. Chatrchyan 1805
 1784 et al., *Search for a Higgs boson in the decay channel H*
to ZZ^ to $q \bar{q} \ell^- \ell^+$ in pp collisions at $\sqrt{s} = 7$*
TeV, *JHEP* **1204** (2012) 036, [[arXiv:1202.1416](#)].
44. A. J. Larkoski, J. Thaler, and W. J. Waalewijn, *Gaining*
(Mutual) Information about Quark/Gluon
Discrimination, *JHEP* **1411** (2014) 129,
 [[arXiv:1408.3122](#)].
45. A. Hoecker, P. Speckmayer, J. Stelzer, J. Therhaag,
 E. von Toerne, and H. Voss, *TMVA: Toolkit for*
Multivariate Data Analysis, *PoS ACAT* (2007) 040,
 [[physics/0703039](#)].
46. **ATLAS Collaboration** Collaboration, G. Aad et al.,
Light-quark and gluon jet discrimination in pp
collisions at $\sqrt{s} = 7$ TeV with the ATLAS detector,
Eur.Phys.J. **C74** (2014), no. 8 3023,
 [[arXiv:1405.6583](#)].
47. J. Gallicchio and M. D. Schwartz, *Quark and Gluon*
Jet Substructure, *JHEP* **1304** (2013) 090,
 [[arXiv:1211.7038](#)].
48. J. Gallicchio and M. D. Schwartz, *Quark and Gluon*
Tagging at the LHC, *Phys.Rev.Lett.* **107** (2011)
 172001, [[arXiv:1106.3076](#)].

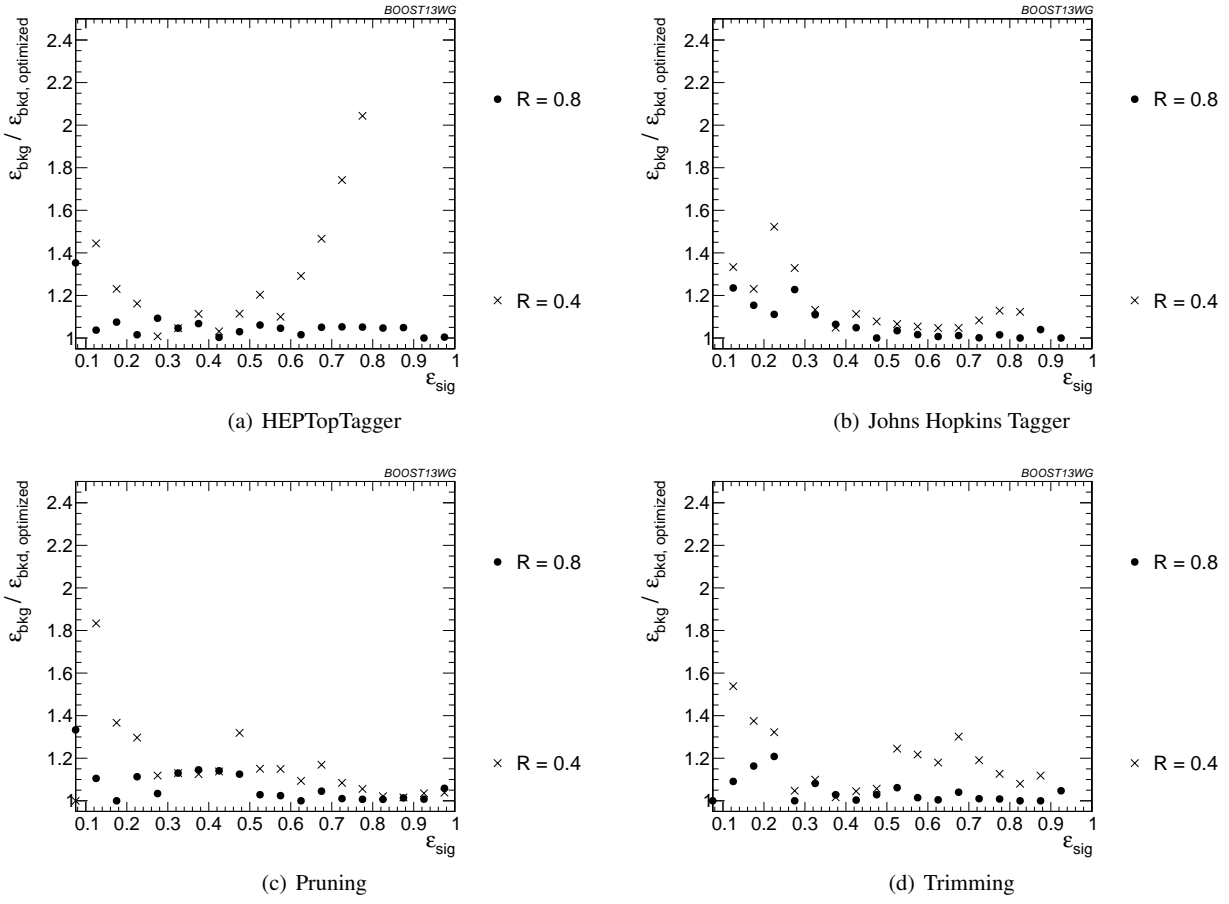


Fig. 49 Comparison of BDT combination of tagger performance at different radius at $p_T = 1.5-1.6$ TeV; the tagger inputs are set to the optimum value for $R = 1.2$.

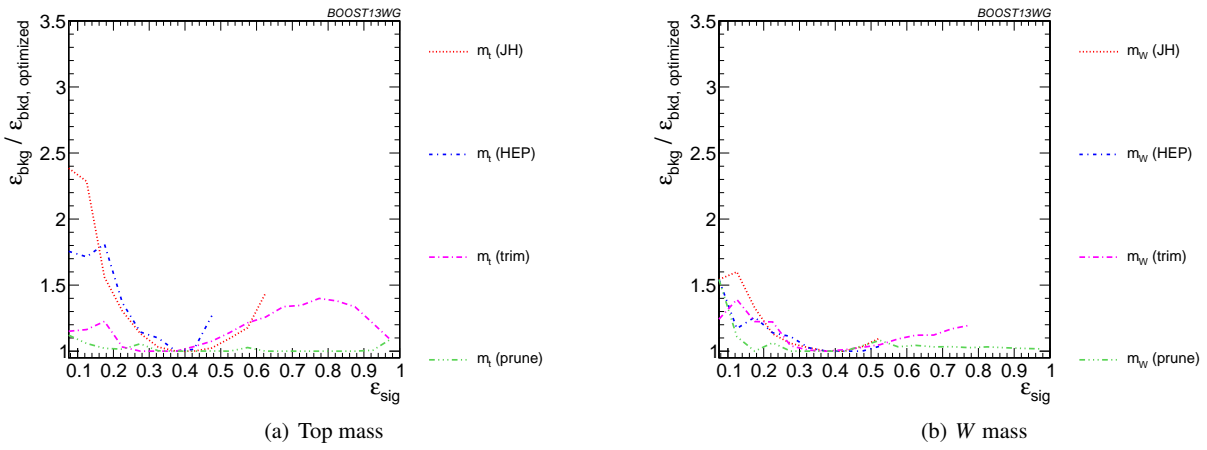


Fig. 50 Comparison of single-variable top-tagging performance in the $p_T = 1 - 1.1$ GeV bin using the anti- k_T , $R=0.8$ algorithm; the inputs for each tagger are optimized for the $\epsilon_{\text{sig}} = 0.3 - 0.35$ bin.

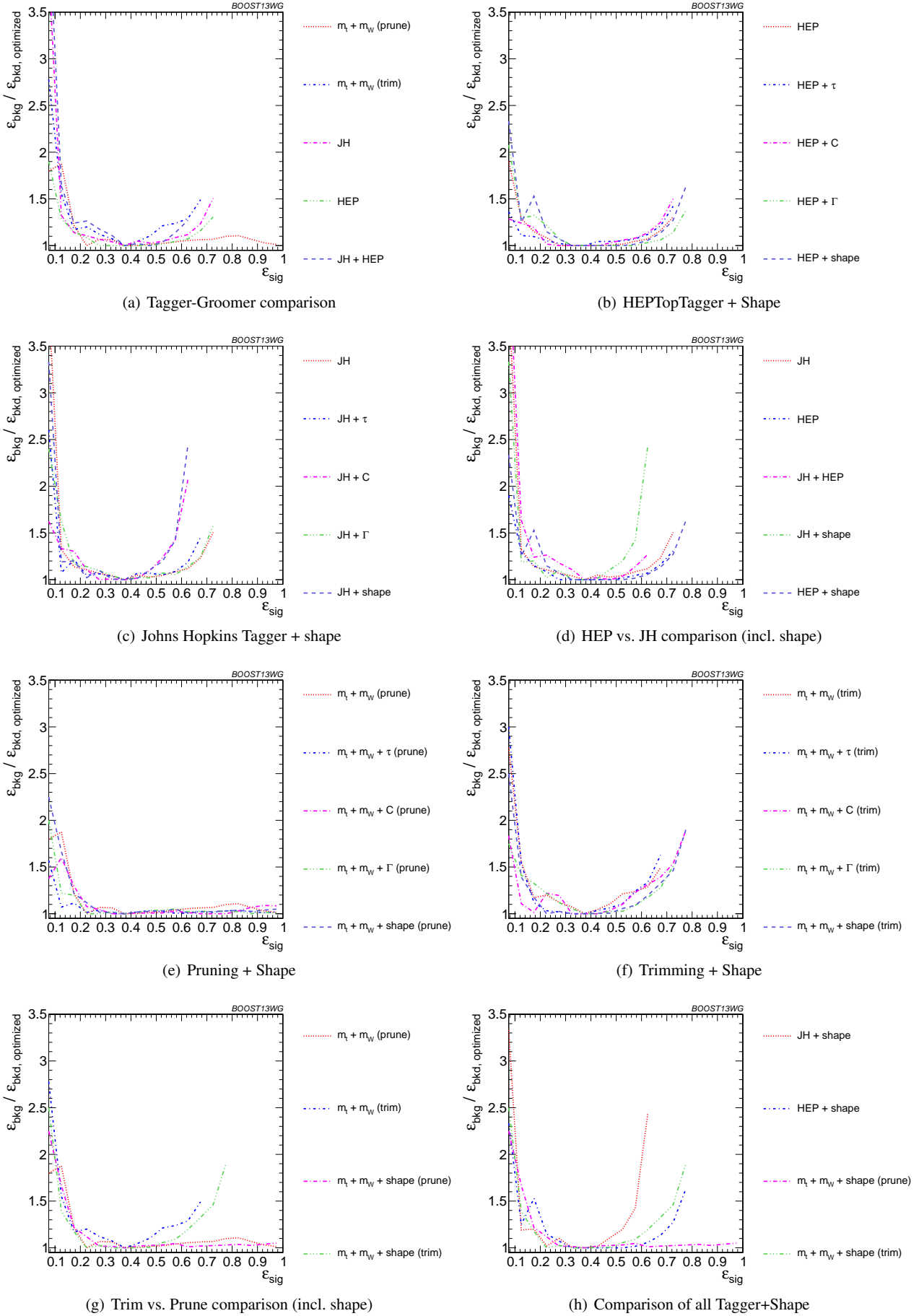


Fig. 51 The BDT combinations in the $p_T = 1 - 1.1$ TeV bin using the anti- k_T $R=0.8$ algorithm. Taggers are combined with the following shape observables: $\tau_{21}^{(\beta=1)} + \tau_{32}^{(\beta=1)}$, $C_2^{(\beta=1)} + C_3^{(\beta=1)}$, Γ_{Qjet} , and all of the above (denoted “shape”). The inputs for each tagger are optimized for the $\epsilon_{\text{sig}} = 0.3 - 0.35$ bin.

-
- 1806 49. **CMS Collaboration** Collaboration, C. Collaboration,
1807 *Performance of quark/gluon discrimination in 8 TeV pp*
1808 *data*, .
- 1809 50. H.-n. Li, Z. Li, and C.-P. Yuan, *QCD resummation for*
1810 *light-particle jets*, *Phys.Rev.* **D87** (2013) 074025,
1811 [[arXiv:1206.1344](#)].
- 1812 51. M. Dasgupta, K. Khelifa-Kerfa, S. Marzani, and
1813 M. Spannowsky, *On jet mass distributions in Z+jet and*
1814 *dijet processes at the LHC*, *JHEP* **1210** (2012) 126,
1815 [[arXiv:1207.1640](#)].
- 1816 52. Y.-T. Chien, R. Kelley, M. D. Schwartz, and H. X. Zhu,
1817 *Resummation of Jet Mass at Hadron Colliders*,
1818 *Phys.Rev.* **D87** (2013), no. 1 014010,
1819 [[arXiv:1208.0010](#)].
- 1820 53. T. T. Jouttenus, I. W. Stewart, F. J. Tackmann, and W. J.
1821 Waalewijn, *Jet mass spectra in Higgs boson plus one*
1822 *jet at next-to-next-to-leading logarithmic order*,
1823 *Phys.Rev.* **D88** (2013), no. 5 054031,
1824 [[arXiv:1302.0846](#)].
- 1825 54. S. D. Ellis, C. K. Vermilion, and J. R. Walsh,
1826 *Techniques for improved heavy particle searches with*
1827 *jet substructure*, *Phys.Rev.* **D80** (2009) 051501,
1828 [[arXiv:0903.5081](#)].
- 1829 55. M. Dasgupta, A. Fregoso, S. Marzani, and A. Powling,
1830 *Jet substructure with analytical methods*, *Eur.Phys.J.*
1831 **C73** (2013), no. 11 2623, [[arXiv:1307.0013](#)].
- 1832 56. *Performance of Boosted W Boson Identification with*
1833 *the ATLAS Detector*, Tech. Rep.
1834 ATLAS-PHYS-PUB-2014-004, CERN, Geneva, Mar,
1835 2014.
- 1836 57. S. Schaetzel and M. Spannowsky, *Tagging highly*
1837 *boosted top quarks*, *Phys.Rev.* **D89** (2014), no. 1
1838 014007, [[arXiv:1308.0540](#)].
- 1839 58. C. Anders, C. Bernaciak, G. Kasieczka, T. Plehn, and
1840 T. Schell, *Benchmarking an Even Better*
1841 *HEPTopTagger*, *Phys.Rev.* **D89** (2014) 074047,
1842 [[arXiv:1312.1504](#)].